UNIVERSIDADE ESTADUAL PAULISTA "JÚLIO DE MESQUITA FILHO"
Programa de Pós-Graduação em Ciência e Tecnologia de Materiais

Caio Castanho Xavier

FUNCTIONALIZATION OF THE Ti-15Zr-15Mo ALLOY BY MICRO-ARC OXIDATION

Bauru
2021

Caio Castanho Xavier

FUNCTIONALIZATION OF THE Ti-15Zr-15Mo ALLOY BY MICRO-ARC OXIDATION

Tese apresentada à Universidade Estadual Paulista – Curso de Doutorado, como um dos requisitos à obtenção do título de Doutor em Ciência e Tecnologia de Materiais, sob a orientação do Prof. Dr. Luis Augusto Sousa Marques da Rocha.

Bauru
2021

X3f

Xavier, Caio Castanho

Functionalization of the Ti-15Zr-15Mo alloy by Micro-Arc Oxidation / Caio Castanho Xavier. -- Bauru, 2021

99 p. : il., tabs.

Tese (doutorado) - Universidade Estadual Paulista (Unesp), Faculdade de Ciências, Bauru

Orientador: Luis Augusto Sousa Marques da Rocha

1. Biomateriais. 2. Ligas de titânio. 3. Corrosão. 4. Tribocorrosão. 5. Micro-arc oxidation. I. Título.

Sistema de geração automática de fichas catalográficas da Unesp. Biblioteca da Faculdade de Ciências, Bauru. Dados fornecidos pelo autor(a).

Essa ficha não pode ser modificada.

UNIVERSIDADE ESTADUAL PAULISTA

Câmpus de Bauru

ATA DA DEFESA PÚBLICA DA TESE DE DOUTORADO DE CAIO CASTANHO XAVIER, DISCENTE DO PROGRAMA DE PÓS-GRADUAÇÃO EM CIÊNCIA E TECNOLOGIA DE MATERIAIS, DA FACULDADE DE CIÊNCIAS - CÂMPUS DE BAURU.

Aos 17 dias do mês de dezembro do ano de 2020, às 10:00 horas, no(a) por videoconferência, realizou-se a defesa de TESE DE DOUTORADO de CAIO CASTANHO XAVIER, intitulada **Functionalization of the Ti-15Zr-15Mo alloy by micro-arc oxidation**. A Comissão Examinadora foi constituida pelos seguintes membros: Prof. Dr. LUÍS AUGUSTO SOUSA MARQUES DA ROCHA (Participação Virtual) do(a) Departamento de Engenharia Mecânica da Universidade do Minho - Portugal, Prof. Dr. FATIH TOPTAN (Participação Virtual) do(a) Departamento de Engenharia Mecânica / Universidade do Minho, Profa. Dra. LUCIA VIEIRA (Participação Virtual) do(a) Laboratório de Nanotecnologia e Processos a Plasma / UNIVERSIDADE DO VALE DO PARAIBA, Prof. Dr. DIEGO RAFAEL NESPEQUE CORRÊA (Participação Virtual) do(a) Instituto Federal de São Paulo - Campus de Sorocaba, Prof. Dr. CARLOS ROBERTO GRANDINI (Participação Virtual) do(a) Departamento de Física / Faculdade de Ciências - UNESP/Bauru. Após a exposição pelo doutorando e arguição pelos membros da Comissão Examinadora que participaram do ato, de forma presencial e/ou virtual, o discente recebeu o conceito final:_ _ _ A Prova 22 _ _ _ . Nada mais havendo, foi lavrada a presente ata, que após lida e aprovada, foi assinada pelo(a) Presidente(a) da Comissão Examinadora.

Prof. Dr. LUÍS AUGUSTO SOUSA MARQUES DA ROCHA Luís Augusto Rocha

“For me, I am driven by two main philosophies: know more today about the world than I knew yesterday and lessen the suffering of others. You'd be surprised how far that gets you”.

Neil deGrasse Tyson.

Acknowledgements

First, I would like to acknowledge Geisa Oliveira Daré for the love, support and advices along all these years.

To my parents, Ricardo and Edilaine, and my family, I would like to thank for believing in my potential and for all their support.

To my advisor and friend, Luis Augusto Sousa Marques da Rocha, for all his guidance and shared knowledge and experience.

To Professors Carlos Roberto Grandini, Fatih Toptan and Alexandra, for all their rich suggestions, discussions and teachings.

To all my laboratory colleagues and friends (Diego, Pedro e Marcel), for the companionship and the nostalgic moments of distraction and laughter.

To CAPES and FCT for the financial support in Portugal.

XAVIER, C. C. **Functionalization of the Ti-15Zr-15Mo alloy by micro-arc oxidation**. 2020. 99 p. Tese (Doutorado – Programa de Pós-Graduação em Ciência e Tecnologia de Materiais) UNESP, Faculdade de Ciências, Bauru (SP), 2021.

Resumo

A pesquisa e o desenvolvimento de novos biomateriais com aplicação como implantes médicos vêm crescendo consideravelmente, visto que a demanda por tais dispositivos deve aumentar nos próximos anos. O titânio e suas ligas são o foco das pesquisas para o desenvolvimento de biomateriais metálicos, devido às propriedades relativamente mais vantajosas, como: biocompatibilidade, módulo de elasticidade, massa específica, resistência mecânica e resistência à corrosão. De fato, em relação às propriedades do bulk, as ligas de titânio, principalmente aquelas com fase β, apresentam valores menores de módulo de elasticidade, o que reduz o efeito de stress shielding, conhecido por causar possíveis falhas de implantes e, consequentemente, cirurgias de revisão. Além disso, outras propriedades são necessárias para que ocorra a osseointegração de um implante, nomeadamente aquelas relacionadas com as interações que ocorrem com a sua superfície, tais como: a promoção de uma osseointegração rápida, para evitar ou minimizar as possibilidades de colonização por microrganismos que causam infecção; e ter um alta resistência à corrosão e desgaste mecânico. Este trabalho teve como objetivo a utilização de uma liga de titânio do tipo β (Ti-15Zr-15Mo), para desenvolver novos métodos de funcionalização, a fim de atender aos requisitos mencionados acima e desenvolver um novo biomaterial, visando uma aplicação biomédica. Desse modo, a técnica de Micro-arc Oxidation (MAO) foi utilizada para a criação de filmes de óxido de titânio com alta resistência à corrosão e ao desgaste mecânico, e dentro desses filmes, a incorporação de elementos bioativos (Ca, P e Zn), que são conhecidos por contribuir para maior bioatividade e melhor comportamento quanto a corrosão e tribocorrosão.

XAVIER, C. C. **Functionalization of the Ti-15Zr-15Mo alloy by micro-arc oxidation**. 2020. 99 p. Tese (Doutorado – Programa de Pós-Graduação em Ciência e Tecnologia de Materiais) UNESP, Faculdade de Ciências, Bauru (SP), 2021.

Abstract

The research and development of new biomaterials with applicability in medical implants has been growing considerably since the demand for such devices is expected to increase in the coming years. Titanium and its alloys are the focus of the research for the development of metallic biomaterials, due to the relatively more advantageous properties, such as: biocompatibility, elastic modulus, specific mass, mechanical resistance, and corrosion resistance. In fact, regarding their bulk properties, titanium alloys, especially those with β phase, have lower values of elastic modulus, which reduces the effect of stress shielding, known to cause possible implant failure and revision surgeries. Also, other properties are required for an osseointegrated implant, namely those related to the interactions that occur with its surface, such as the promotion of rapid osseointegration, to avoid or minimize the possibilities of colonization by microorganisms that cause infection and having a high resistance to corrosion and mechanical wear. This work aimed to use a β-type titanium alloy (Ti-15Zr-15Mo), to develop new methods of functionalization in order to meet the requirements mentioned above for a new biomaterial for a biomedical application. Thus, the Micro-arc Oxidation (MAO) technique was used in order to create titanium oxide films with high resistance to corrosion and mechanical wear, and within these films, the incorporation of bioactive elements (Ca, P and Zn), which are known to contribute to increased bioactivity and better electrochemical and tribocorrosion behavior.

Table of Contents

List of Figures

List of Tables

1. INTRODUCTION

1.1. Titanium and Titanium alloys for biomaterial applications

A biomaterial is said to be a natural or synthetic material used for medical applications which can interact with biological systems in order to repair and/or replace tissues, organs or biological functions, aiming to maintain or improve the patient's quality of life [1-3]. However, in order to be used as a biomaterial, some important properties need to be reached, as in the need to resemble the physical and biological conditions of the tissue or organ where the material would be implanted. Also, a biomaterial must promote positively interactions with the host's organism in their required application. In fact, a material is considered as biocompatible whether its faculty to perform a desired function as medical therapy without causing undesirable effects locally or systemically, and yet, bring forth beneficial biological responses to the surround tissue, as well as optimizing clinical performance to applied therapy [3, 4].

The research and development of new biomaterials is a worldwide trend, because of the ongoing increase in the life expectancy and populational growth in the last decades. Combining these facts with the rise in traffic and sports injuries in the last years, the need to develop more effectiveness in treatments and quality of life for patients is utterly required [2-7]. Furthermore, the studied implants must ensure a mechanical resistance suitable to its applied location in the human body. Thus, a biomaterial aiming for an orthopedic or dental application must endure high loads without fracturing or fatigue, and also be resistant to corrosion and tribocorrosion because of the wear in a biological environment due to the constant friction of micro-movements [8-11]. Recent researches revealed the economic burden regarding revision surgeries for total knee arthroplasty (TKA), total joint arthroplasty (TJA) or total hip arthroplasty (THA) in the years to come, due to the relatively low lifespan of the current implants and their respectively failures from biomechanical mismatch and/or infections [12-15]. Old et al. (2017), found that regarding total knee arthroplasty, about 27% of the patients required revision surgeries, where the time between the primary surgery and the revision were approximately 12,5 years. The main cause for the revision surgery related to the wear and loosening of the implant (about 68%) and the other major cause was mostly due to infections (20%). Kurtz et al. (2007), estimate that by 2030, the projections are that the demand for primary surgeries of total hip arthroplasty will increase 174% (572 thousand procedures) and

for total knee arthroplasty 673% (3.48 million procedures). In addition, revision surgeries for hip and knee are estimated to increase in 137% and 601%, respectively [12-15]. Also, because of the increase in these type of surgeries for younger patients with a longer life expectancy, the lifespan of such devices must increase proportionally [16]. Therefore, because of these estimates and the current lifespan of the commercial implants, it is undeniable that the research and development of new and improved biomaterials is of great relevance.

The metallic biomaterials exhibit a more suitable combination of the required properties as a medical implant than polymeric or ceramic materials for orthopedic and dentistry applications. In fact, metallic biomaterials composed about 70% of all medical implants, such as in orthopedics (knee joints, total hip joints, bone plates, fracture fixation wires, pins, screws and plates) and cardiovascular (heart valves, artificial stents, vascular stents and peacemaker parts) [17-20]. The most common metallic biomaterials are the stainless steel, cobalt-chromium alloys, and titanium alloys. The SS316L alloy is generally used as temporarily implants (screws and bone plates). However, due to the presence and high toxicity of nickel, research, and development of new alloys are ongoing. On the other hand, cobalt-chromium and titanium alloys are intended for permanent medical applications (e.g. hip implants), due to more suitable properties for these applications. Alloys such as Co-Cr-Mo and Co-Cr-W-Ni are widely used as joint implants, dental wires, and stents. Even though, these alloys present long-term problems due to the toxicity of some alloying elements and some mechanical problems such as stress shielding [17-21].

Titanium and titanium alloys are widely studied as a worldwide trend, whether in industry, aeronautics, aerospace, or medical application. As a biomaterial, either orthopedic or dental implants, its application is unanimous [9, 22, 23]. Over the years, researches with titanium alloys covered binary and ternary systems with the most variety of alloying elements, since titanium alloys present relatively beneficial characteristics for biomedical applications, such as: biocompatibility, corrosion resistance, low elastic modulus, mechanical strength and low specific mass [7, 23-25].

The properties of commercially pure titanium can be seen in Table 1. In general, titanium, which is relatively abundant in nature, is known for relatively low specific mass, high melting point, low elastic modulus, corrosion resistance, low thermal conductivity, low coefficient of linear expansion and is a poor electrical conductor. At room temperature it has a hexagonal close packed crystalline structure (HCP, ratio c / a = 1.587, network parameter =

3.3065Å), called alpha phase. When above 882.5 ºC temperature it undergoes an allotropic transformation, changing its structure to the body centered cubic structure (BCC), called beta phase. Due to the titanium allotropy, it is possible to control and manipulate the microstructure of the alloy and thus its mechanical properties, through the addition of alloying elements and / or heat treatments [24-26]. Thus, titanium alloys can be divided and categorized according to the phases present in their microstructure, essentially as: α phase alloys, α + β phase alloys and β phase alloys. The α phase alloys are those that have large amounts of α-phase stabilizers elements, that is, alloying elements that are capable of increasing the β-transus temperature of the alloy. With the addition of small amounts of β phase stabilizer elements, alloying elements that decrease the β-transus temperature, the alloy can be called near-α. On the other hand, α + β type alloys are those that have stabilizers in both phases. Finally, β-type alloys are those with sufficient capable alloying elements that stabilize β phase at room temperature. Alloys of this type have higher hardness values and low elastic modulus, making them more interesting for applications such as dental and orthopedic implants [10, 25, 27].

In fact, the stress shielding phenomena occurs due to a biomechanical incompatibility of the material that presents higher elastic modulus values than compared to the bone, leading to bone atrophy and consequently the implant failure. It is known that β-type titanium alloys show a reduction in the elastic modulus due to the β phase presence in the alloy. Therefore, these alloys are extensively studied, exhibiting lower values of elastic modulus than other biomedical alloys already mentioned, such as: Co-Cr-Mo alloys (210 GPa), stainless steel alloys (200 GPa), or Ti-6Al -4V (110 GPa) [9, 27].

In previous works of our group, zirconium and molybdenum were used as alloying elements, resulting in an increase of β phase due to the addition of molybdenum in the alloy, together with an increase in its microhardness. The Ti-15Zr-15Mo alloy presented a microstructure composed only by β phase and with an elastic modulus of 75 GPa [26, 28, 29].

In addition, as there is a direct contact between the material's surface and body fluids, the molecular interactions between both must be considered. Thereby preserving the material and its properties and aiming at the adhesion of the appropriate proteins on its surface, since they mediate the osteoblast adhesion process. Because its surface is very reactive with oxygen at high temperatures, titanium can naturally form a thin layer of titanium oxide (TiO_2). Due to this specific property, titanium together with surface treatment techniques is of great importance for the research and development of orthopedic and dental biomaterials [11, 18, 30-34].

Table 1 - Properties of the titanium element [10, 25, 27].

Properties of commercially pure titanium (cp-Ti)	Values
Atomic Number	22
Atomic Weight (g/mol)	47.90
Hexagonal close packed crystalline structure (HCP)	α phase, c= 4.6832±0.0004Å and a=2.9504±0.0004 Å
Body centered cubic structure (BCC)	ß phase, a= 3.28±0.003Å
Specific mass (g/cm³)	4.51
Thermal conductivity (s.m.K)	22
Linear thermal expansion coefficient (α at 20°C)	$8.4\times10^{-6}K^{-1}$
Melting point (°C)	1670
Boiling point (°C)	3260
Alotropic transformation temperature (°C)	882.5
Shear module (GPa)	45
Tensile strength (MPa)	740
External electronic configuration	$3d^24s^2$
Eletronegativity	1,6
Eletrical resistance (W.cm)	47,8

1.2. Ti-Zr-Mo alloys

Among the binary and ternary alloys studied along the years, those with zirconium and molybdenum as alloying elements had presented advantageous properties, such as: a tensile strength superior to commercially pure titanium; relatively low specific mass; and good biocompatibility. Therefore, the development of new alloys with the Ti-Zr-Mo system was aimed regarding its potential for dental and orthopedic applications [28, 35-40].

Zirconium and titanium possess similar physical and chemical features, which contribute for the complete solid solubility of both elements. Also, zirconium presents the same structure as titanium (HCP, α-phase). Thus, its addition to the alloys is known to increase corrosion resistance, biocompatibility improvement and a slightly decrease to the melting point [39-42]. Molybdenum, however, has a body centered cubic structure (BCC, β-phase) and its addition to a titanium alloy contributes to its hardening, decrease in its elastic modulus, yield strength and the decrease in the allotropic transition temperature [26, 35, 39, 40].

Martins Júnior et al. [37] investigated the Ti-15Mo alloy produced by an arc-melting furnace and then characterized in terms of its structure, microstructure, mechanical properties

and cytotoxicity. Results indicated that the alloy presented a β-phase predominance with an increase of specific mass and microhardness. Also, it was observed that the studied alloys had a decrease in the elastic modulus and presented no cytotoxic effects. Furthermore, in another research, Martins Júnior et al. [43], studied the influence that the oxygen content had to the microstructure, mechanical properties and biocompatibility in the same Ti-15Mo alloy composition. The results obtained showed that both hardness and elastic modulus were influenced by the presence of the interstitial element, but no direct correlations were observed. The microhardness presented an increase with the addition of the oxygen to the alloy, but no significant difference was further observed regarding the increase of the oxygen concentrations values. In the other hand, the elastic modulus presented a decrease at first, when the interstitial element was introduced to the alloy, and then an increase in its values with the concentration of the oxygen. The mechanisms leading to the observed behavior was not discussed. Finally, the biocompatibility tests conducted showed no differences with the addition of the oxygen to the Ti-15Mo alloy.

In the work done by Vicente et al. [38], the influence of small quantities of oxygen in a Ti-xZr alloy system was analyzed. Along with the increase in the oxygen concentration, the zirconium's addition was also an important issue, where its concentration ranged from 5wt% (Ti-5Zr), 10wt% (Ti-10Zr) and 15wt% (Ti-15Zr). Regarding the microhardness, it was not significantly affected by the addition of oxygen to the Ti-5Zr alloy, while a decrease in the microhardness for the Ti-10Zr and an increase for the Ti-15Zr were observed. For the elastic modulus, the first two compositions presented no significant differences, but for the Ti-15Zr, however, a decrease was observed regarding its oxygen concentration. Once again, the mechanisms governing this behavior are still unknown. The biocompatibility tests showed no cytotoxic effects for any of the studied samples.

Because of the interesting results obtained in the above referred studies, the research and development of a new titanium alloy containing both zirconium and molybdenum was considered. In the works performed by Araújo et al. [44], Kuroda et al. [45-47], Correa et al. [10, 39, 48-52] and Xavier et al. [26, 40], the Ti-Zr-Mo system was deeply studied and characterized in terms of its structure, microstructure, mechanical properties and biocompatibility.

De Araújo et al. [44], studied the preparation and characterization of the Ti-10Mo-xZr system alloy, variating the zirconium concentration in 5, 10,15 and 20 wt%. It was observed

that with the increase in the zirconium concentration to the alloy, there was a suppression of the α'' phase by the predominant β phase, in which the microhardness values decreased. Also, it was corroborated the β stabilizer effect of zirconium when together with another β stabilizer [53, 54].

Kuroda et al. [45-47] studied the microstructural and mechanical characterization of a Ti-20Zr-xMo alloy as a function of thermomechanical treatments. With the increase in the molybdenum content in the alloy (2.5wt%, 5wt%, 7.5wt% and 10wt%), it was observed the β stabilizer effect of this alloying element, where it stabilizes completely the β phase with levels above 10wt%. For the lower concentrations of molybdenum, there is the presence of α' and α'' phase along with β phase. Also, because of this triphasic microstructure, the microhardness values increased with the addition of the molybdenum to the alloy, but decreased for the Ti-20Zr-10Mo alloy, which is composed only for the β phase. For the elastic modulus, there was no significant differences between the studied alloys, except for the Ti-20Zr-7.5Mo alloy, that showed higher values which along with its higher microhardness suggested the possibility of ω phase precipitation in this particular alloy. The thermomechanical treatments performed in the alloys showed that the hot-rolling presented the most significant results with the microhardness and elastic modulus of the studied alloys. However, no significant differences could be observed with the homogenized and annealed treatments when compared with the as-cast alloys.

In the works performed by Correa et al. [10, 39, 48-52] a deep study was carried out involving the preparation, characterization and heat treatments effects of both Ti-15Zr-xMo and Ti-15Mo-xZr systems alloys, where the molybdenum and zirconium contents were 5, 10, 15 and 20wt%. In terms of microstructure, it was possible to observe the β stabilization effect of both molybdenum and zirconium. However, the Ti-15Mo-xZr alloy showed only a β phase structure, while the Ti-15Zr-xMo only presented β phase predominance for the higher content of molybdenum (Ti-15Zr-15Mo). Regarding microhardness, both systems presented similar tendencies, with an increase in the microhardness for the 10wt% alloys and a decrease for the Ti-15Zr-15Mo alloy. The heat treatments carried out were homogenization, solubilization, oxygen doping and aging. It was observed that for the 5, 10 and 15wt% Ti-15Zr-xMo alloys, the microhardness was not significantly affected, except for the Ti-15Zr-20Mo where a small decrease for the homogenized, solubilized and oxygen doped samples was observed. A more significant decrease was observed for the aged samples. Concerning elastic modulus, there was

a decrease in these values up to the Ti-15Zr-15Mo alloy and then an increase for the Ti-15Zr-20Mo alloy. Also, the aging heat treatment presented distinct high values when compared with the other heat treatments. Lastly, the cytotoxicity test indicated that the studied alloys presented no observable or tolerable cytotoxicity levels when in contact with cells.

Xavier et al. [26, 40], studied the effects of different heat treatments parameters on the microstructure and mechanical properties of a Ti-15Zr-xMo system alloy, with the increase in the molybdenum content of 5, 10, and 15wt%. The heat treatments were performed at relatively low temperatures (600 ºC), different times (6, 12 and 24h), as well at temperatures above the β-transus (900 and 1000 ºC) with different cooling rates (fast and slow cooling rates). The results showed that the lower temperature heat treatments (600 ºC) were the cause of the α′ phase growth in the β phase alloys (Ti-15Zr-10Mo and Ti-15Zr-15Mo). For the high temperature heat treatments (900 and 1000 ºC), the cooling rate presented more significant variations on the β phase alloys (Ti-15Zr-10Mo and Ti-15Zr-15Mo), where the slow cooling rate allowed the growth of α′ phase, whilst the fast cooling rate presented α′′ phase. In general, the microhardness followed a similar tendency observed by Kuroda et al. [46] and Correa et al. [39], with an increase in the microhardness up to 10wt% Mo and then a decrease for the Ti-15Zr-15Mo alloy.

Because of these results, the Ti-15Zr-15Mo alloy presented the most interesting and promising properties for use in load-bearing implants. Therefore, investigation of surface properties (corrosion and tribocorrosion) was carried out to further knowledge of this alloy.

1.3. Surface treatments and Micro-arc oxidation as a functionalization process

Although titanium and its alloys exhibit excellent properties for its biomedical application, when used inside the body in a medical device capacity, the implanted material is subject to constant loads, which could lead to the occurrence of micro-movements and consequently damage by mechanical wear. At the same time, it also suffers the corrosive action from the body environment fluids. That combination of both mechanical wear and electrochemical corrosion is defined as tribocorrosion. It is estimated that for hip prostheses,

about 20-30% of implant failure is attributed to the tribocorrosion side effects in the human body [55-59]. Therefore, in addition to address the bulk properties of the material to be used as a medical implant, it is also necessary to perform a surface treatment in order to increase its resistance to tribocorrosion, thus increasing the patient's quality of life and the implant's life expectancy [9, 18, 52, 60].

1.3.1. Surface modification techniques

The most common surface modification techniques for titanium and titanium alloys can be divided in mechanical methods, physical methods and chemical methods (Fig. 1). The mechanical methods, such as machining, blasting, grinding and polishing, are usually employed in order to obtain certain surface topographies and/or remove surface contaminants. On the other hand, physical methods, mostly plasma-based techniques, are mainly used for the preparation of coatings and/or surface doping. Lastly, the chemical methods are a bit more diverse; acid etching, sol-gel, and chemical vapor deposition (CVD), can be used to prepare and produce a variety of thin films at the surface [61-63].

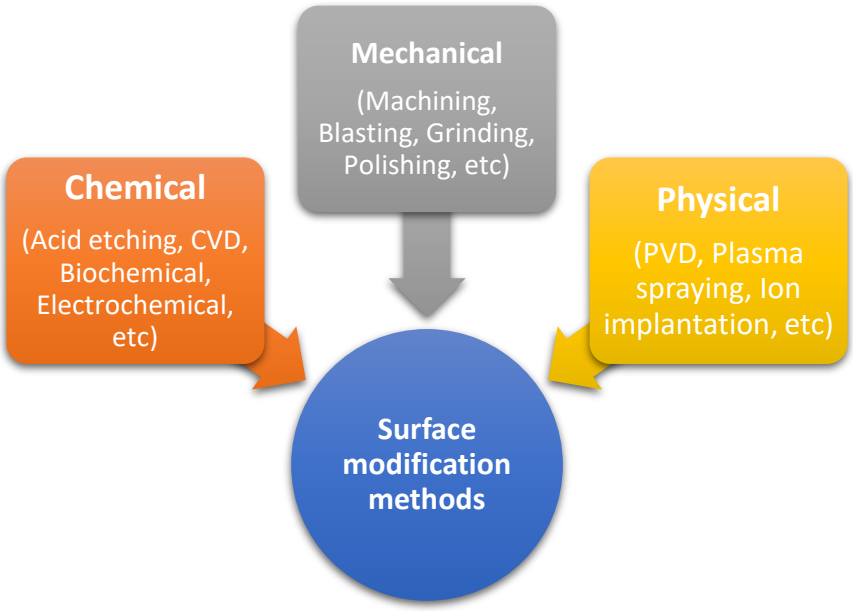

Figure 1 - Most common surface modification techniques used for titanium and titanium alloys [61, 63].

Among these surface modification techniques, electrochemical methods, due to their low-cost, are promising for the development of new biomaterials. Furthermore, they allow large-scale production, and the manipulation of processing parameter is relatively simple. The most common electrochemical modification technique used for the surface treatment of titanium and titanium alloys for biomedical applications is the anodization. Anodization is usually employed to build compact or porous oxide layers, nanotubes, nanopores, nanorods and any micro or nano texture on Ti-based material surfaces, through the reaction of the surface of the alloy. An interesting method of anodization is the micro-arc oxidation (MAO), known to tailor and construct microporous with biofunctional elements on the surface materials [61-64].

The traditional electrochemical anodization technique is responsible to grow compact and protective barrier-type oxide layers on the surface of the studied metals and its alloys. The procedure takes place with the current metal of interest serving as anode whilst the counter-electrode is usually an inert material, such as graphite or a platinum sheet. The electrolytes can be composed of various reagents in which with a sufficiently high voltage power source, it's possible the conduction of ions and electrons across the native oxide film and electrolyte. The ion conduction is the cause for the oxide growth in the surface materials, while the electron conduction is responsible in the evolution of oxygen from the anode surface following the reaction in equation (1). As the oxide film grows, the electron conduction decreases whereas the ion conduction becomes the dominant contributor to the current flow. At this stage, oxidized Ti^{4+} species formed at the metal/oxide interface are diffused outward, while oxygen ions (O^{2-}) migrates inward, coming from the H_2O deprotonation at the oxide/electrolyte interface. Because of this ion migration, the oxide is grown at both interfaces following equations (2)-(4) [61, 63-65].

$$2H_2O \rightarrow O_2 + 4H^+ + 4e^- \quad (1)$$

$$Ti \rightarrow Ti^{4+} + 4e^- \quad (2)$$

$$H_2O \rightarrow O^{2-} + 2H^+ \quad (3)$$

$$Ti^{4+} + 2O^{2-} \rightarrow TiO_2 \quad (4)$$

The growth and thickness of this oxide layer is limited and proportional to the applied voltage, where this limit is called dielectric breakdown. However, when the applied voltage is higher than the dielectric breakdown of the oxide layer, there is an increased gas evolution and an occurrence of sparks discharges. This kind of anodization is called micro-arc oxidation (MAO), and will be addressed in more detail in the next section [61, 63, 64].

1.3.2. Micro-arc Oxidation (MAO)

As already stated, surface treatments allow the surface of the material to be bio-functionalized with agents that are responsible for improvements in the bioactivity of the material, thus increasing osseointegration and regeneration of the adjacent tissue. In fact, there are several works found in the literature corroborating that porous surfaces functionalized with elements such as Ca, P, Zn and Mg increases the interaction of the surface to bone cells (osteoblasts) and its adhesion to the surface's material. The incorporation of bioactive elements such as calcium and phosphorus, improves the biological performance of the implanted materials, since they are native elements present in the bones [33, 60, 66-69]. Also, the use of particles such as Al_2O_3, ZnO and HAp, in addition to promoting better biological properties, contributes to the improvement in the mechanical properties of the material's surface, minimizing the effects of corrosion and tribocorrosion [55, 56, 70]. Alumina (Al_2O_3) is known to promote the mechanical wear resistance and, consequently, reducing problems related to the release of debris or metal ions through wear and/or tribocorrosion. Hydroxyapatite ($Ca_{10}(PO_4)_6(OH)_2$) is a ceramic material considered ideal for the coating of metallic biomaterials, having almost total similarity to the bone's chemical composition inorganic tissues. ZnO, besides promoting the above-mentioned surface properties, it's also known for its

antimicrobial action, which can be useful for combating inflammatory issues from the surgery procedure [18, 19, 55, 70-72].

Many techniques for surface modification have been used over the years, aiming at better biological properties, and thus increasing osseointegration and implant success. For this purpose, it is very important that the surface treatment is able to manipulate the microstructure and the surface properties of the material, such as porosity, roughness, structure and composition, as well as improve the tribological properties [21, 73-75]. In this case, the MAO technique is a widely used method, based on the electrochemical anodization of the material's surface, in order to form a protective oxide film. Basically, the procedure performs an anodic oxidation of the surfaces material by applying a positive voltage to the substrate, which is used as an anode immersed in an electrolyte, as can be seen by Fig. 2. When the applied voltage is relatively high, there is the presence of micro-arcs, that are generated as a result of a dielectric breakdown on the surface of the oxide layer. The highly energetic micro-arcs cause a localized melting of the oxide, where in contact with the electrolyte it quickly solidifies, allowing elements of the electrolyte to be incorporated into the new formed film [30, 73, 76, 77]. Its advantages include being a remarkably simple technique, which results in strong adhesion between the oxide layer and the substrate and allows the control of morphology and chemical composition of the surface varying the anodizing conditions. In fact, the properties of the new formed oxide layer depend on the parameters of the process, such as the applied anodic voltage, electrolyte composition, time, and temperature. Studies indicate that when high voltage values are applied, there is a formation of thicker oxide films and greater porosity. On the other hand, lower voltage values are responsible for thinner and more compact films, as discussed above [30, 73, 78, 79].

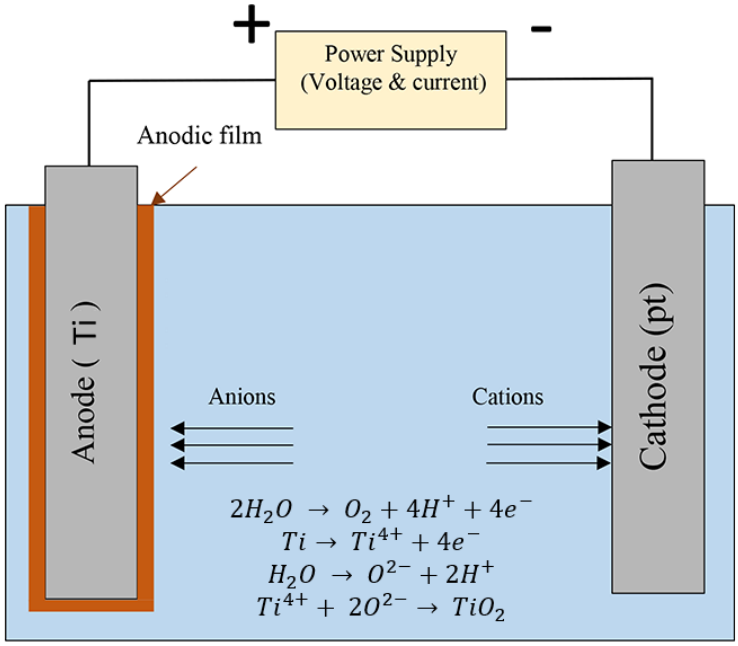

Figure 2 - Schematic representation of the anodization process [80].

1.3.3. TiO_2 structure and characteristics

Titanium dioxide (TiO_2) can be naturally found in three allotropic phases: anatase, rutile and brookite, whereas anatase and rutile are currently the most interesting phases for biomedical applications. In fact, rutile, which is considered stable at room temperature, it's known due to its high refractive index values, therefore is commonly used in optoelectronics, semiconductor devices and optical coatings. In the other hand, anatase is considered a metastable phase, where it is shown most efficient for photovoltaic applications, Li-ion electrodes batteries and photocatalysis for water and air purification [81-83]. Both anatase and rutile present a tetragonal structure, but with anatase phase exhibiting a prolonged shape, therefore, a greater cell volume (Fig.3). Although the differences between these two phases, studies show the possibility for the anatase phase transformation to the rutile phase when the structure is put under high temperatures, ranging between 400 – 1200 °C. In fact, this transformation is dependable to various parameters, such as: particles shape and size; pressure; sample volume; heating rate; and impurities [81-83]. Depending on the phases that are formed, there is a better biocompatibility and mechanical performance for biomedical applications. An adequate ratio between the amount of rutile and anatase crystalline phases, together with a small

portion of amorphous phase, can significantly improve the tribocorrosion behavior, while improving the osseointegration capacity, and even antimicrobial properties [30, 33, 73, 79, 84].

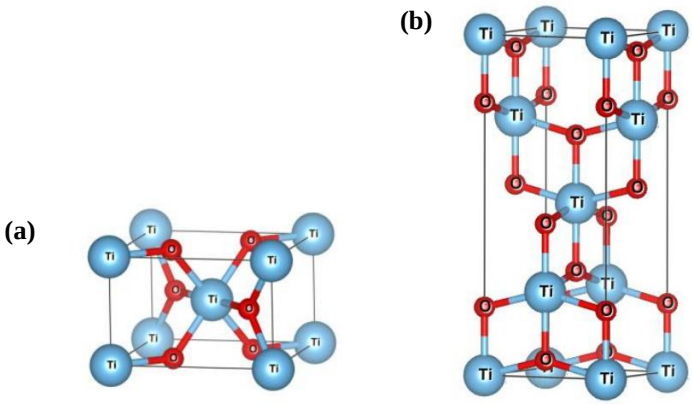

Figure 3 – Tetragonal phase structures of: (a) Anatase (I41/amd); and (b) Rutile ($P4_2/mnm$) [82, 85].

1.4. Electrochemical and Tribocorrosion analysis

Corrosion process is the reaction of any metal with its surrounding environment, where the degradation occurred results in a deterioration of the metals properties. It's commonly observed and addressed among metals in every aspect of its applications. Focusing on metallic biomedical materials, decrease of the structural integrity of implants and the release of corrosion products in the adjacent tissues and the adverse reactions that might occur, are of particular concern [62, 86, 87]. When a metallic implant is inserted into the human body, it will be in contact with complex physiological fluids, different pH, variation of temperature and multifaceted chemical compositions, including the presence of different biomolecules, cells and microorganisms. Also, as the metallic biomaterials used in biomedical application are passive, they are prone to localized corrosion, which can lead to cracks, mechanical instability and possible implant failure [62, 88].

On the other hand, although the usual negative remark of the term corrosion, there are some electrochemical reactions considered as a positive outcome for its material. That depends

on the reaction products being protective or non-protective, as well as the speed and extent of the reaction. For instance, titanium is known for its passive oxide film, which occurs naturally due to the oxidation process on its surface, leaving the titanium surface with a reaction product that is protective against the surrounding environment and slows further active corrosion. Thus, the passive film protection can be evaluated by the ion release rate over the film and its stability against dissolution. Also, the anodization process is nothing but a controlled corrosion process, where it's possible to produce not only protective films to the surface of metallic biomaterial but also functionalize it with elements that improves its application [62, 87, 89, 90].

Titanium and titanium alloys are relatively resistant to corrosion, however, its known that one of the main factors that influences corrosion for titanium in physiological environments is the pH, or rather, the pH variation from different acids. Besides, under physiological conditions, other factors can affect the electrochemical behavior during its application, such as: the presence of bacteria, microbial agents, and/or proteins, which may adsorb to the implants surface [91-95].

For this purpose, Tafel's extrapolation is one of the most popular DC techniques for estimating the corrosion rate of studied samples. The correct extrapolation of the anodic and cathodic Tafel lines, regarding the charge transfer controlled reactions, provide two of the main potentiodynamic polarization analysis: the corrosion current density (i_{corr}); and the corrosion potential (E_{corr}), where they can be obtained from the intersection of the linear anodic and cathodic branches of the polarization curves (Fig. 4). Also, for an accurate extrapolation, two rules should be used with the Tafel extrapolation technique: at least one of the branches of the polarization curve ought to exhibit a linear on semilogarithmic scale, over a minimum of one decade of current density; and the extrapolation should start at least 50-100 mV away from the corrosion potential [96, 97].

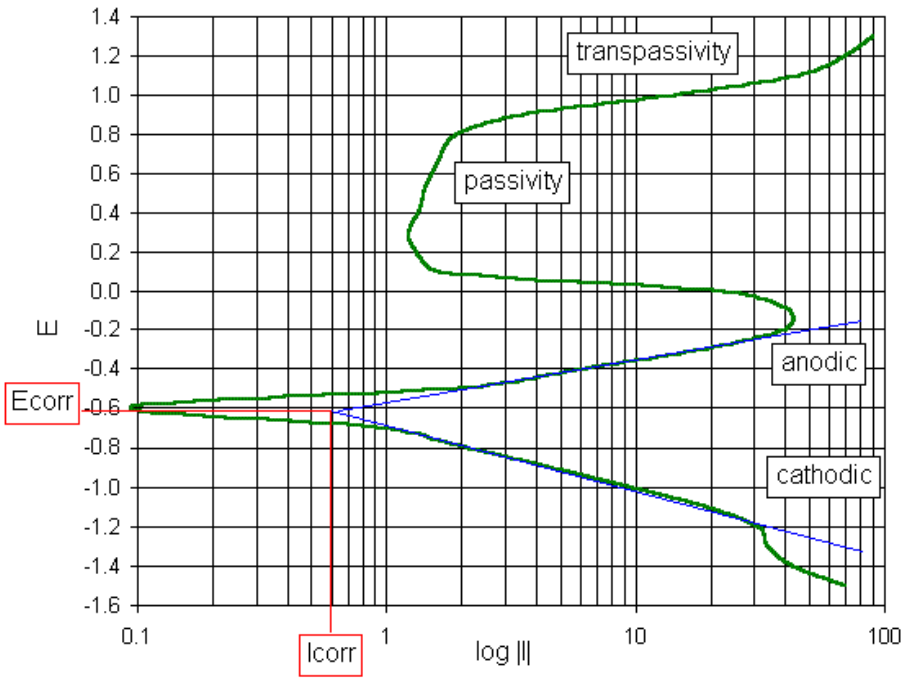

Figure 4 - Tafel region extrapolation [98].

On the other hand, Electrochemical Impedance Spectroscopy (EIS) is an electrochemical measurement technique with multifrequency AC. The results are obtained by measuring the impedance (electrical resistance) of the metal/solution interface between a determined range of frequencies. In fact, this data is obtained by applying an AC potential to an electrochemical cell, then measuring the AC current's response and the recording of phase shift and amplitude variations through a range of applied frequencies. By EIS it is possible to relate theoretical circuit elements to actual electrochemical processes that occurs in a material's surface, allowing for the fitting of current, voltage and frequency data to an equivalent circuit model [99-101]. The analysis of impedance data is commonly carried out with the Nyquist and Bode plot diagrams, where it's possible to determine the individual components of the equivalent electrical circuit model that represents the studied surface. The Nyquist plot graphs the resistive (a) *versus* the reactive (b) components of impedance, Z, whilst the Bode plot exhibits both the modulus of impedance (r) and phase angle (θ), *versus* the frequency (f), in a logarithm graph (Fig. 5). The purpose of this methods is not only to determine an equivalent electrical circuit that represents the studied surface, but also to obtain the circuits individual components values. The combination of resistors and capacitors in the equivalent electrical

circuit used for the representative model, gives characteristic plot shapes in both Nyquist and Bode obtained diagrams (Fig. 6). Therefore, the analysis of these plot shapes allows the calculation of the individual component values, as well as how they are combined together [102, 103].

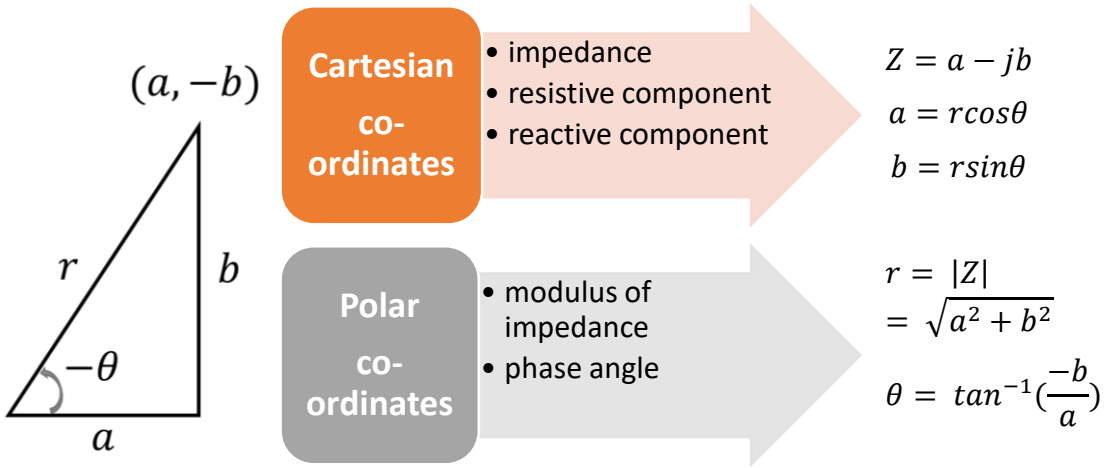

Figure 5 - Definition of impedance relationship in Cartesian coordinates (a,b) and polar coordinates (r, θ) [102].

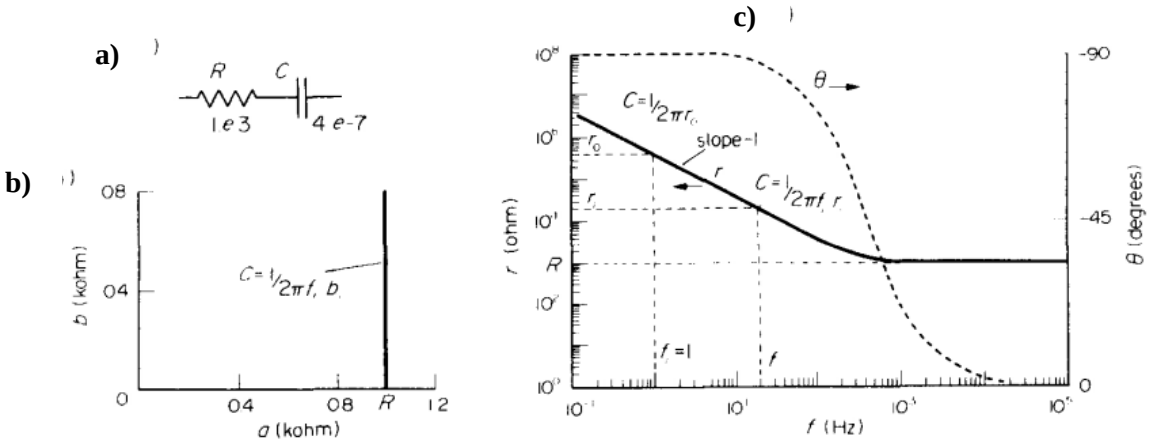

Figure 6 - Example of : a) a series resistor (R) and capacitor (C) combination; b) Nyquist; and c) Bode impedance plots [102].

Besides the electrochemical analysis of the biomaterials surface, the tribocorrosion behavior is an important characteristic among the biomedical applications devices due to the release of metal ions and possible wear particles that can produce adverse reaction in the adjacent human tissue. As referred, tribocorrosion can be define as the combination of both mechanical wear and electrochemical corrosion. When the implanted material is subject to constant loads, that can consequently be damaged by mechanical wear, while at the same time, suffers the corrosive action from the body environment fluids. For this purpose, researches and developments for biomaterials with better tribocorrosion behavior have increased over the years [10, 55-59, 62]. The tribocorrosion behavior is known for the combined conditions of corrosion and mechanical loading at the materials surface. Also, among them, there is another worth mentioning well-known characteristic: the synergism. The synergistic relation between the corrosion and wear can bring both positive and negative aspects to the system; whether helping with the formation of self-lubricant and/or self-healing layers; or causing an amplified degradation of the surface [62, 104]. In fact, the corrosive environment contributes to the amplification of the wear mechanisms, as well as, the wear processes can affect a materials corrosion rate when the protective passive film is removed. In this regard, the synergistic mechanisms that are in work throughout a tribocorrosion process are complex and difficult to identify. Some of the main contributors to the synergistic mechanisms are well known and have been deeply studied, such as: the formation of wear debris; the galvanic coupling between worn and non-worn areas; and the accumulated dissolved species in the electrolyte around the contact zone [55-59, 62, 90, 105].

Although its complex and difficult behavior to simulate, the tribocorrosion can be investigated with an *in situ* device (Fig. 7), where a tribometer is coupled with an electrochemical Potentiostat/Galvanostat. Thus, the evolution of the mechanical properties of the contact (coefficient of friction) and the corrosion parameters (open circuit potential and current density) are monitored and plotted for the tribocorrosion analysis of the surface [62].

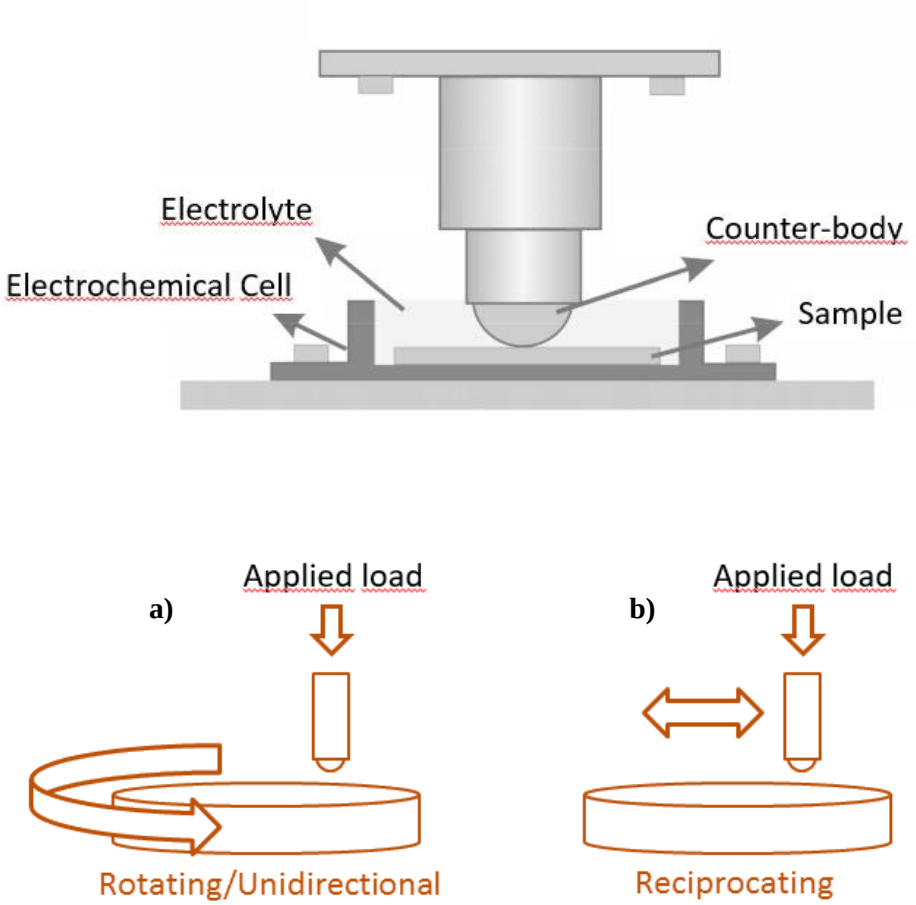

Figure 7 - Illustration of a tribometer with its different motions of operation: (a) rotating/unidirectional; and b) reciprocating motion [106, 107].

2. OBJETIVES

The main objective of this work was the development and characterization of a functionalized surface on a β type Ti-15Zr-15Mo alloy, through micro-arc oxidation. A deep characterization of the microstructure, corrosion and tribocorrosion behavior was carried out. For this purpose, cp-Ti and Ti-6Al-4V were used as control groups, in order to understand and correlate the results obtained in the Ti-15Zr-15Mo alloy.

The specifics objectives of the work were:

1) The functionalization of the Ti-15Zr-15Mo, and control group samples through micro-arc oxidation to create a porous titanium oxide film doped with Ca and P bioactive elements.
2) The incorporation of particles in the porous film through the anodization process, such as ZnO and HAp.
3) To understand the mechanisms leading to the film creation.
4) Characterization of the produced films by means of structure, microstructure and chemical analysis.
5) Electrochemical and Tribocorrosion analysis for the untreated and MAO produced samples.

3. MATERIALS AND METHODS

3.1. Studied materials

Cp-Ti grade II and Ti-6Al-4V grade V were used as control groups. As for the Ti-15Zr-15Mo alloy, it was produced by an arc-voltaic melting furnace composed of a non-consumable tungsten electrode, a water-cooled copper crucible and under argon atmosphere (Fig. 8). The raw materials are weighted in an analytical scale with the aimed proportion to obtain the Ti-15Zr-15Mo alloy, then etched and cleaned with propanol and distilled water.

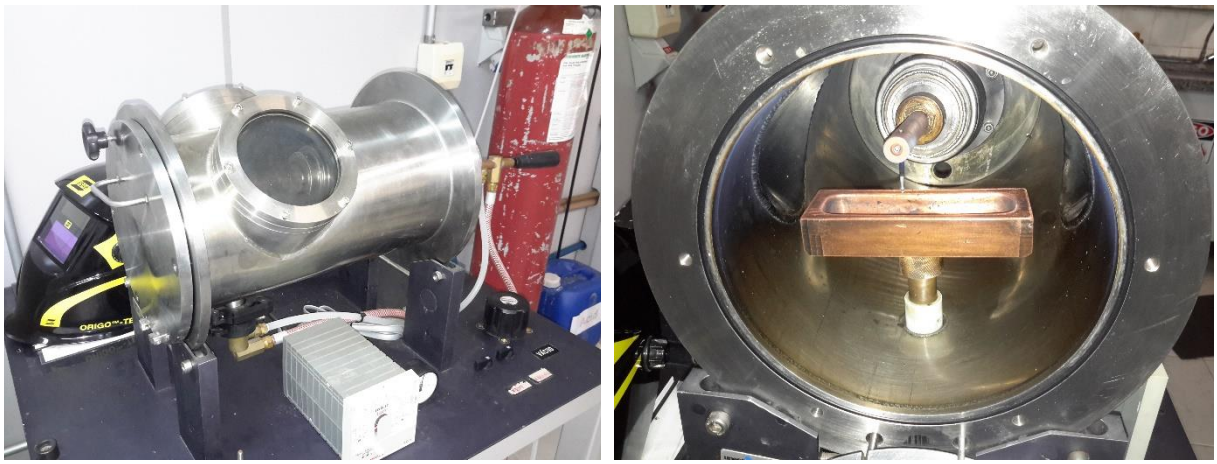

Figure 8 - Arc-melting furnace system

The Ti-15Zr-15Mo ingot was produced in the Laboratory of Anelasticity and Biomaterials (UNESP-Bauru), supervised by Prof. Dr. Carlos Roberto Grandini, where the arc-voltaic furnace was acquired with a FAPESP grant (proc. 06/00257-8). EDS and the specific mass measurements were realized to guarantee the quality and integrity of the produced alloy.

3.2. Arquimedes' Principle

For the specific mass measurements of the untreated cp-Ti, Ti-6Al-4V and Ti-15Zr-15Mo, the analysis was realized following the Arquimedes' principle, where the sample is immersed in a fluid and subjected to a buoyant force opposite to its weight. From this principle, the value of the force is proportional to the mass of the displaced fluid from the immersed sample, thus obtaining the relation from equation (5).

$$\rho_{sample} = \frac{m_{air}}{m_{air} - m_{fluid}} \rho_{fluid} \quad (5)$$

Where, ρ_{sample} is the samples' specific mass, m_{air} is the samples measured mass in air, m_{fluid} the samples' measured mass immersed in the fluid and ρ_{fluid} the fluid's specific mass.

The samples' mass was measured five times for each sample with an analytical scale, Explorer model, from Ohaus Corporation. Also, to determine the samples' specific mass, it was used distilled water as the immersing fluid, with a temperature of 21°C and, therefore, a 0,990 g/cm³ specific mass.

3.3. Material's surface preparation

In order to standardize the surface parameters for the Micro-arc Oxidation, corrosion and tribocorossion analysis, all samples proceeded with the same surface preparation as follows.

First, the samples were grounded down with #1200 mesh SiC papers with water, then ultrasonically cleaned with propanol and distilled water for 15 minutes. After that, the samples were chemically etched in Kroll's reagent (2 ml HF, 10 ml HNO_3, 88 ml H_20) for 10 min. Then,

the samples were again ultrasonically cleaned with propanol and distilled water, for 10 and 5 min, respectively.

3.4. Micro-arc oxidation (MAO)

The functionalization of the surface was realized by anodic treatments with electrolytes containing CA ($C_4H_6CaO_4$) and β-glicerolphosphate ($C_3H_9O_6P$) with the concentrations of 0.35M and 0.02M, respectively. In Fig. 9 it is shown the anodization system used for the MAO process. The anodic treatment was realized at room temperature with a DC power supply (GPR-30H10D) at 300 V and 2.6 A during 1 min, with Pt foil as cathode and in a sample area of 0.38 m^2 using Vitton o-rings [30]. Also, it was added ZnO and HAp particles to the electrolyte with the concentrations of 2 and 5 g/l each, intending to the incorporation of particles in the oxide films [57, 73, 78]. These particles were added and ultrasonic dispersed in the electrolyte just before the anodization process using a Hielscher ultrasonic processor, model UP200St (Fig. 10), during 5 min at 150W. For the HAp particles, it was used in solid form (powder), from MERCK, with a mean particle size of 2-20 μm and molar mass of 502.32 g/mol. On the other hand, the ZnO particles used were from SIGMA-ALDRICH, in solid form (powder) and molar mass of 81.39 g/mol. In Fig. 11, SEM images of the powder materials are presented, and in table 2 are summarized their EDS chemical analysis data (Fig. 12).

From the anodization process, it was obtained the current density versus time graphs (anodization curves). The current variation values obtained during the anodization process are divided by the sample surface area (0,38 m^2), hence the current density is calculated and plotted versus the anodization time. Also, from these plots, the charge values (q) related to the anodization process were obtained by integrating the curves through Origin software.

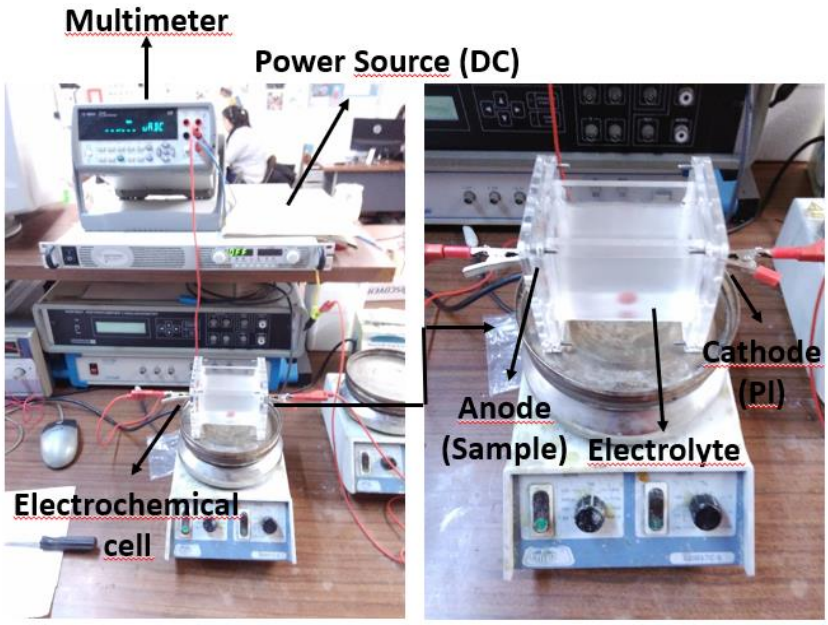

Figure 9 - Anodic treatment system.

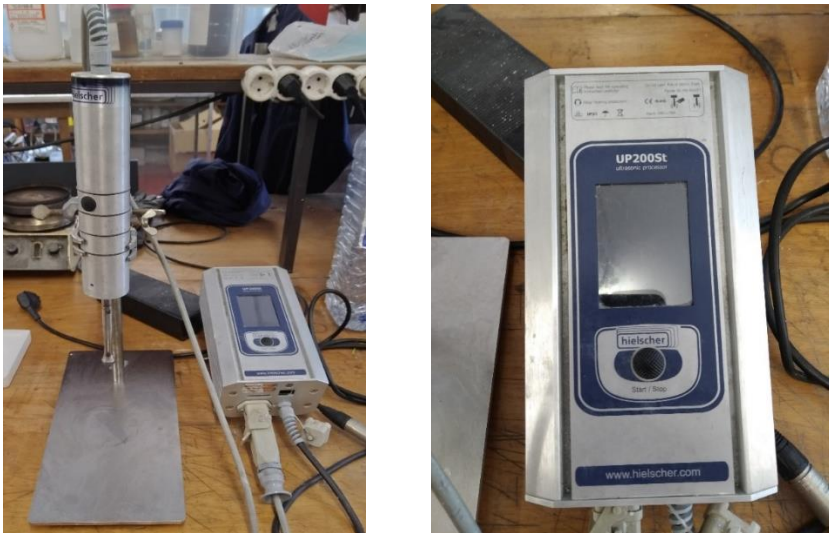

Figure 10 - Ultrasonic processor for the particle's dispersion in the electrolyte.

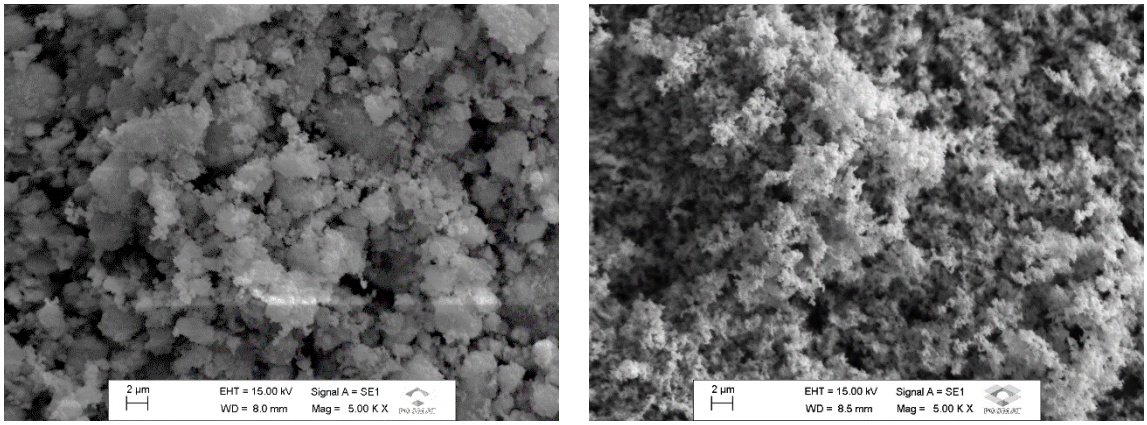

a) b)

Figure 11 - SEM images of the: a) Hydroxyapatite (HAp); and b) Zinc oxide (ZnO) particles.

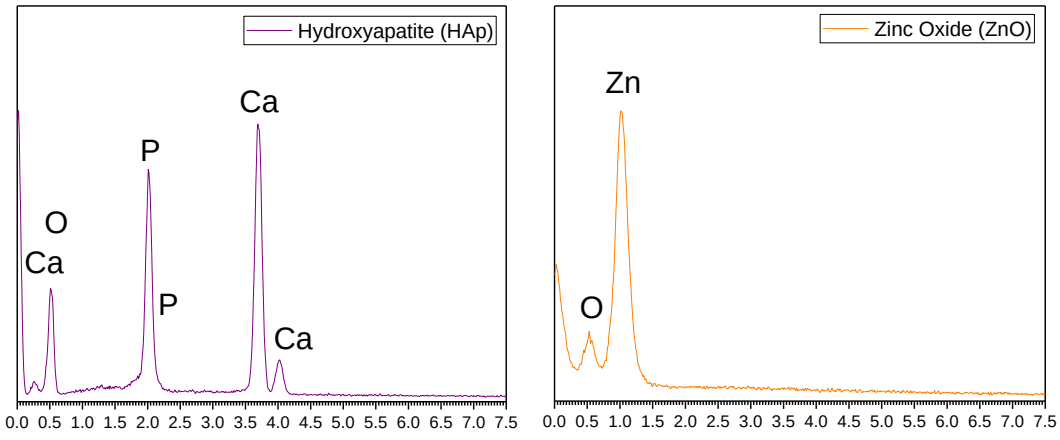

a) b)

Figure 12 - Qualitative chemical analysis from the EDS of the: a) Hydroxyapatite (HAp); and b) Zinc oxide (ZnO) particles.

Table 2 - EDS – Semi-quantitative analysis of the chemical composition from the HAp and ZnO particles.

	Ca (at.%)	P (at.%)	Ca/P	O (at.%)	Zn (at.%)
HAp	22.28 ± 0.31	12.88 ± 0.12	1.70 ± 0.01	65.20 ± 0.44	-
ZnO	-	-	-	51.82 ± 1.83	48.18 ± 0.1.83

3.5. Microstructural Analysis

The structural and microstructural analysis were realized by X-ray diffraction (XRD), optical microscopy (OM) and scanning electron microscopy (SEM). X-ray diffraction was performed with a Bruker D8 Focus diffractometer, where the analysis was made with CuKα radiation in the scan range 2θ from 20° to 80°, with step size of 0.04° and step time of 1 s. All indexed XRD cards used for the peak's identification are in the annex of this work. The surface morphology was analyzed using a Leica DM2500 OM and a Nano FEI Nova 200 field emission gun scanning electron microscope equipped with an energy dispersive spectrometer (EDS). Also, a Ti-15Zr-15Mo sample cross-section was obtained through precision cuts from a Focused Ion Beam (FIB). The cross-section equipment consists of a Tescan Lyra 3 dual beam microscope with gallium ions and an electron beam (FIB-SEM). For this analysis, first it was performed the deposition of a platinum protective layer through the ion beam with 30 keV of energy and 0.2 nA of current. Then the trench is formed with the ion beam under 30 keV of energy and 5 nA of current. After that, a fine polishing is realized with the ion beam under 30 keV of energy and 1 nA of current, in order to reveal the oxide film and substrate interface [108].

From the XRD spectra, the structure and phase percentages (distribution) of the TiO_2 anodic layers are analyzed and calculated with the following equation (6).

$$\%phase_{\alpha} = \frac{\sum I_{\alpha\ peaks}}{\sum I_{all\ peaks}} \quad (6)$$

Where a certain phase percentage (%phaseα) is determined by the sum of the phase's intensity peaks ($\Sigma I_{\alpha peaks}$), divided by the sum of all intensity peaks ($\Sigma I_{allpeaks}$).

Also, the pore/size distribution analysis of the produced porous oxide film was evaluated through Fiji Software (ImageJ). For this analysis, SEM images with a 5.000x magnitude were selected, where 15 lines were drawed with 2 cm apart. All pores under the

drawed lines were measured, where each pore size was obtained by mean value between the bigger diagonal and the smaller diagonal of the pore (Fig. 13). This analysis was realized for three times for each produced surface, hence, nine times total for each studied sample. With the pore size results obtained, it was realized a frequency counts statistical analysis using Origin software, where it was possible to plot a frequency versus pore size graph.

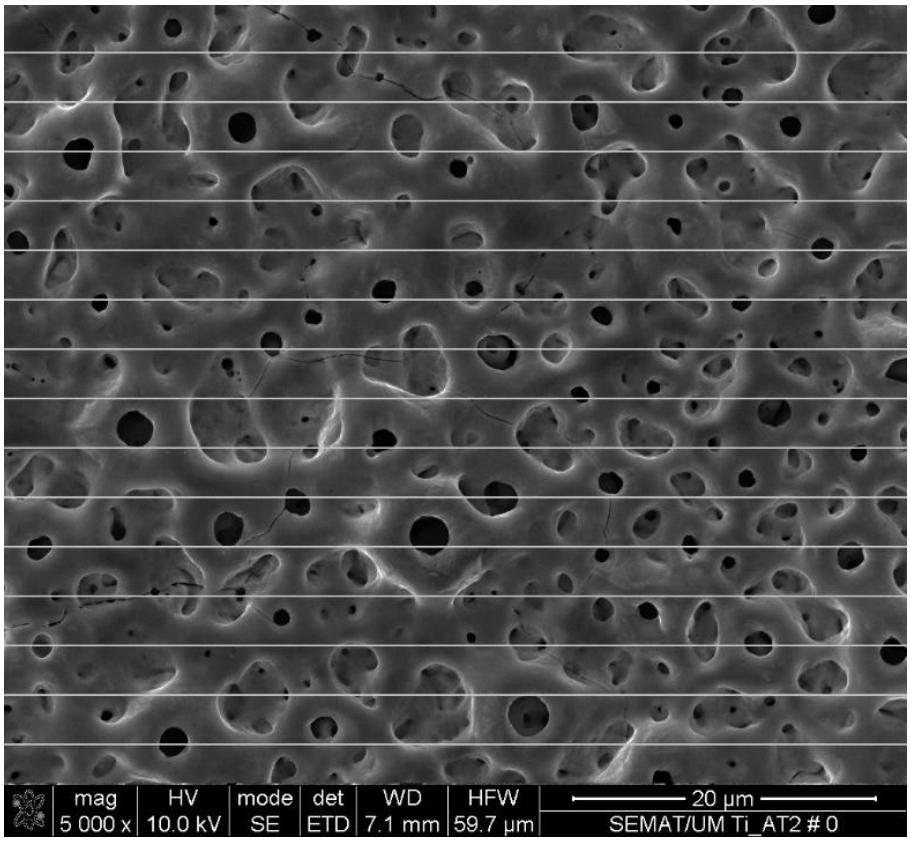

Figure 13 - Representative image of a pore size/distribution analysis with Fiji Software.

3.6. Corrosion and tribocorrosion experiments

Corrosion and tribocorrosion were performed in triplicates with a 9 g/l electrolyte of NaCl at body temperature (37 ± 2 °C). NaCl, being the simplest saline solution used to mimic biological fluids, was chosen in order to allow comparison of the results with previous published works. The corrosion tests were realized using a Gamry Potentiostat/Galvanostat (model Reference-600) by means of electrochemical impedance spectroscopy (EIS) and potentiodynamic polarization (PDP), which system can be seen in Fig. 14. The experiments followed a three-electrode configuration with the samples acting as working electrodes, a saturated calomel electrode (SCE) (Hg/Hg_2Cl_2/saturated HCl solution, SCE = +244 mV/NHE) as reference and a platinum electrode as counter electrode; with an electrochemical cell (adapted from ASTM:G3-89) containing 180 ml of fresh electrolyte. EIS measurements were performed after three hours of stabilization time at open circuit potential (OCP) with a scanning range of 100kHz till 10 mHz. Potentiodynamic polarization was performed after 10 min of OCP (-0.25VOCP till 1.50 VSCE) with a scan rate of 0.5 mV/s. Tribocorrosion experiments were performed using a couple Gamry Potentiostat/Galvanostat (model Reference-600) to a pin-on-disc tribometer (CETR-UMT2) operated in reciprocating mode using an alumina ball (10 mm in diameter) as a counter-body, the samples as working electrode and the platinum electrode as counter. OCP measurements were recorded before, during and after sliding. Tests were carried out with an applied normal load of 1 N, frequency of 1 Hz and a total stroke length of 6 mm. The 1 Hz frequency corresponds to an average walking frequency. The applied normal load of 1N corresponds to an Hertzian contact pressure of 410 MPa. That is the maximum value of the yield strength for dense Ti (275-410 MPa), and yet, significant higher than the contact pressure reported for hip implants (3-9 MPa) [109, 110]. The sliding duration time was realized in 30 minutes. Also, the electrochemical cell used for the tests can be seen in Fig. 15 where red silica is applied at the surface's sample in order to control the intended target area that would be tested.

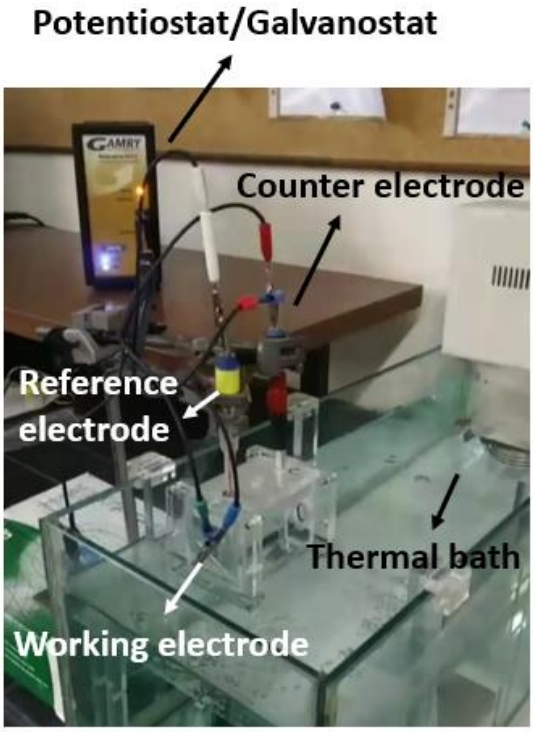

Figure 14 - Electrochemical Analysis system.

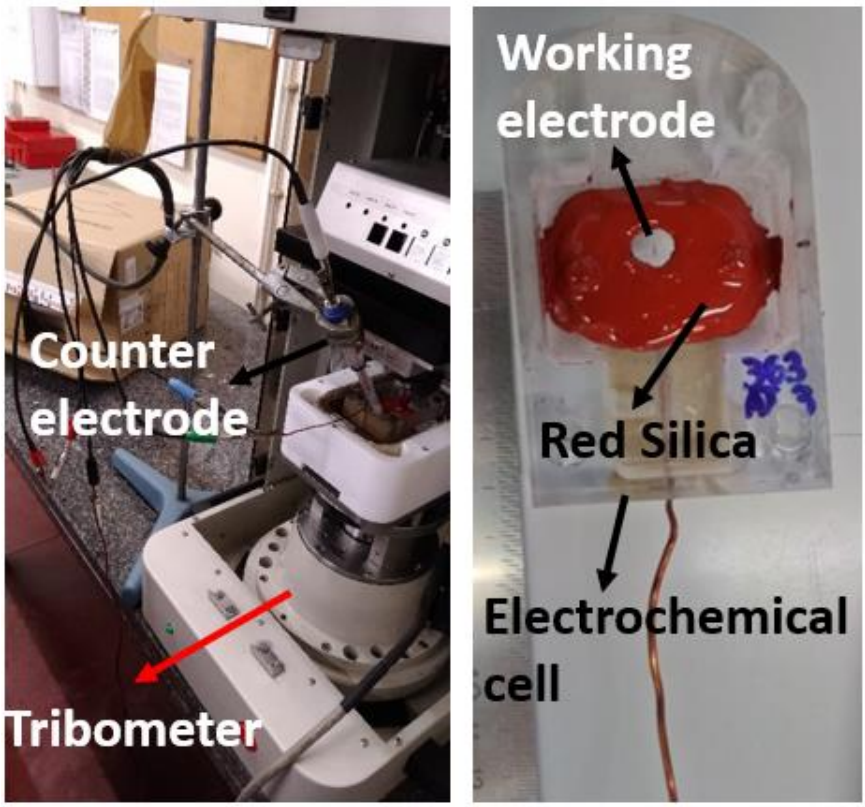

Figure 15 - Tribocorrosion system and electrochemical cell.

4. RESULTS AND DISCUSSION

4.1. Characterization of the untreated samples

First, EDS and specific mass measurements were carried out to verify the quality of the produced Ti-15Zr-15Mo alloy. For the EDS analysis, measurements were performed in five different regions of the samples in order to obtain a mean value. These results are summarized in table 3 and Fig. 16 presents the qualitative chemical analysis of the EDS for the commercially pure titanium (cp-Ti), Ti-6Al-4V and Ti-15Zr-15Mo alloy. For the evaluation of the specific mass, the values were obtained by Arquimedes' Principle and are presented in table 4.

Table 3 - EDS – Semi-quantitative analysis of the chemical composition from the untreated samples.

Sample	Ti (wt.%)	Al (wt.%)	V (wt.%)	Zr (wt.%)	Mo (wt.%)
cp - Ti	100	-	-	-	-
Ti-6Al-4V	89.06 ± 0.2	5.72 ± 0.4	5.23 ± 0.5	-	-
Ti-15Zr-15Mo	69.1 ± 0.6	-	-	15.4 ± 0.2	14.9 ± 0.7

Table 4 – Specific mass measurements for the untreated cp-Ti, Ti-6Al-4V and Ti-15Zr-15Mo samples.

Specific Mass	cp - Ti (g/cm³)	Ti-6Al-4V (g/cm³)	Ti-15Zr-15Mo (g/cm³)
Measured	4.50 ± 0.01	4.42 ± 0.03	5.24 ± 0.01
Theoretical	4.50	4.43	5.23

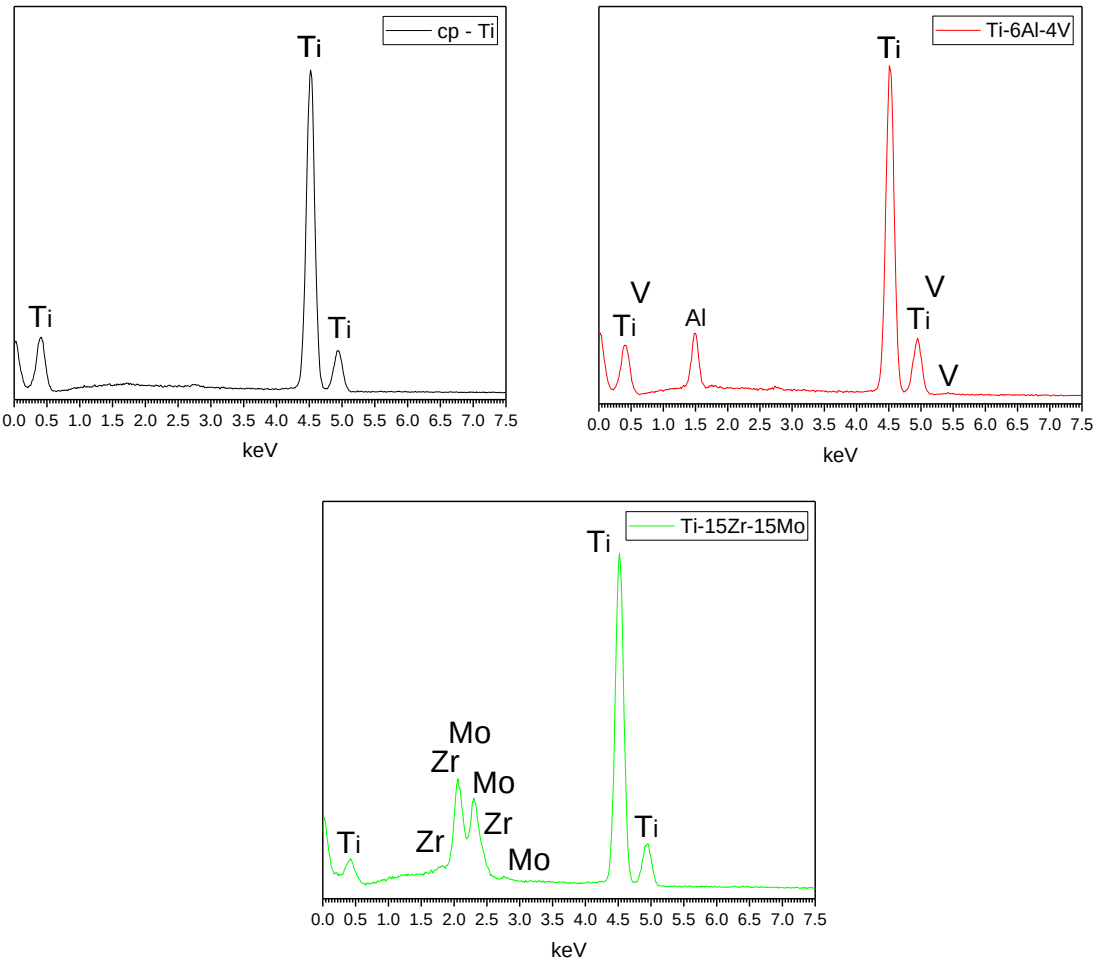

Figure 16 - Qualitative chemical analysis from the EDS of the untreated samples: cp-Ti; Ti-6Al-4V; and Ti-15Zr-15Mo.

From table 3, it is possible to verify the weight percentage regarding the untreated samples. For the commercial samples, cp-Ti and Ti-6Al-4V alloy, and the produced Ti-15Zr-15Mo alloy, the semi-quantitative analysis exhibited chemical compositions close to its nominal values. Also, for the Ti-15Zr-15Mo alloy, the EDS spectra showed only the presence of the alloying elements: titanium, zirconium and molybdenum. For the evaluation of the specific mass (table 4), it can be observed that the experimental results were close to the theoretical data. Furthermore, the Ti-15Zr-15Mo alloy presented slightly higher specific mass values than compared with the cp-Ti an Ti-6Al-4V alloy. As well known, for biomedical applications, specific mass is an impacting factor due to the possibility of bone loosening, bone loss or even eventual fracture. For successful biomaterials applications, lower values of specific

mass are required to diminish the possibility of implant failure [24, 25]. In Fig, 17 it's presented the optical and SEM images exhibiting the microstructure of the untreated samples.

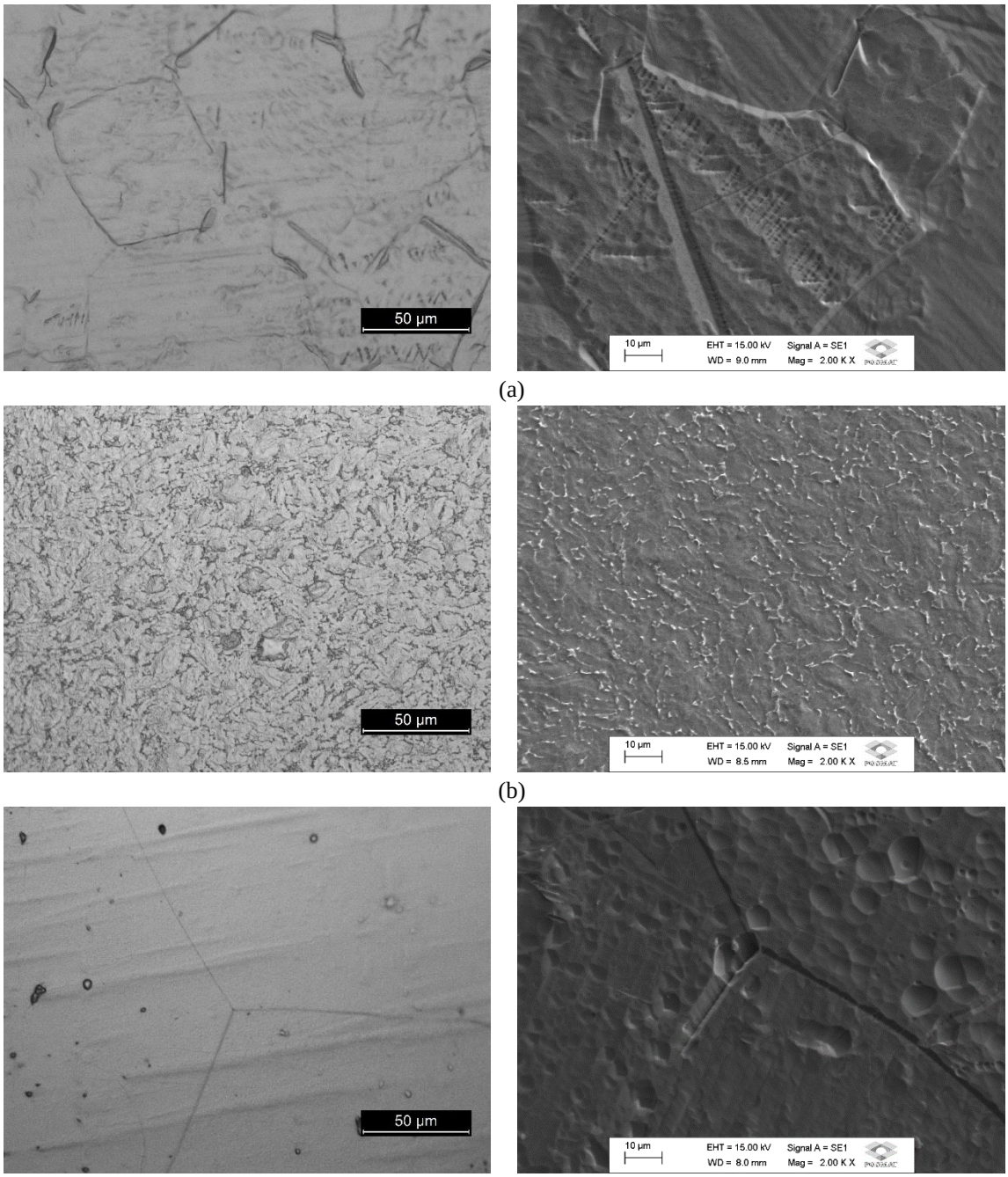

Figure 17 – Optical and SEM images of the a) cp-Ti, b) Ti-6Al-4V and c) Ti-15Zr-15Mo alloy.

As can be seen by the micrographs in Fig. 17, the cp-Ti (Fig. 17.a) shows α phase grains. As for the Ti-6Al-4V (Fig. 17.b), it consists of a fine grained α phase along with β particles at the grain boundaries. Lastly, the Ti-15Zr-15Mo (Fig. 17.c), presented a microstructure consisting only of β phase grains. Therefore, the cp-Ti showed only α phase and the Ti-6Al-4V a α + β phase microstructure, as well known in the literature [111]. While the Ti-15Zr-15Mo is a β phase alloy as discussed in other papers [10, 26, 49].

4.2. Micro-arc Oxidation without particles

In Fig. 18 the current density versus time plots are presented regarding the anodization process without particles for the cp-Ti (Ti-AT#0), Ti-6Al-4V (Ti-6Al-4V-AT#0) and Ti-15Zr-15Mo alloy (Ti-15Zr-15Mo-AT#0). Also, in Table 5, the charge during anodization is presented.

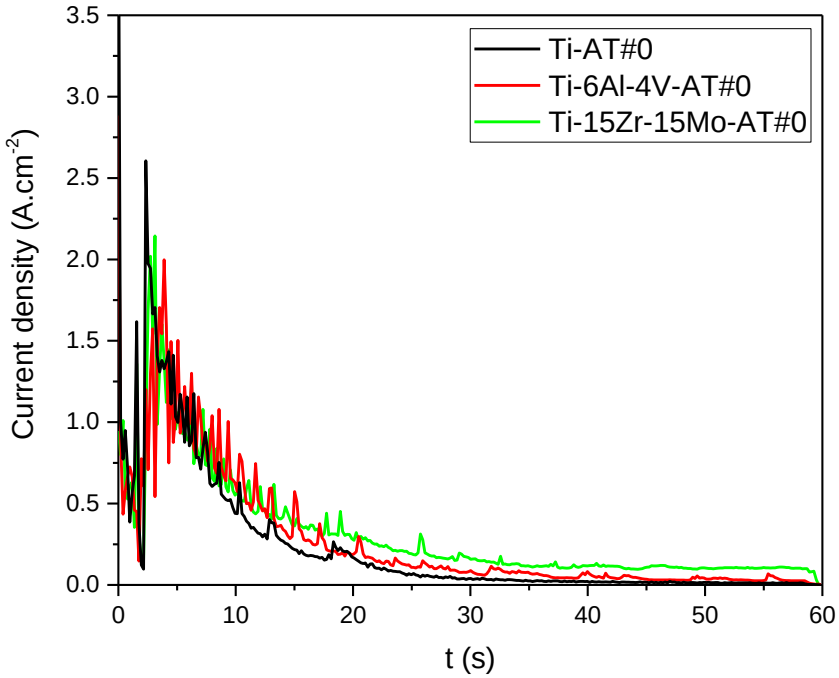

Figure 18 - MAO without particles compared with cp-Ti, Ti-6Al-4V and Ti-15Zr-15Mo.

Table 5 - Charge values for the MAO without particles.

q (C.cm^{-2})		
cp-Ti – AT#0	Ti-6Al-4V – AT#0	Ti-15Zr-15Mo – AT#0
13.5 ± 0.4	15.8 ± 0.2	19.2 ± 0.7

As can be seen by Fig. 18, the 300 V applied by the equipment is reached out instantaneously. After that, there is a sudden drop in the current related to the formation of a compact film. Then, there is the breakdown rupture of the film associated with the increase in the current values, where more energetic pores are formed with a thicker oxide film. The current decreases until the end of the process with occasional peaks due to the formation of pores. This behavior is related with the thickness of the film, where there is an increase in the current density values (occasional peaks) related to the decrease of the oxide film thickness (pore formation). On the other hand, when the new oxide film is formed, as its thickness increases, the current decreases until the end of the anodization time. As it can be seen in Table 5, the charge is higher for the Ti-15Zr-15Mo alloy when compared with the Ti-6Al-4V and cp-Ti. In fact, the higher values in the charge could be associated with the higher current density values of the anodization process for the alloys. Because the current density is related with the thickness of the new oxide film that is formed, it's possible that the titanium alloys samples present lower thickness than the cp-Ti [30].

The EDS chemical analysis results of the MAO samples are summarized in table 6, as well as, their representative SEM images are exhibited in Fig. 19.

Table 6- EDS – Semi-quantitative analysis of the chemical composition from the MAO without particles.

Samples	Ti (at.%)	Al (at.%)	V (at.%)	Zr (at.%)	Mo (at.%)	Ca (at.%)	P (at.%)	O (at.%)	Ca/P
Ti-AT#0	21.69 ± 0.18	-	-	-	-	6.36 ± 0.12	2.04 ± 0.04	69.91 ± 0.15	3.11 ± 0.02
Ti-6Al-4V-AT#0	18,86 ± 0,69	1,72 ± 0,07	0,97 ± 0,03	-	-	6,78 ± 0,09	2,40 ± 0,09	69,26 ± 0,58	2.83 ± 0.08
Ti-15Zr-15Mo-AT#0	17,27 ± 0,26	-	-	2,40 ± 0,05	0,61 ± 0,07	5,99 ± 0,22	1,59 ± 0,04	72,12 ± 0,12	3.75 ± 0.25

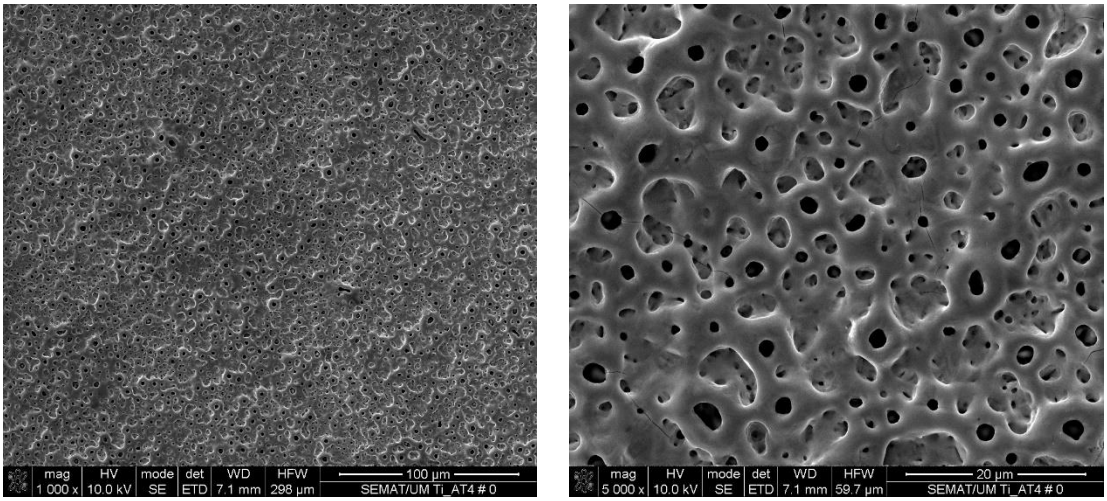

(a)

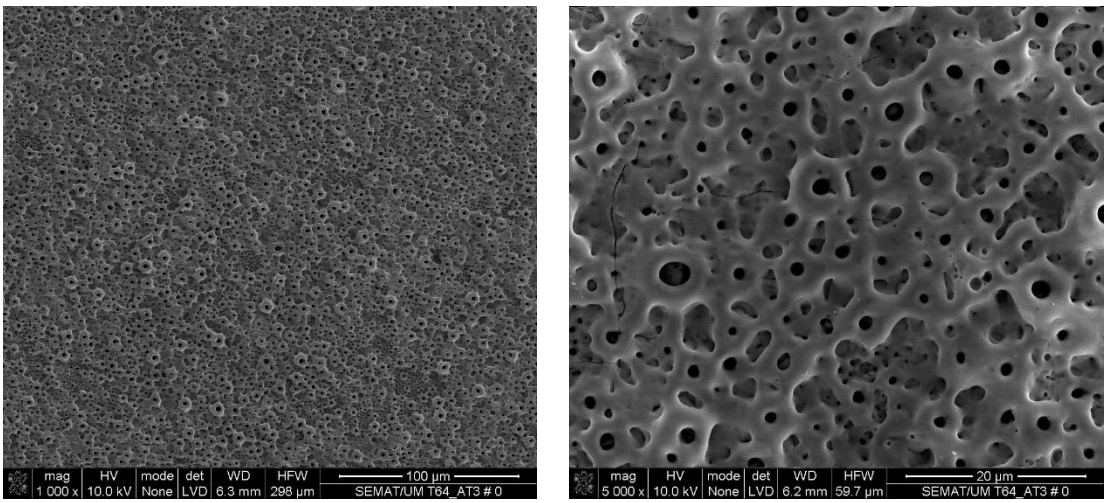

(b)

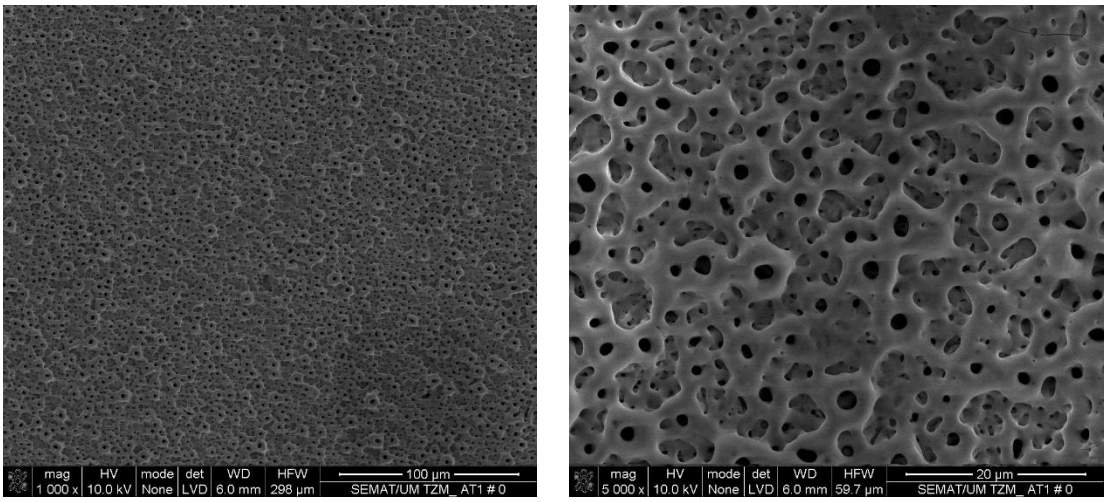

(c)

Figure 19 - SEM images of the anodized samples without particles: a) Ti; b) Ti-6Al-4V; and c) Ti-15Zr-15Mo.

As can be seen by the microstructure presented by the anodization treatment showed in the SEM images (Fig. 19) and between their untreated surface (Fig. 17), the anodization treatment allowed the formation of a porous topography. The surface presented a homogeneous porous morphology with bigger pores ("volcanoes" alike structures) and smaller pores. Also, there is the presence of some cracks along the anodized surface, originated during the growth of the film [30]. As already discussed in the literature [30, 68], this oxide layer is composed of a mixture of crystalline structure (anatase and rutile phases), as well as an amorphous material. Rutile can be found mainly on the top of the bigger porous structures, while anatase is found more at the bottom part of the film. However, between cp-Ti, Ti-6Al-4V and Ti-15Zr-15Mo alloy, there is no visible differences in the microstructure for their anodized surface. For the EDS results of the anodized samples, the chemical analysis of the surfaces showed the presence of the elements Ti and O for all anodic films, the alloying elements Al and V (for the Ti-6Al-4V), and Zr and Mo (for the Ti-15Zr-15Mo). The presence of the bioactive elements Ca and P was also observed in all oxide films. In fact, as can be seen by Table 6, the Ca/P ratio is higher for Ti-15Zr-15Mo (3.75 ± 0.25) and cp-Ti (3.11 ± 0.02), being a little bit lower on the Ti-6Al-4V (2.83 ± 0.08), although it is still higher than the hydroxyapatite (≈ 1.67). However, these are significant results because the Ca/P ratio is important for developing a successful bioactive surface [30, 32, 33, 66]. On the other hand, the results obtained for the Ti-15Zr-15Mo alloy can't be completely verified because of the SEM-EDS limitation in differentiating the excitation energy from Zr (Lα = 2.042 keV) apart from the P (Kα = 2.013 keV). Therefore, further characterizations such as WDS (wavelength-dispersive spectroscopy) or XPS (x-ray photoelectron spectroscopy) are required to verify these results [112].

Also, for further investigation of the oxide film formation, in the Ti-15Zr-15Mo alloy, a FIB cross section was realized in order to understand the growth of the anodic film and its different structures (Fig. 20).

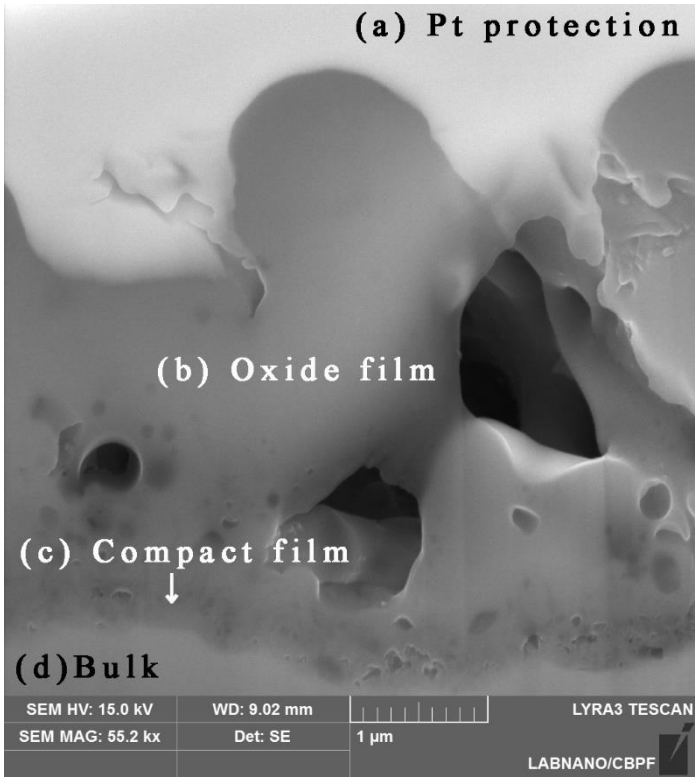

Figure 20 - Cross-section of the anodized Ti-15Zr-15Mo alloy by FIB with: a) Pt protection; b) oxide film; c) compact film; and d) bulk.

As can be seen by Fig. 20, there are three distinguishable layers that were revealed by the FIB cross-section. In the bulk/oxide interface, there is a presence of a thin and compact structure. Then, there is the presence of two porous layers: the inner porous layer, composed of smaller pores; and the outer porous layer, mostly composed of bigger pores. The compact structure at the oxide film and bulk interface was measured with approximately 340 ± 0.32 nm thick.

The size/distribution of pores are presented in Fig. 21 which corroborated the microstructure analysis, where no significant differences of the pores size/distribution for the anodized samples were observed. In general, these samples presented higher frequencies of pores with diameters ranging between 0.5 to 1.0 μm.

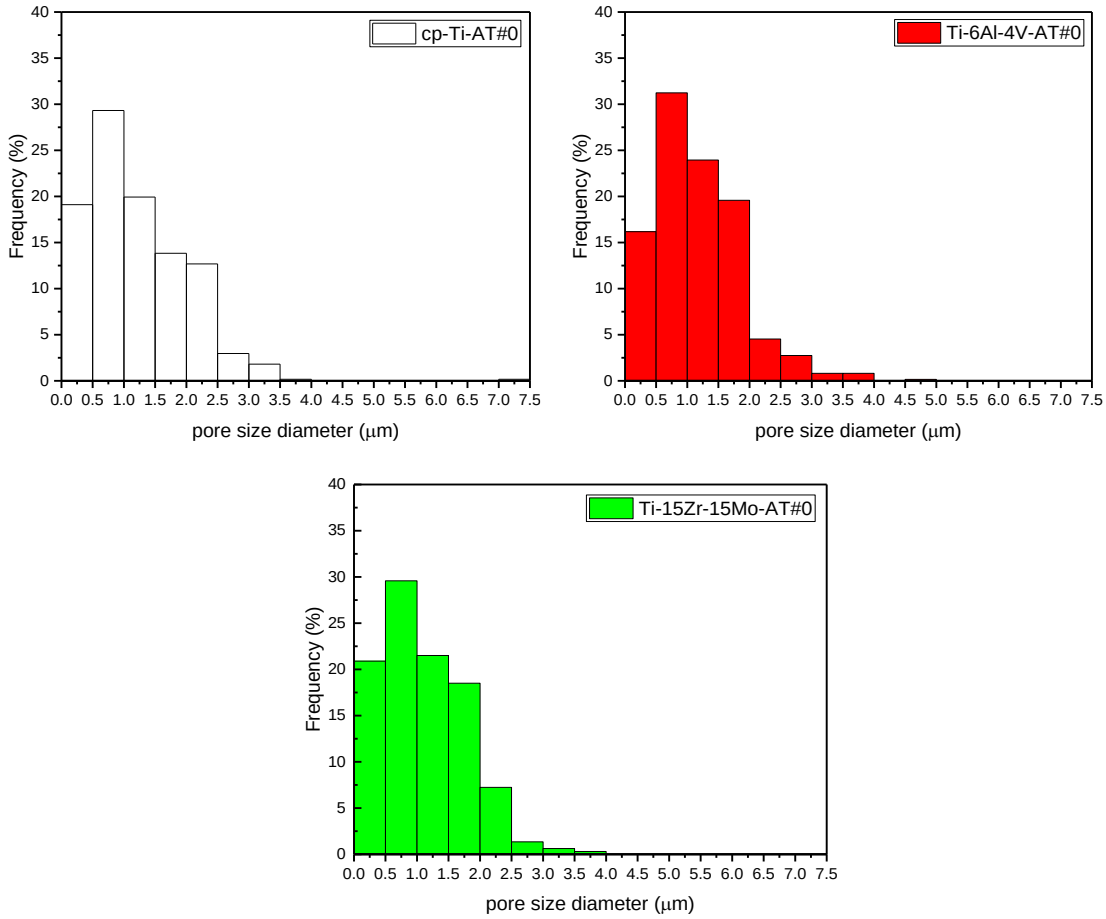

Figure 21 - Pore size/distribution graphs for: cp- Ti; Ti-6Al-4V; and Ti-15Zr-15Mo.

The XRD spectra obtained for the anodized samples are presented in Fig. 22. Also, Table 7 exhibits the phase percentages obtained by the XRD data results with equation (6).

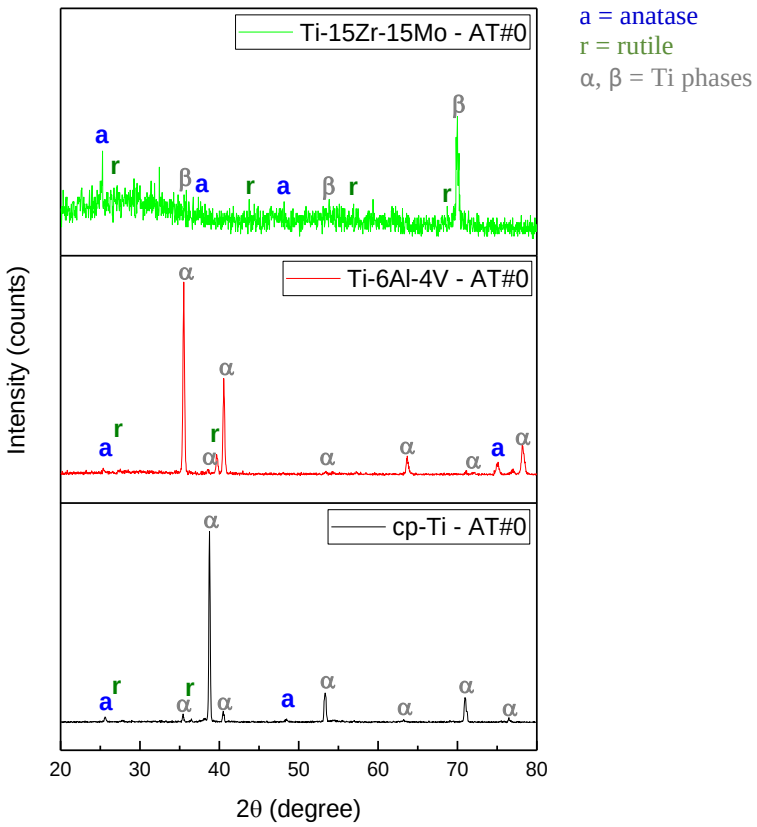

Figure 22 - XRD of MAO without particles for: cp-Ti; Ti-6Al-4V; and Ti-15Zr-15Mo.

Table 7 - Anatase and rutile phase percentage for the MAO without particles.

Phase (%)		
Samples	**Anatase**	**Rutile**
cp-Ti – AT#0	72	28
Ti-6Al-4V– AT#0	49	51
Ti-15Zr-15Mo– AT#0	45	55

For the diffractograms in Fig. 22, it's possible to observe the presence of peaks from the substrate (α or β titanium phase) for the cp-Ti, Ti-6Al-4V and Ti-15Zr-15Mo alloy. Also, some peaks can be identified for the anatase (a) and rutile (r) crystalline structures. As can be seen

for the phase percentages in Table 7, the amount of rutile phase is higher in the Ti-6Al-4V and Ti-15Zr-15Mo alloy, when compared with cp-Ti.

The results obtained by XRD and the anodization curves were summarized in a graph exhibiting the comparison between rutile phase percentage and charge values for the studied samples (Fig.23).

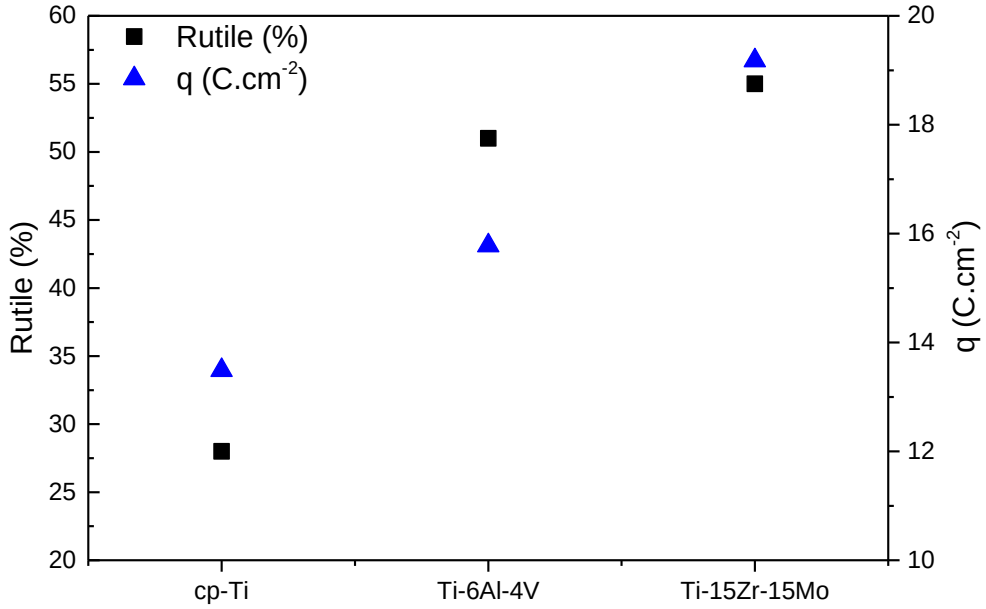

Figure 23 - Comparison between rutile percentage, Ca/P ratio and charge values for the cp-Ti, Ti-6Al-4V and Ti-15Zr-15Mo alloys.

As can be seen by Fig. 23, there is a higher rutile phase presence for the Ti-6Al-4V and Ti-15Zr-15Mo alloys when compared with the cp-Ti. Also, there are higher charge values of the anodization curves for these alloys in comparison with the cp-Ti. As discussed in the works of Wang et al. [113] and Shin et al. [114], higher current density values lead to higher rutile amount in the oxide film. These results could be related to the rutile's formation occurring preferentially in the top zones of the pores, where there are higher temperatures possibly due to these higher energetic discharges [30]. The oxide melts locally and while in contact to a much lower temperature of the electrolyte, the re-solidification is almost instantaneously, where there is an oxide formation related to the decrease in the cooling rate from the surface to the bulk,

leading to a composite with gradient structure [30, 32, 68, 115, 116]. On the other hand , it's known that due to an increase in the conductivity of the electrolyte, there is a higher rutile to anatase ratio, as the current density remains higher for longer processing times [62]. However, the electrolyte used for the MAO of the cp-Ti, Ti-6Al-4V and Ti-15Zr-15Mo were with the same aimed composition.

4.3. Micro-arc Oxidation with incorporation of particles

In this section, the incorporation of HAp and ZnO particles into the oxide film during the anodization process is discussed. The particles were added to the electrolyte with concentrations of 2 and 5 g/l, where an ultrasonic was used for dispersion right before the anodic treatments. The anodization's were also performed in triplicates to ensure its reproducibility.

In Fig. 24 it's presented the anodization curves for the anodized samples with the addition of HAp and ZnO particles. Also, a table is presented detailing the labels for these samples (Table 8).

Table 8 – Labels of the anodized samples with the incorporation of particles.

Sample	HAp - 2 g/l	HAp - 5 g/l	ZnO - 2 g/l	ZnO - 5 g/l
cp-Ti	Ti-AT#2HAp	Ti-AT#5HAp	Ti-AT#2Zn	Ti-AT#5Zn
Ti-6Al-4V	Ti-6Al-4VAT#2HAp	Ti-6Al-4V AT#5HAp	Ti-6Al-4V AT#2Zn	Ti-6Al-4V AT#5Zn
Ti-15Zr-15Mo	Ti-15Zr-15Mo AT#2HAp	Ti-15Zr-15Mo AT#5HAp	Ti-15Zr-15Mo AT#2Zn	Ti-15Zr-15Mo AT#5Zn

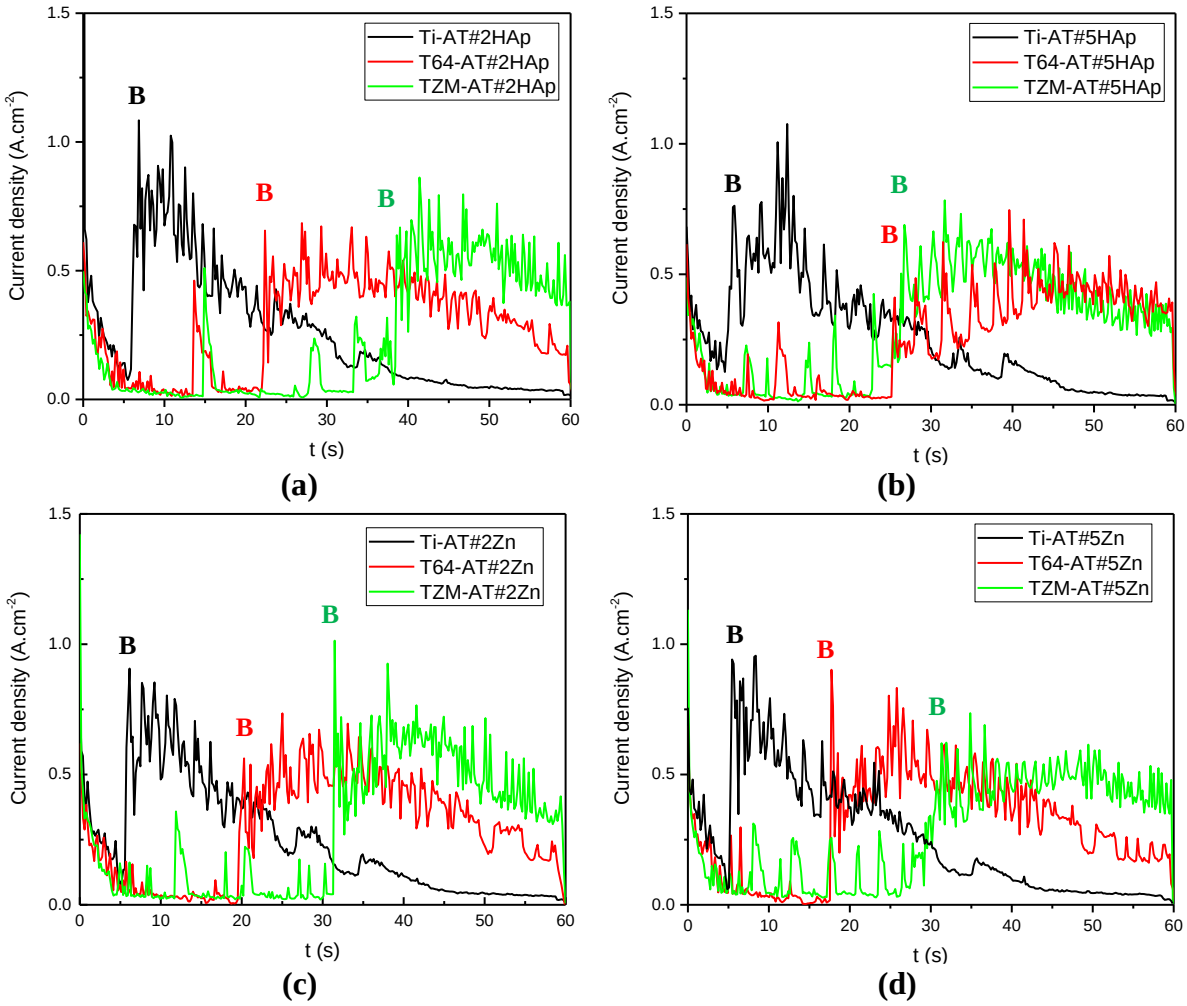

Figure 24 – Comparison between anodization curves for Ti, Ti-6Al-4V and Ti-15Zr-15Mo with: a) 2 g/l of HAp; b) 5 g/l of HAp; c) 2 g/l of ZnO; and d) 5 g/l of ZnO.

These anodization curves (Fig. 24) exhibit a different behavior when compared with the anodization without particles (Fig. 18). As can be seen by Fig. 24, there is a decrease in the current for the early stages of the anodization, but with the 300 V applied by the 2.6 A current equipment's limits still reaching instantaneously right at the initial process. For the cp-Ti, the anodization curves for the conditions with particles are similar to the condition without particles, but with lower current density. However, there is distinguishable difference between the cp-Ti anodization curves with particles when compared with the alloys (Ti-6Al-4V and Ti-15Zr-15Mo). It's possible to observe that for the alloys, after the decrease of the current from the initial stage, the current density remains with lower values for a longer period of time, with occasional increases followed by sudden drops in the current density values. Hence, there is a

bigger delay on the breakdown rupture (B) of the film that is higher from the cp-Ti to the Ti-6Al-4V and Ti-15Zr-15Mo alloys. Because of that delay, the current increases with the breakdown rupture and remains considerably high until the end of the process. In Table 9, we have the charge related to anodization curves.

Table 9 - q values for the MAO with particles in comparison with the anodization without particles.

	q ($C.cm^{-2}$)				
	AT#0	AT#2HAp	AT#5HAp	AT#2Zn	AT#5Zn
Ti-cp	13.49 ± 0.35	15.89 ± 0.52	15.17 ± 0.36	15.77 ± 1.03	15.62 ± 1.02
Ti-6Al-4V	15.78 ± 0.21	15.87 ± 0.88	16.09 ± 1.22	17.84 ± 0.64	17.97 ± 0.42
Ti-15Zr-15Mo	19.18 ± 0.69	18.23 ± 1.74	18.57 ± 1.79	17.01 ± 0.37	18.21 ± 1.93

As can be seen by Table 9, the charge values of the anodization curves with the addition of particles presented no significant differences for the Ti-6Al-4V and Ti-15Zr-15Mo alloys. However, for the cp-Ti, there was a small increase for the charge value between the anodization without particles (Ti-AT#0) and with the presence of particles (Ti-AT#2HAp, Ti-AT#5HAp, Ti-AT#2Zn and Ti-AT#5Zn).

In Fig. 25 it's presented the SEM images for the cp-Ti, Ti-6Al-4V and Ti-15Zr-15Mo MAO samples with the addition of particles. Also, in tables 10-12, the EDS analysis obtained are summarized with their chemical composition. As it can be seen, the 2 g/l of ZnO condition, no incorporation of ZnO was observed. Reasons for this behavior should be investigated in future work. Therefore, further characterization of the samples was performed only for the other conditions (2 g/l of HAp, 5 g/l of HAp and 5 g/l of ZnO), where incorporation of particles was observed.

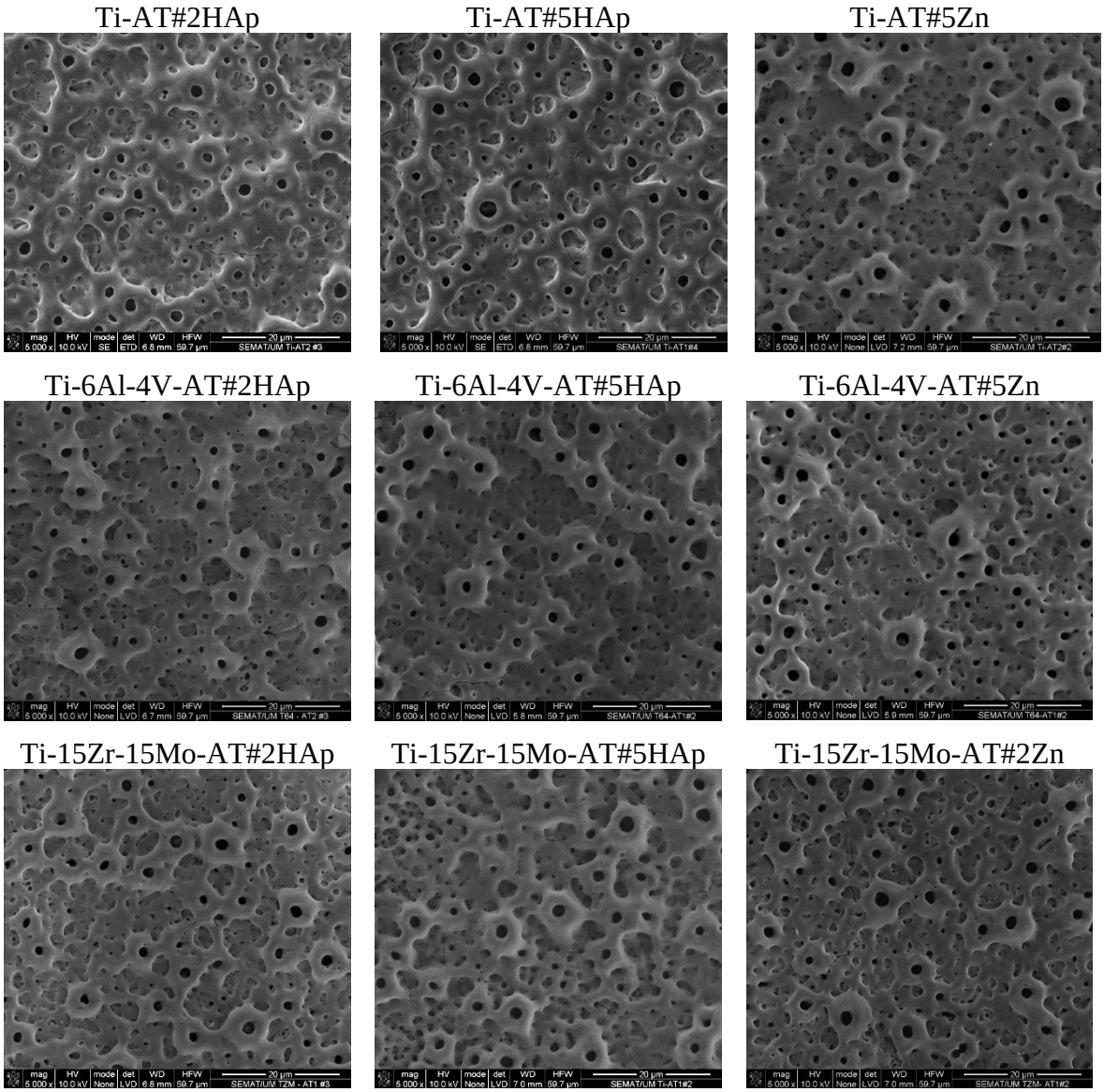

Figure 25 -SEM images for the cp-Ti, Ti-6Al-4V and Ti-15Zr-15Mo alloy anodized samples with the addition of particles.

Table 10 - EDS – Semi-quantitative analysis of the chemical composition from the MAO with particles for Ti.

Ti-cp	Ti (at.%)	Ca (at.%)	P (at.%)	O (at.%)	Zn (at.%)	Ca/P
AT#2HAp	21.62 ± 0.30	6.60 ± 0.21	2.09 ± 0.07	69.69 ± 0.11	-	3.16 ± 0.12
AT#5HAp	21.28 ± 0.16	6.74 ± 0.10	2.13 ± 0.02	69.85 ± 0.14	-	3.17 ± 0.07
AT#2ZnO	21.52 ± 0.36	6.25 ± 0.24	1.95 ± 0.05	70.19 ± 0.16	-	3.21 ± 0.17
AT#5ZnO	21.44 ± 0.16	6.12 ± 0.06	1.95 ± 0.10	70.29 ± 0.11	0.19 ± 0.02	3.14 ± 0.16

Table 11 - EDS – Semi-quantitative analysis of the chemical composition from the MAO with particles for Ti-6Al-4V.

Ti-6Al-4V	Ti (at.%)	Al (at.%)	V (at.%)	Ca (at.%)	P (at.%)	O (at.%)	Zn (at.%)	Ca/P
AT#2HAp	19.81 ± 0.30	1.80 ± 0.04	0.93 ± 0.13	6.66 ± 0.33	2.35 ± 0.07	68.45 ± 0.49	-	2.84 ± 0.15
AT#5HAp	18.75 ± 0.26	1.76 ± 0.57	0.97 ± 0.04	6.90 ± 0.36	2.57 ± 0.15	69.04 ± 0.57	-	2.68 ± 0.02
AT#2ZnO	19.39 ± 0.69	1.85 ± 0.07	1.02 ± 0.04	6.37 ± 0.65	2.47 ± 0.24	68.90 ± 0.79	-	2.58 ± 0.08
AT#5ZnO	19.77 ± 0.57	1.83 ± 0.12	1.11 ± 0.16	6.13 ± 0.49	2.29 ± 0.13	68.67 ± 0.20	0.20 ± 0.04	2.67 ± 0.07

Table 12 - EDS – Semi-quantitative analysis of the chemical composition from the MAO with particles for Ti-15Zr-15Mo

Ti-15Zr-15Mo	Ti (at.%)	Zr (at.%)	Mo (at.%)	Ca (at.%)	P (at.%)	O (at.%)	Zn (at.%)	Ca/P
AT#2HAp	17.07 ± 0.20	2.52 ± 0.22	0.69 ± 0.09	6.71 ± 0.14	1.74 ± 0.26	71.25 ± 0.46	-	3.90 ± 0.51
AT#5HAp	17.63 ± 0.08	2.59 ± 0.06	0.70 ± 0.04	7.45 ± 0.07	1.87 ± 0.08	69.76 ± 0.06	-	3.99 ± 0.20
AT#2ZnO	18.12 ± 0.29	2.51 ± 0.07	0.63 ± 0.06	6.52 ± 0.10	1.75 ± 0.14	70.45 ± 0.11	-	3.75 ± 0.25
AT#5ZnO	17.10 ± 0.32	2.38 ± 0.02	0.59 ± 0.04	6.37 ± 0.03	1.77 ± 0.02	71.45 ± 0.30	0.33 ± 0.04	3.60 ± 0.23

As can be seen in Fig. 25, the SEM images obtained by the MAO samples with the addition of particles exhibited similar surface when compared with the anodized samples without particles (Fig. 19). Therefore, it's possible to observe a homogeneous pore morphology with "volcanoes" type structures mixed with the presence of smaller pores, all over the anodized surface. Also, some cracks are still present in the anodized surface for all conditions. Regarding the incorporation of particles, no presence of the HAp or the ZnO was observed on these surfaces. In tables 10-12, the chemical composition for the anodized samples with the addition of particles exhibit the presence of Ti and O for all samples, as well as, the bioactive elements (Ca and P). For the Ti-6Al-4V and Ti-15Zr-15Mo alloys, the presence of their respectively alloying elements is also shown (Al, V, Zr and Mo). Thus, because the HAp particles are composed of Ca and P, their chemical composition analysis couldn't be separated with the

bioactive elements. Therefore, the EDS analysis could not determine the incorporation of particles for the studied samples, besides for the 5 g/l of ZnO condition.

Figures 26-28 show the pore size/distribution graphs for the MAO samples with the addition of particles. As can be seen, these results are in agreement with the SEM images analysis observed for these samples, where no significant differences were noticed regarding their pore morphology and distribution over the surface of cp-Ti, Ti-6Al-4V and Ti-15Zr-15Mo with the addition of particles. The pore size/distribution graphs for all conditions exhibited similar behavior with most presence of pores ranging between 0.5 to 1.0 μm.

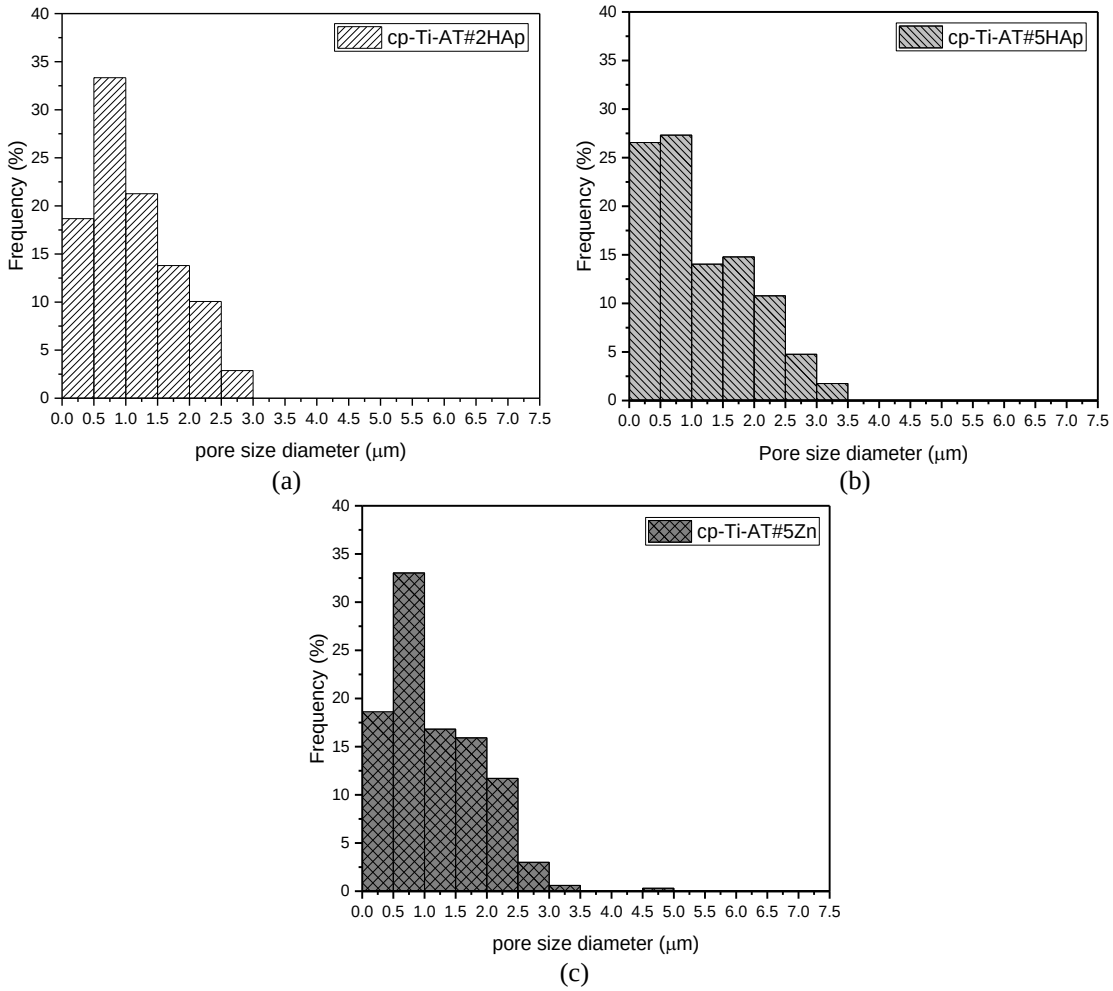

Figure 26 - Pore size/distribution graphs for cp-Ti anodized with: a) 2 g/l of HAp: b) 5 g/l of HAp; and c) 5 g/l of ZnO.

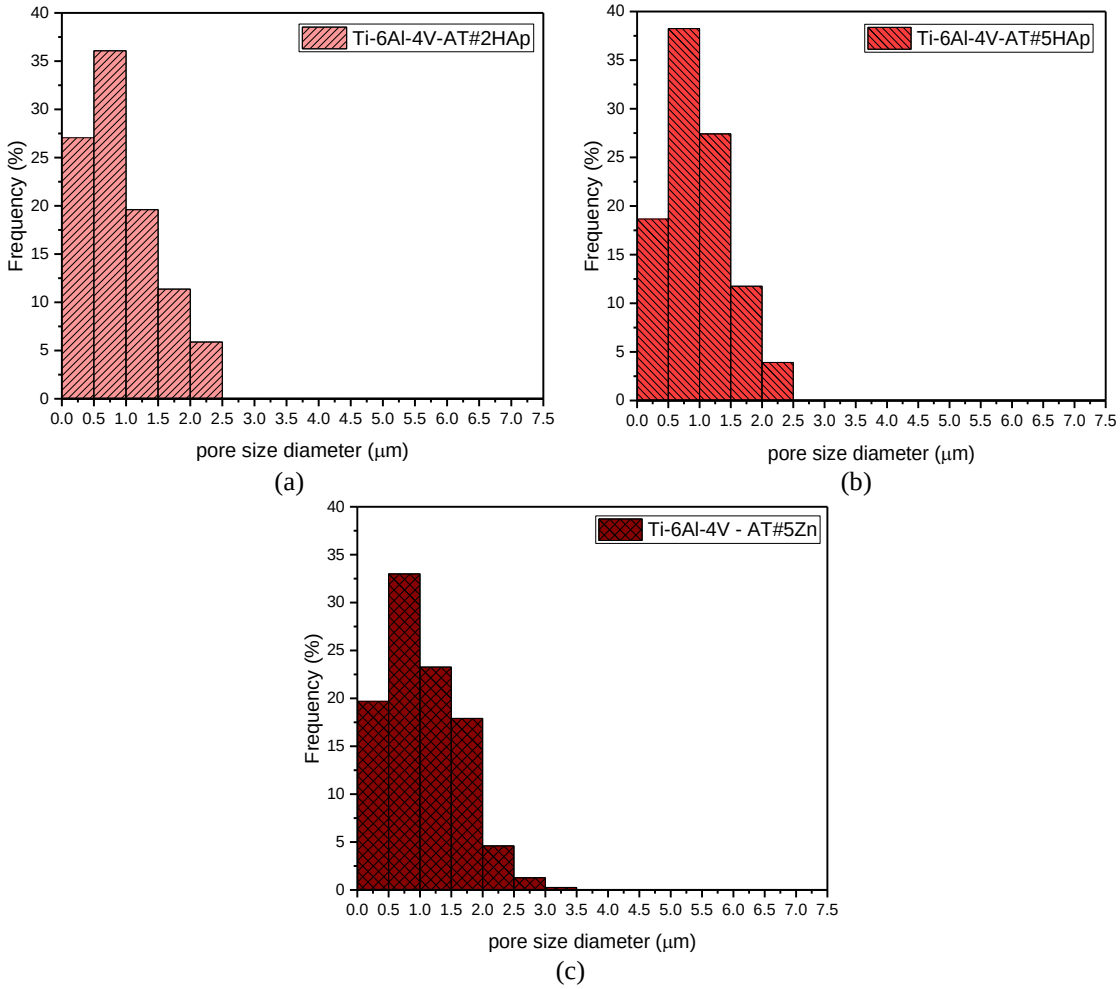

Figure 27 - Pore size/distribution graphs for Ti-6Al-4V anodized with: a) 2 g/l of HAp: b) 5 g/l of HAp; and c) 5 g/l of ZnO.

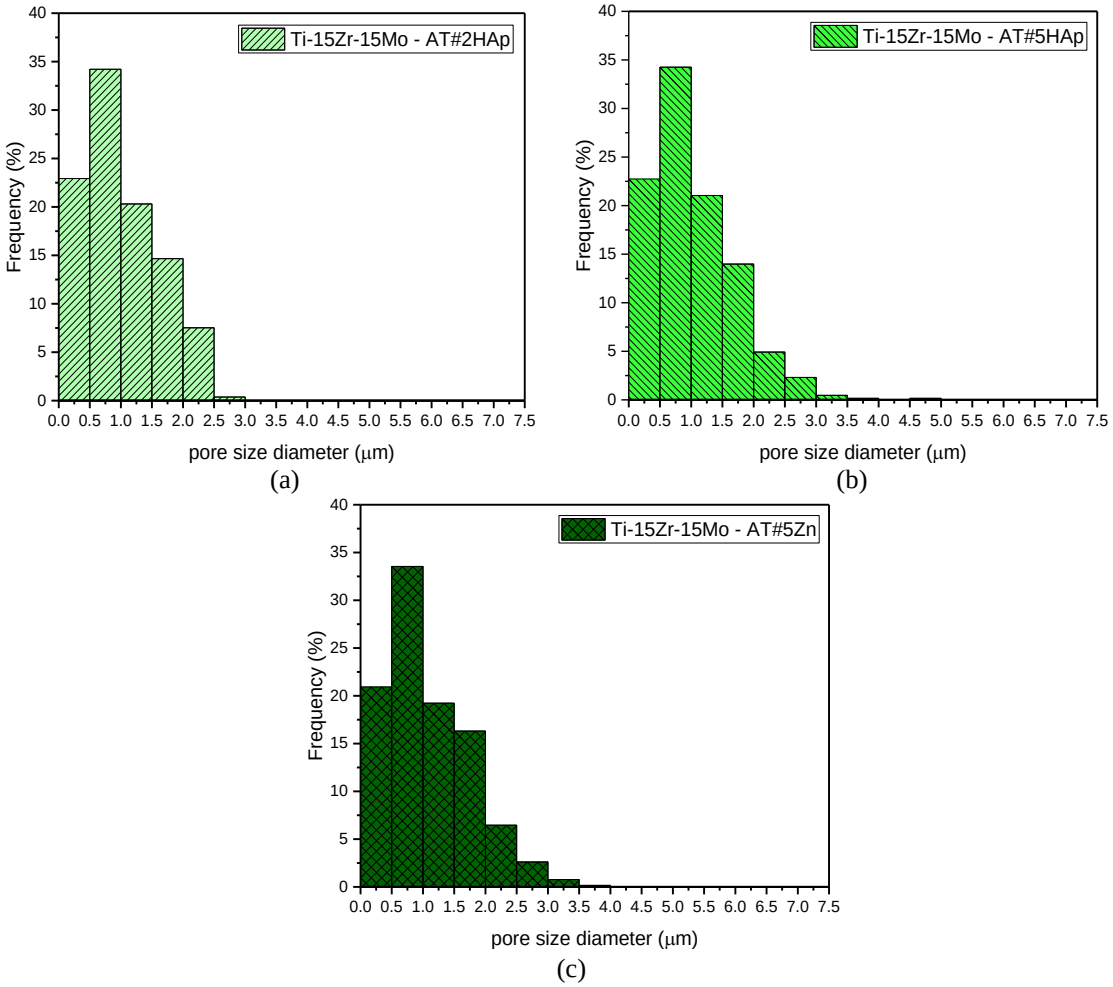

Figure 28 - Pore size/distribution graphs for Ti-15Zr-15Mo anodized with: a) 2 g/l of HAp: b) 5 g/l of HAp; and c) 5 g/l of ZnO.

In Fig. 29 the XRD analysis of the MAO with the addition of particles is presented. As can be seen by these diffractograms, it's possible to identify α or β titanium phase peaks from the substrate samples of cp-Ti, Ti-6Al-4V and Ti-15Zr-15Mo. Also, anatase (a) and rutile (r) peaks were identified for all the studied conditions. In Table 13, it's presented the results regarding the anatase and rutile phase percentages of the MAO samples with the addition of particles.

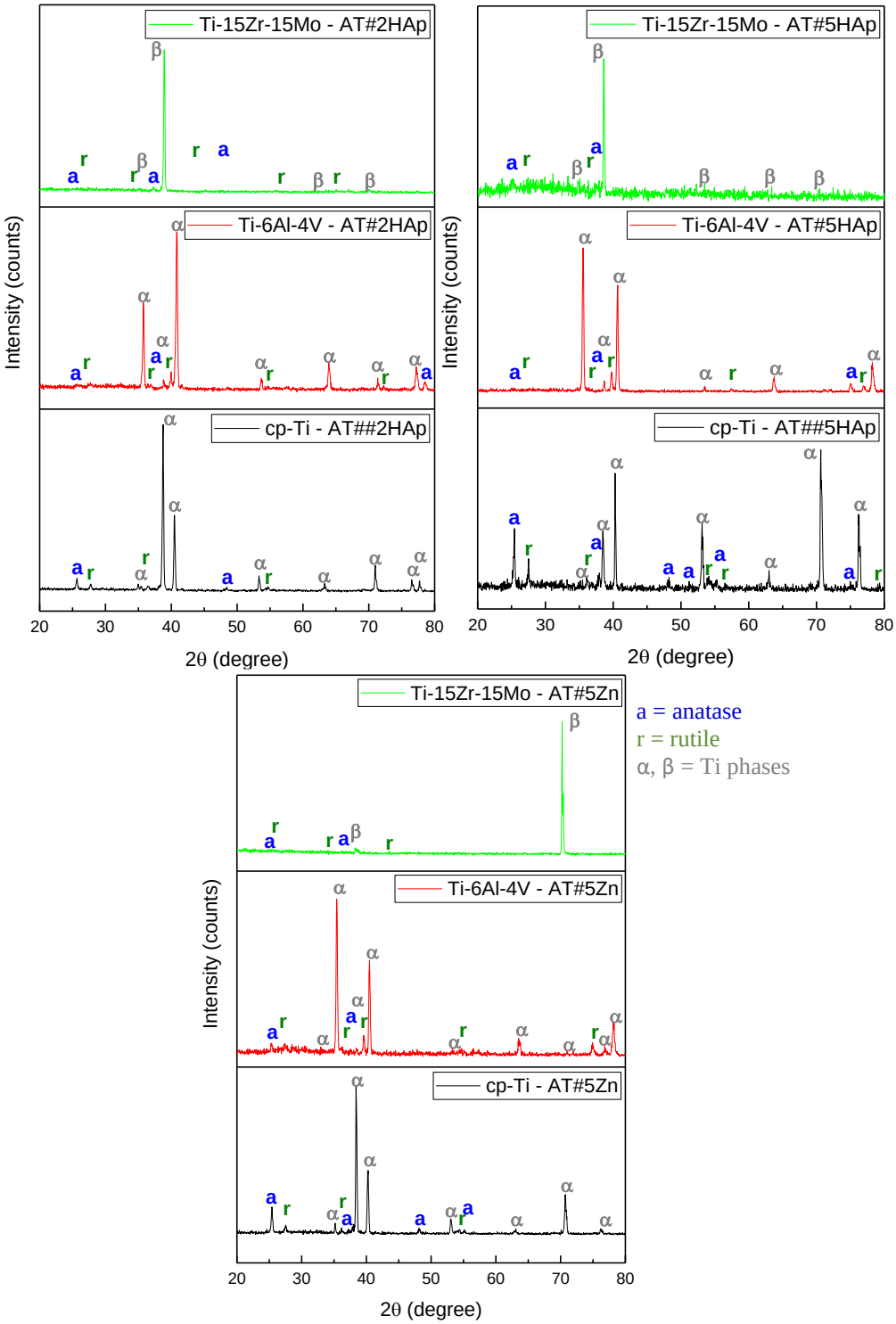

Figure 29 - XRD for the MAO with the addition of particles.

Table 13 – Anatase (A) and rutile (R) phase percentages for the MAO with the addition of particles.

Phase (%)								
	AT#0		AT#2HAp		AT#5HAp		AT#5ZnO	
	A	**R**	**A**	**R**	**A**	**R**	**A**	**R**
Ti	72	28	60	40	61	39	63	37
Ti-6Al-4V	49	51	35	65	32	68	30	70
Ti-15Zr-15Mo	45	55	39	61	40	60	38	62

In Fig. 30, the results obtained by the anodization curves and the XRD analysis are summarized comparing the charge and the rutile phase percentages between the MAO samples (cp-Ti, Ti-6Al-4V and Ti-15Zr-15Mo alloys) with and without the addition of particles.

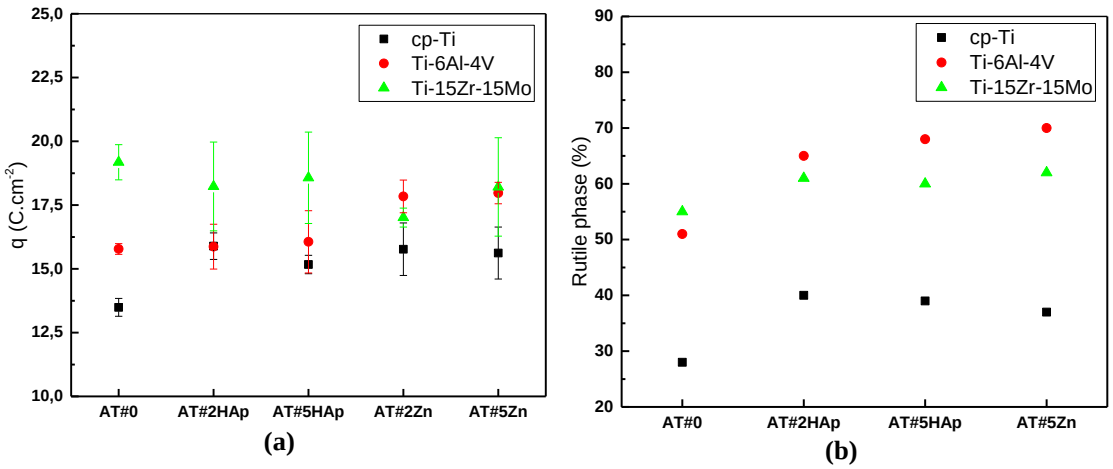

Figure 30 - Charge values and rutile phase percentage of the MAO samples with and without the addition of particles.

As can be seen by Fig. 30, although the anodized samples with the addition of particles showed no significant difference regarding their pore morphology, pore size/distribution, chemical composition, charge and anatase/rutile phase percentages, this comparison shows a tendency for the studied conditions. The cp-Ti presented lower values of charge and rutile phase when compared with the Ti-6Al-4V and Ti-15Zr-15Mo alloys, that could be related to the

higher current density during the anodization process of the alloys for a longer period of time (See Fig. 24). In fact, the Ti-6Al-4V and Ti-15Zr-15Mo alloys presented similar results for both analyses. Because Al and Zr oxides should present higher presence than V and Mo oxides, due to their higher EDS percentages (see Tables 11 and 12), when following the Ellingham diagram (Fig. 31), it's possible to verify the higher stability for the Al and Zr oxides when compared with the Ti oxide. Therefore, these results could be related with a higher stability of the cp-Ti oxides that were formed at the surface, hence lower number of arcs, which produces lower temperatures values and, therefore, lower rutile phase percentages [113, 117]. Also, the ultrasonic dispersion procedure performed for the MAO with the addition of particles, could have influenced this result, since its responsible for an increase in the electrolyte's temperature before the anodization process, when compared with the anodization without particles. The results show that the incorporation of particles appear not to be achieved by these conditions. Therefore, higher concentrations of the reagents should be considered to the MAO aiming the functionalization with HAp and ZnO particles.

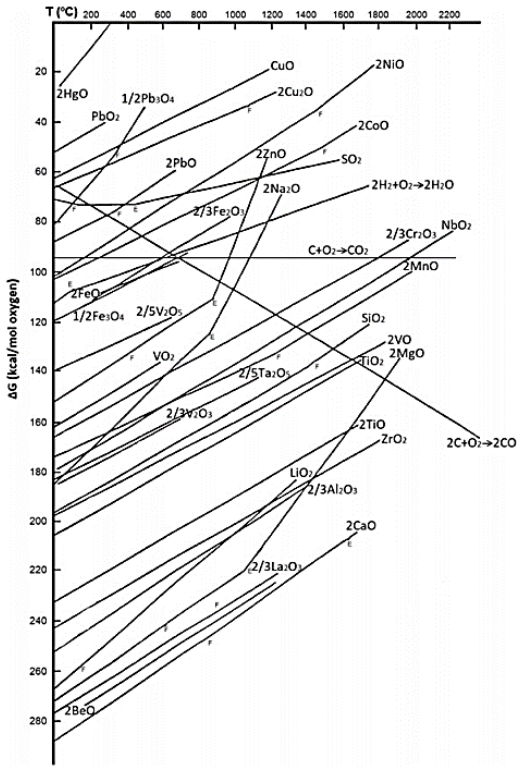

Figure 31 - Ellingham's Diagram ΔG°(T) for the formation of metallic oxides [117].

4.4. Electrochemical and Tribocorrosion behavior

This section will present the corrosion and tribocorrosion analysis comparing the results of cp-Ti, Ti-6Al-4V and Ti-15Zr-15Mo alloy for the as cast and the MAO without particles. In Fig. 32, representative potentiodynamic polarization curves are presented.

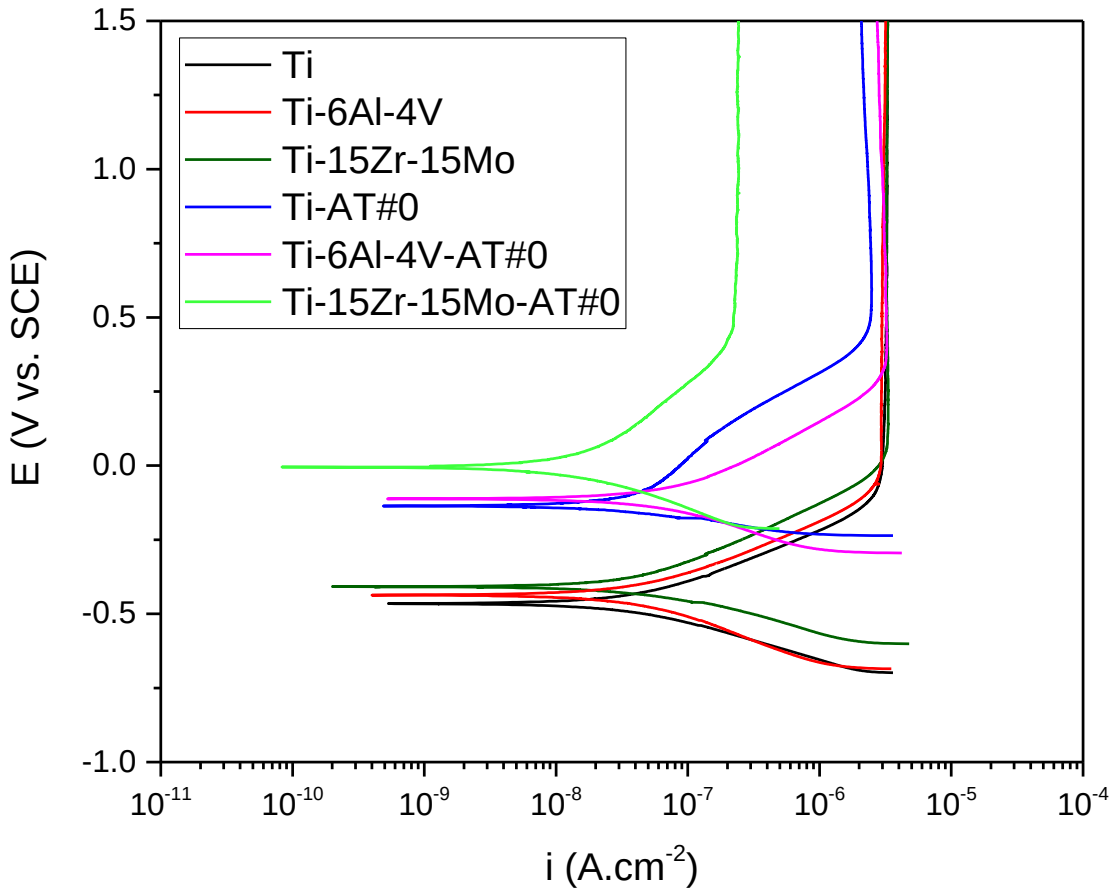

Figure 32 - Potentiodynamic polarization curves for the cp-Ti, Ti-6Al-4V and Ti-15Zr-15Mo: untreated samples; and MAO conditions.

These results were obtained for the untreated samples and the MAO without particles, where all samples presented good reproducibility with a well-defined passivation plateau. Corrosion potential was obtained from the intersection of the linear anodic and cathodic branches of the polarization curves while the passivation current was estimated from the

passivation plateau. As can be seen, the anodic treatments presented higher potential values when compared with the untreated samples. However, the passivation current (i_{pass}) showed no significant differences for the Ti and Ti-6Al-4V samples, where the anodized Ti-15Zr-15Mo alloy presented significant lower current densities in the passive domain. In Table 14, the corrosion results are presented.

Table 14 - Potentiodynamic polarization results for the untreated samples and the MAO without particles.

	E_{corr} (mV)	i_{pass} ($\mu A.cm^{-2}$)
Ti-cp	-474 ± 24	3.26 ± 0.34
Ti-AT#0	-119 ± 22	2.26 ± 0.06
Ti-6Al-4V	-409 ± 22	3.35 ± 0.41
Ti-6Al-4V-AT#0	-101 ± 38	3.07 ± 0.14
Ti-15Zr-15Mo	-388 ± 17	3.29 ± 0.06
Ti-15Zr-15Mo – AT#0	11 ± 22	0.30 ± 0.06

Figure 33 and Figure 34 shows the Nyquist and Bode diagrams derived from the electrochemical impedance results for the cp-Ti, Ti-6Al-4V and Ti-15Zr-15Mo untreated and anodized conditions. Also, the equivalent electrical circuits used for the fitting of the experimental data in the EIS spectra are presented in Fig. 35 and 36. For the untreated samples, the equivalent circuit presents the electrolyte resistance (R_s), the native barrier oxide film resistance ($R_{bf(N)}$) and the constant phase element ($Q_{bf(N)}$), which is related to the capacitance of the native barrier oxide film. In fact, the constant phase element ($Q_{bf(N)}$) values can be converted to the capacitance of the native barrier oxide film ($C_{bf(N)}$) by using eq. (7) which is derived from Brug's equation [103, 118]. On the other hand, for the anodic treated samples, the equivalent circuit used followed the proposed circuits of Alves et al. [103], whereas a triplex structure were observed for these samples. This triplex structure was composed of: a thin and compact

oxide film at the bulk/oxide interface, named as anodic treatment barrier film (bf_{AT}); and two porous layers, the inner porous layer (ip), due to the small porous that reach the barrier film, and the outer porous layer (op), due to the larger pores at the surface that don't reach the barrier film. In this aspect, the equivalent circuit for the anodic treatments presents: the electrolyte resistance (R_S); the anodic treatment barrier oxide film resistance ($R_{bf(AT)}$) and its constant phase element ($Q_{bf(AT)}$); the resistances associated with the solution's resistance inside the inner and outer pores ($R_{s\text{-}ip}$ and $R_{s\text{-}op}$, respectively); and the two constant phase elements that correspond to the intact porous wall and to the porous wall of the outer pores (Q_{wall} and $Q_{1/2wall}$, respectively). In addition, the constant phase elements were also converted into capacitance values, where it was obtained the capacitance of the anodic treatment barrier oxide film ($C_{bf(AT)}$) by using eq. (8), the capacitance of the intact porous wall (C_{wall}) by using eq. (9), and the capacitance of the outer porous wall ($C_{1/2wall}$) by using eq. (10) [103, 119].

$$C_{bf(N)} = [Q_{bf(N)} {R_s}^{(1-n)}]^{\frac{1}{n}} \tag{7}$$

$$C_{bf(AT)} = \left[Q_{bf(AT)\left(\frac{1}{R_s+R_{s-ip}}+\frac{1}{R_{bf(AT)}}\right)^{(n-1)}} \right]^{\frac{1}{n}} \tag{8}$$

$$C_{wall} = [Q_{wall} {R_s}^{(1-n)}]^{\frac{1}{n}} \tag{9}$$

$$C_{1/2wall} = [Q_{1/2wall}(R_s + R_{s-op})^{(1-n)}]^{\frac{1}{n}} \tag{10}$$

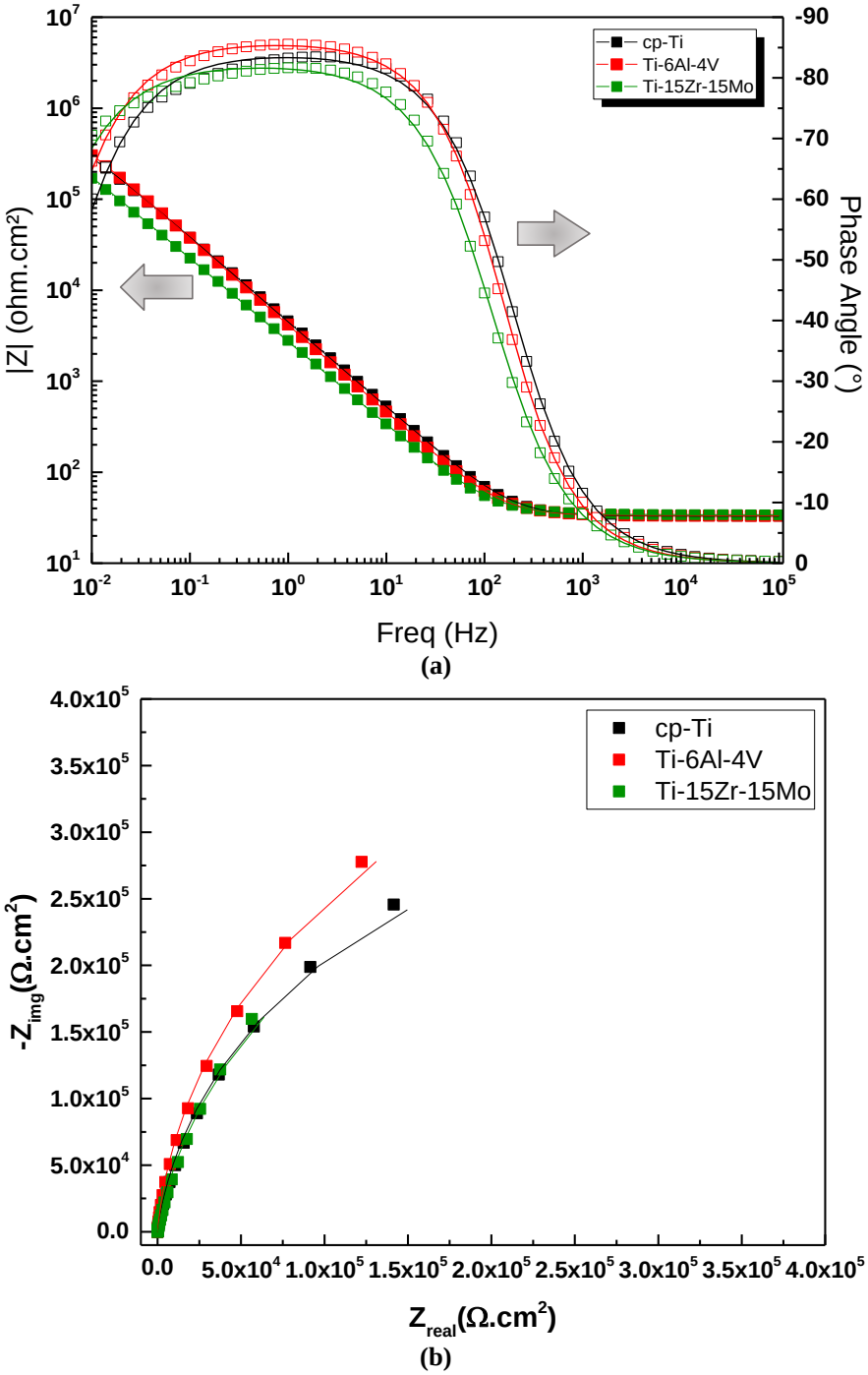

Figure 33 - EIS results for the untreated samples: a) Bode; and b) Nyquist.

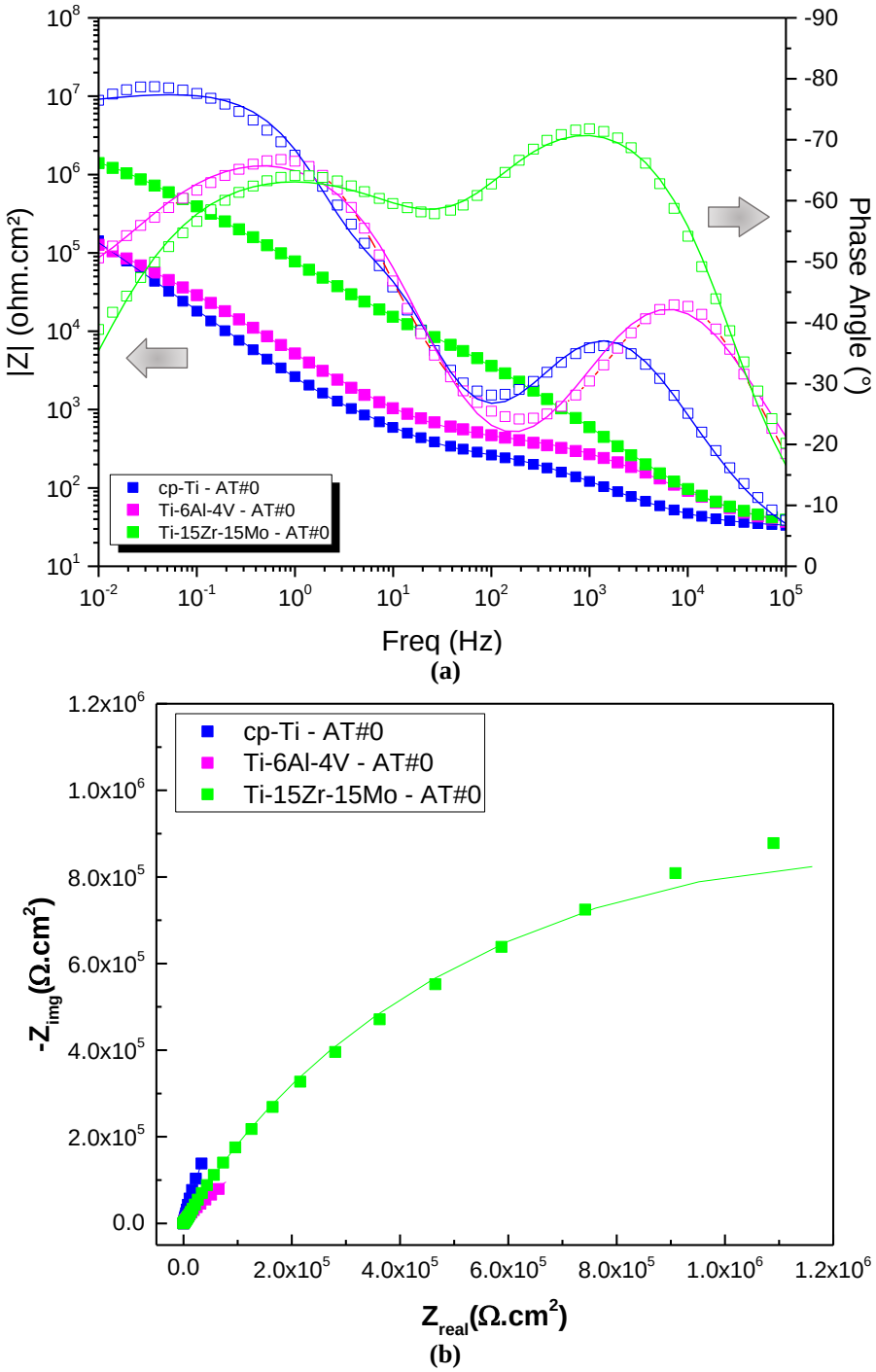

Figure 34 - EIS results for the MAO condition without particles: a) Bode; and b) Nyquist

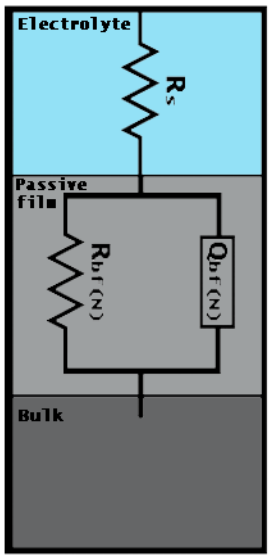

Figure 35 - Circuit used for the EIS fitting of the untreated samples.

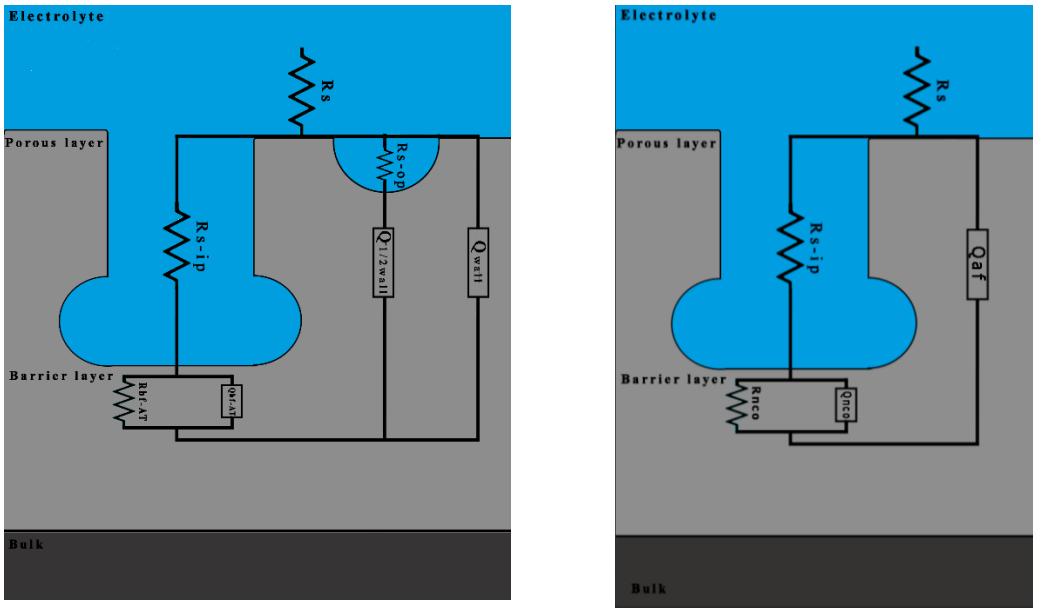

a) b)

Figure 36 - Circuit used for the EIS fitting of the anodized samples: a) cp-Ti and Ti-6Al-4V; and b) Ti-15Zr-15Mo.

As can be seen, the Bode diagrams for the untreated samples (Fig. 33.a), the phase angle shifted to values near 90° for lower frequencies than 10^2 Hz. This could be related to the capacitive behavior of the compact oxide film. In Table 15, the equivalent circuit parameters estimated from the spectra are presented. From the Table 15, the Ti-6Al-4V presented the higher native barrier oxide film resistance (R_{ox}), while cp-Ti and Ti-15Zr-15Mo alloy showed similar values. Regarding capacitance (C_{ox}) it is of the same magnitude for all materials. This indicates a higher protection of the passive oxide film for the Ti-6Al-4V alloy [103]. The quality of the results obtained by the equivalent circuit parameters was evaluated by their goodness of fitting, in which, all samples presented a goodness of fitting (χ^2) bellow 10^{-4}, as can be seen by Tables 15 and 16.

For the EIS spectra data obtained for the MAO samples, a different behavior is observed where it seems to exist, at least, two times constants in the Bode diagrams (Fig. 34.a). The time constant related to the higher frequencies presented higher values for the Ti-15Zr-15Mo than cp-Ti and Ti-6Al-4V. Also, for the lower frequencies, there is a decrease in the phase angle from the cp-Ti to the Ti-6Al-4V and Ti-15Zr-15Mo alloys [103].

Table 15 - EIS results for the untreated samples.

	cp-Ti	**Ti-6Al-4V**	**Ti-15Zr-15Mo**
R_{ox} ($M\Omega cm^{-2}$)	0.63 ± 0.06	1.14 ± 0.68	0.74 ± 0.05
C_{ox} (μFcm^{-2})	30 ± 5	29 ± 1	36 ± 3
χ^2	< 4.59×10^{-4}	< 1.52×10^{-4}	3.80×10^{-4}

Table 16 - EIS results for the MAO without particles.

	Ti-AT#0	**Ti-6Al-4V-AT#0**	**Ti-15Zr-15Mo-AT#0**	
$C_{1/2wall}$ (μFcm^{-2})	33.11 ± 9.24	12.28 ± 0.74	-	-
C_{wall} (μFcm^{-2})	0.72 ± 0.04	0.15 ± 0.02	C_{af} (μFcm^{-2})	0.02 ± 0.01
C_{bf} (μFcm^{-2})	14.99 ± 2.93	4.76 ± 1.22	C_{nco} (μFcm^{-2})	0.45 ± 0.03
χ^2	$< 5.96 \times 10^{-4}$	$< 2.91 \times 10^{-4}$	χ^2	$< 6.98 \times 10^{-4}$

In Fig. 37 representative curves of the tribocorrosion results consisting in coefficient of friction (COF) and open circuit potential values (OCP) before, during and after sliding are presented.

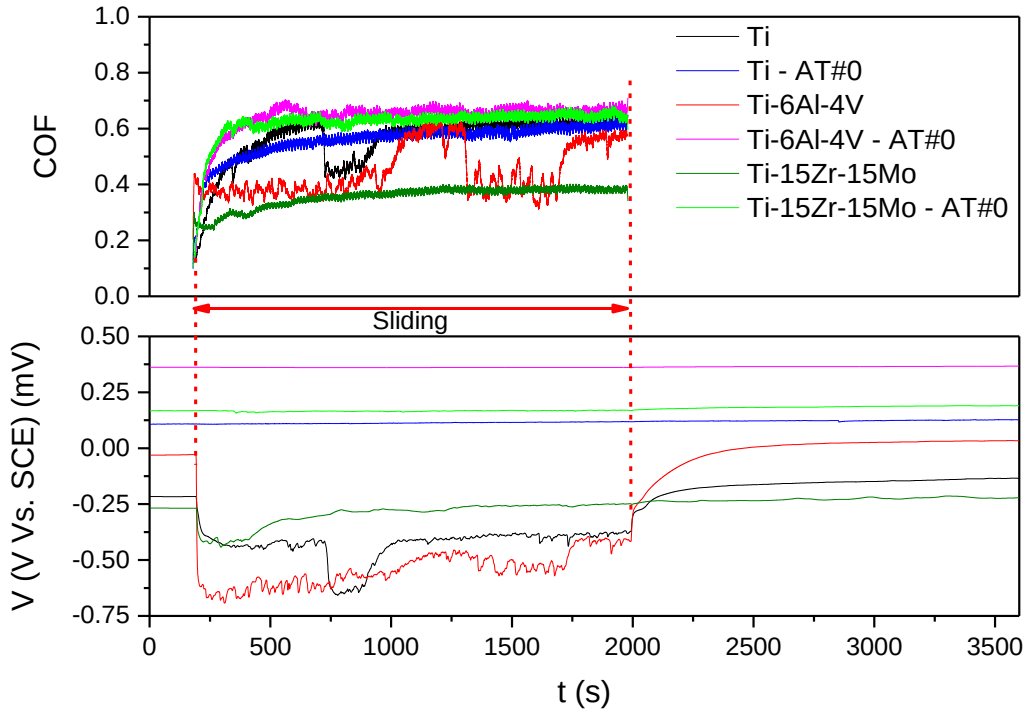

Figure 37 - Tribocorrosion results for the as cast and MAO without particles for Ti, Ti-6Al-4V and Ti-15Zr-15Mo.

As it can be seen by Fig. 37, before the start of sliding, the MAO presented significantly higher OCP values than the untreated conditions, indicating a lower tendency to corrosion. This can be related to the presence of the protective anodic film on the surface of the MAO samples [11]. When sliding begins, there is a sudden drop in the OCP values for the untreated samples, associated with the removal of the passive film at the surface and consequently the exposure of the bulk material to the solution's corrosive effects. After sliding ended, OCP evolute to the values observed before sliding, possibly due to the repassivation process occurring in the wear tracks. On the other hand, considering the MAO samples, no significant variation of the OCP was observed during sliding, indicating a better tribocorrosion behavior when compared with the untreated conditions [11, 66, 120, 121]. Regarding the COF values, the anodized samples showed similar tendency with stable values between Ti-6Al-4V-AT#0 ($\mu \approx 0.65$), Ti-15Zr-15Mo-AT#0 ($\mu \approx 0.60$) and Ti-AT#0 ($\mu \approx 0.50$). However, for the untreated samples, the COF values presented a different behavior, with the Ti-15Zr-15Mo alloy exhibiting stable COF values around 0.30, whilst the cp-Ti and Ti-6Al-4V alloy showed an unstable behavior with COF values increasing and decreasing during the sliding time. This could be related to the formation of oxide patches and wear debris along the tribocorrosion test.

Figures 38 and 39 exhibits the micrographs of the wear tracks illustrating the wear behavior between the untreated and the MAO conditions. In Fig. 38, the representative SEM micrographs shows the backscattered electrons detector (BSE) along with the secondary electrons detector (SE). The BSE detector allows the analysis of differences in the atomic number at the surface materials. On the other hand, Fig. 39 presented the worn surface areas of the studied samples with higher magnification SEM images.

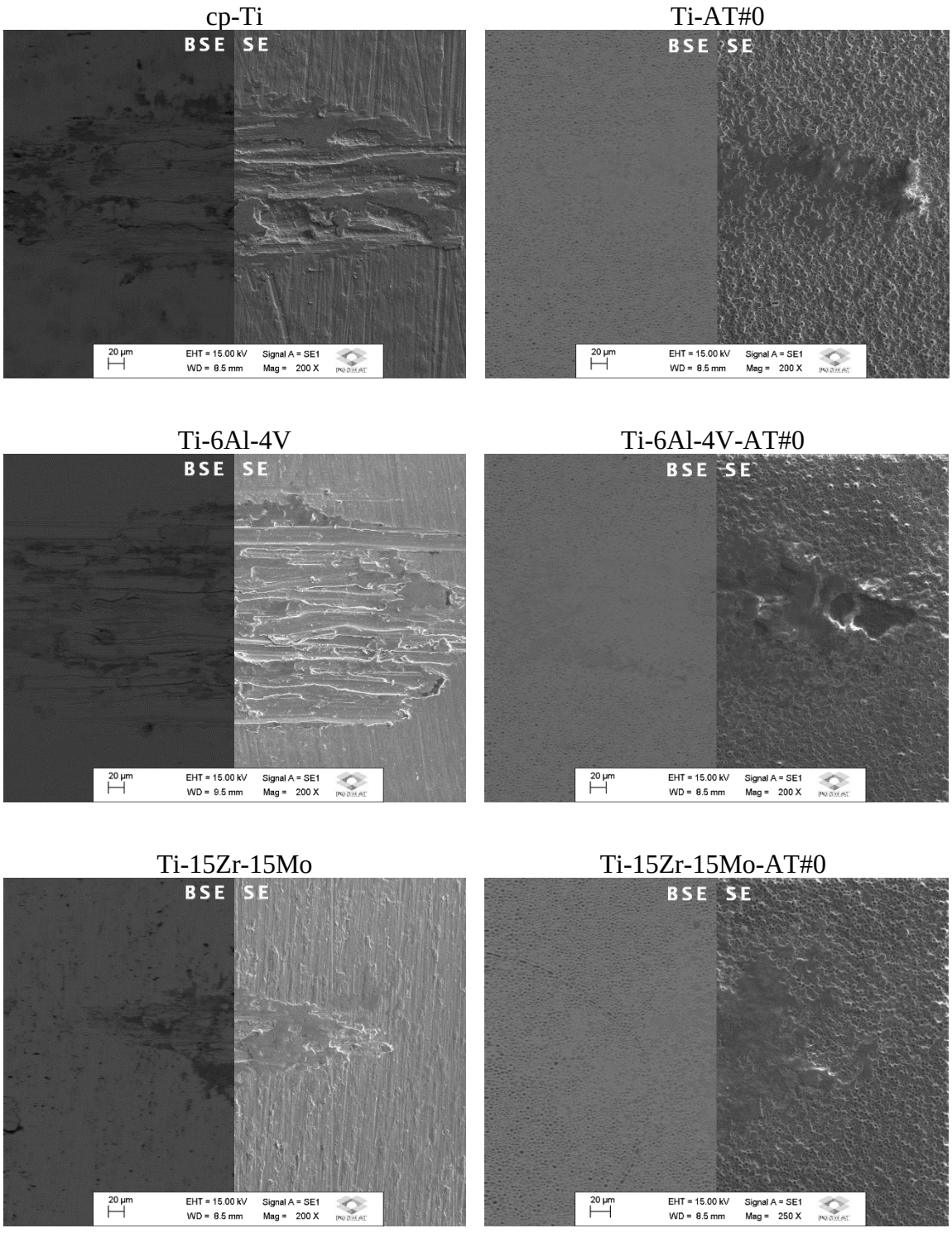

Figure 38 - SEM images of the wear tracks for the: cp-Ti; anodized Ti-AT#0; Ti-6Al-4V; anodized Ti-6Al-4V-AT#0; Ti-15Zr-15Mo; and anodized Ti-15Zr-15Mo-AT#0.

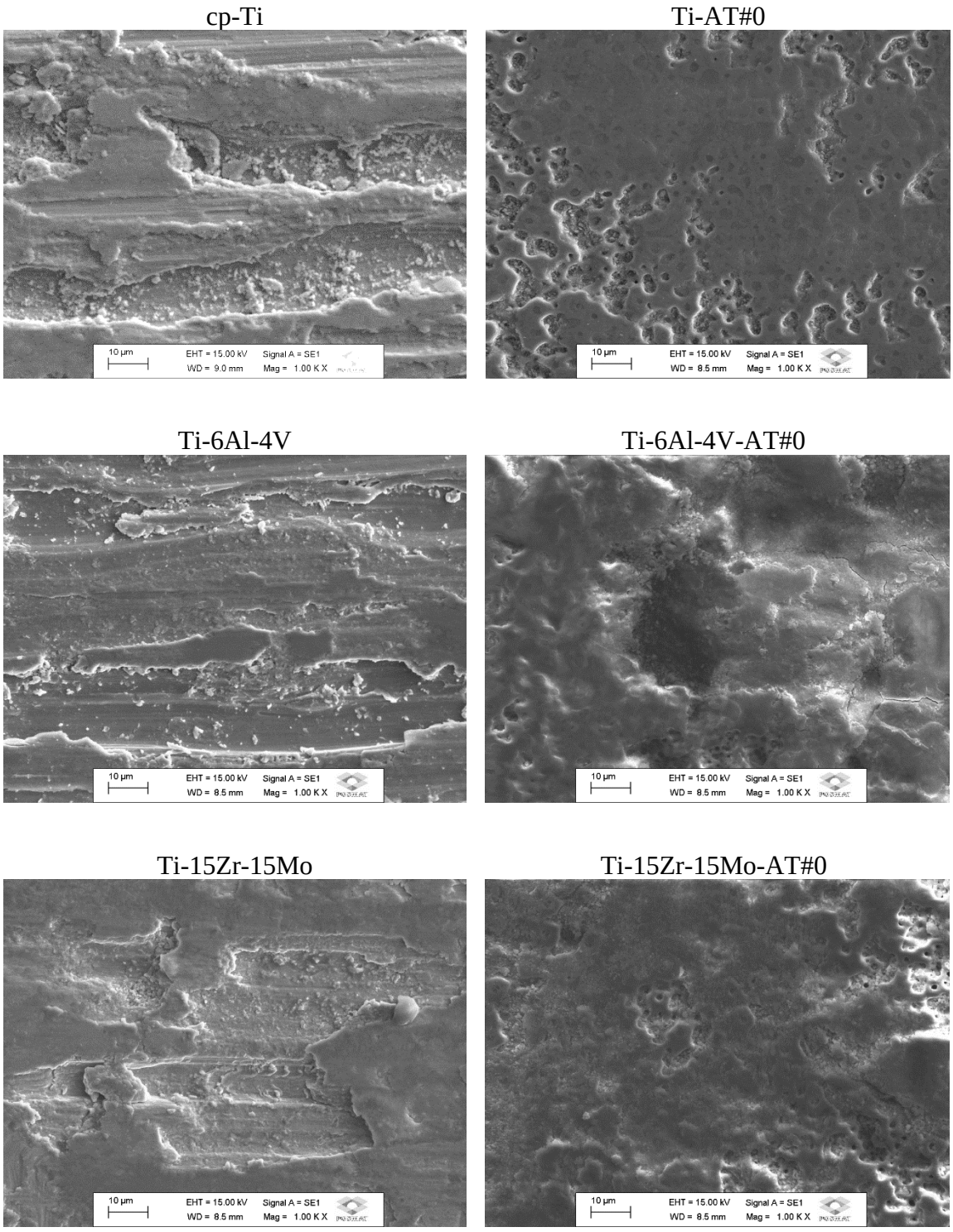

Figure 39 - SEM images of the wear tracks for the: cp-Ti; anodized Ti-AT#0; Ti-6Al-4V; anodized Ti-6Al-4V-AT#0; Ti-15Zr-15Mo; and anodized Ti-15Zr-15Mo-AT#0.

As can be seen by the representative tribocorrosion results (Fig. 37), for the untreated samples, the electrochemical potential values obtained by the tribocorrosion tests showed a drop of 155 mV for the Ti-15Zr-15Mo alloy, 429 mV for the cp-Ti and 640 mV of difference for the Ti-6Al-4V alloy. As already mentioned, the drop in the potential values, for the untreated samples, are related with the partially or fully removal of the passive film on the materials surface. In fact, the measured potential, after the destruction of the different passive layers, is a mixed potential between the areas with and without the passive film [122, 123]. The measured potential during sliding depends on the characteristics of the passive film (e.g., chemical composition, thickness and structure) as well as the base material [122, 123]. Martin et al. [124], in his work with different Ti-6Al-4V microstructure samples and their effect in the tribocorrosion behavior, found out that for the Ti-6Al-4V alloy, corrosion and wear behavior increased due to the formation of harder wear debris during sliding which can lead to abrasive wear. Therefore, the differences observed between cp-Ti and Ti-6Al-4V tests could be related with the different passive film characteristics and tribocorrosion mechanisms occurring during sliding. Also, it's possible to observe the presence of wear debris, scratches and oxide patches at the worn areas, this corroborates with the unstable COF values obtained for the untreated cp-Ti and Ti-6Al-4V.

For the MAO samples, no distinctive behavior regarding their electrochemical potential values were observed during the tribocorrosion test, exhibiting constant OCP values for the entire process. However, the Ti-6Al-4V-AT#0 alloys presented higher OCP values during the tribocorrosion tests when compared with the cp-Ti and Ti-15Zr-15Mo alloy. Also, the wear tracks exhibited in Figs. 38 and 39 showed only a plastic deformation on the top pores at the surface materials with some presence of debris accumulating at the lower topographic pores. In fact, it's possible to observe wider and more visible affected areas for the Ti-AT#0 and Ti-6Al-4V-AT#0, when compared with the Ti-15Zr-15Mo-AT#0.

In Fig. 40, it's shown the EDS spectra obtained from the worn areas. Also, Table 17 presents their chemical composition analysis.

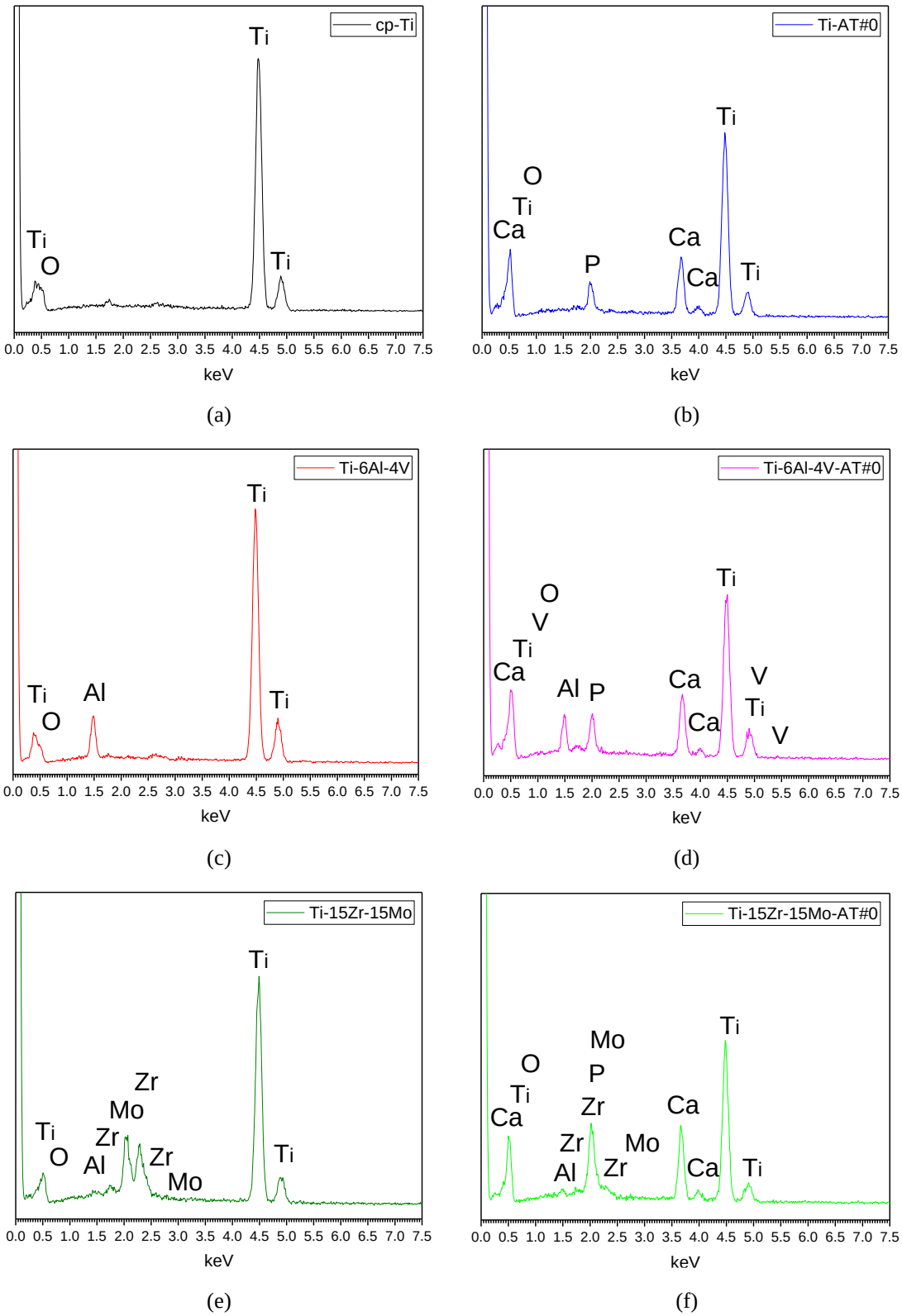

Figure 40 - EDS – Semi-quantitative analysis of the chemical composition from the worn areas of: a) cp-Ti; b) anodized cp-Ti; c) Ti-6Al-4V; d) anodized Ti-6Al-4V; e) as cast Ti-15Zr-15Mo; and e) anodized Ti-15Zr-15Mo.

Table 17- EDS – Semi-quantitative analysis of the chemical composition from the worn areas.

Samples	Ti (at.%)	Al (at.%)	V (at.%)	Zr (at.%)	Mo (at.%)	Ca (at.%)	P (at.%)	O (at.%)
cp-Ti	55.55 ± 3.06	-	-	-	-	-	-	44.46 ± 2.95
Ti-AT#0	22.97 ± 0.37	-	-	-	-	5.35 ± 0.14	2.70 ± 0.04	68.99 ± 0.57
Ti-6Al-4V	58.19 ± 1.14	6.93 ± 0.30	-	-	-	-	-	34.88 ± 1.06
Ti-6Al-4V-AT#0	21.67 ± 0.52	2.87 ± 0.83	-	-	-	4.52 ± 1.53	3.54 ± 0.05	67.39 ± 2.93
Ti-15Zr-15Mo	34.43 ± 1.73	0.23 ± 0.20	-	4.98 ± 0.36	4,90 ± 0.34	-	-	55.46 ± 2.40
Ti-15Zr-15Mo-AT#0	19.78 ± 1.79	0.30 ± 0.27	-	1.86 ± 0.25	0.78 ± 0.28	5.34 ± 1.79	4.32 ± 0.23	67.61 ± 0.66

As can be seen by Fig. 40 and Table 17, the chemical composition of the worn areas was affected by the tribocorrosion tests. For the untreated samples, it's possible to notice the presence of Ti and O along with some of the alloying elements for the Ti-6Al-4V and Ti-15Zr-15Mo alloys. The presence of O on the untreated samples could indicate the formation of an oxidative wear, which can be seen by the BSE representative SEM images (Fig. 38) [109]. Also, there is a higher O presence for the cp-Ti when compared with the Ti-6Al-4V. These results could be related with the higher potential values obtained for the cp-Ti, which can be an indication of the presence of oxide patches on the surface materials during the tribocorrosion tests which are known to decrease wear during sliding [109, 110]. For the MAO samples, the chemical composition analysis of the worn areas showed the presence of Ti, O, Ca, P, and the alloying elements: Al, for Ti-6Al-4V; and Zr and Mo, for Ti-15Zr-15Mo. Also, for the untreated and MAO condition of the Ti-15Zr-15Mo alloy, a small presence of Al was observed, indicating the material transfer from the counter body.

From these results, the Ti-6Al-4V and Ti-15Zr-15Mo MAO samples showed more interesting behavior when compared with the untreated samples and the Ti-AT#0. This behavior on their tribocorrosion could be related to the higher presence of the rutile phase for the anodized Ti-6Al-4V and Ti-15Zr-15Mo alloys (between 51 and 55%) when compared with the cp-Ti (28%). In fact, it's known that the presence of rutile phase improves the tribocorrosion behavior [11, 30, 52, 62, 81-83]. However, because of researches regarding the Ti-6Al-4V alloying elements toxicity effects [7, 23, 125], the Ti-15Zr-15Mo alloy showed a more

optimistic results, presenting similar electrochemical behavior. Therefore, the Ti-15Zr-15Mo alloy is a suitable option for a biomedical application regarding its electrochemical behavior when compared with cp-Ti and Ti-6A-4V.

5. CONCLUSIONS

This work aimed for the development and characterization of a functionalized surface on a β-type Ti-15Zr-15Mo alloy with MAO. Also, cp-Ti and Ti-6Al-4V alloy was used as control groups, which are commonly used as biomaterials for biomedical applications. For this purpose, the characterization of the microstructure, corrosion and tribocorrosion behavior was performed. The remarks of this work are as follows:

- The untreated cp-Ti, Ti-6Al-4V and Ti-15Zr-15Mo were characterized in terms of their microstructure and chemical composition (EDS). Where it was possible to observe their typical microstructure with: cp-Ti consisting of a α phase grains; Ti-6Al-4V composed of fine α phase grains along with β particles at the grain boundaries; and Ti-15Zr-15Mo presenting only β phase grains.
- Ti-15Zr-15Mo was functionalized by MAO, where EDS identified the presence of Ca and P bioactive elements at its surface. Also, Ti-15Zr-15Mo alloy exhibited a similar anodized surface when compared with cp-Ti and Ti-6Al-4V, with the presence of: bigger pores ("volcanoes"); smaller pores; cracks; and pore size/distribution ranging between 0.5 to 1.0 μm. On the other hand, the Ca/P ratio and the presence of the rutile phase was higher for the β-type alloy, when compared with cp-Ti and Ti-6Al-4V. Therefore, the Ti-15Zr-15Mo alloy presented the same interesting features from cp-Ti and Ti-6Al-4V, regarding the pore morphology and anodized surface, and also, it presented a slightly higher presence of rutile phase and Ca/P ratio.
- For the incorporation of HAp and ZnO particles, the samples showed no significant difference from the anodization without particles regarding their pore morphology, pore size/distribution, chemical composition, charge and anatase or rutile phase percentages. Also, no presence of the particles was identified by the studied conditions through the performed characterizations. Therefore, higher concentrations of the reagents should be considered.
- For the electrochemical behavior, the potentiodynamic polarization curves showed that Ti-15Zr-15Mo alloy presented higher potential (E_{corr}) and lower passivation current (i_{pass}) when compared with the cp-Ti and Ti-6Al-4V, between both untreated

and MAO conditions. However, for the electrochemical impedance spectroscopy analysis, the untreated Ti-6Al-4V native barrier oxide film presented higher resistance (R_{ox}) and similar capacitance (C_{ox}) when compared with cp-Ti and Ti-15Zr-15Mo alloy, indicating a higher protection of the passive oxide film. For the MAO samples, the Ti-15Zr-15Mo alloy presented lower capacitance values than cp-Ti and Ti-6Al-4V.

- For the tribocorrosion behavior, the untreated Ti-15Zr-15Mo alloy presented higher potential values during sliding when compared with cp-Ti and Ti-6Al-4V. For the MAO condition, all samples presented constant potential values during sliding, with higher potential values for the Ti-6Al-4V. Also, representative SEM images of the worn areas showed wider wear tracks with a more affected area for the untreated samples, with the MAO conditions presenting only plastic deformation on the top pores.

From these results and within the limitation of this work, it's possible to conclude that the Ti-15Zr-15Mo alloy presented similar or superior properties when compared with the cp-Ti and Ti-6Al-4V control groups. However, as it's widely known, the utilization of cp-Ti and Ti-6Al-4V alloy as biomaterials for biomedical purposes, still presents barriers due to biomechanical mismatches and/or toxicity problems. For this purpose, because of the excellent results obtained for the β-type Ti-15Zr-15Mo alloy when compared with cp-Ti and Ti-6Al-4V, the studied alloy is a suitable option as a biomaterial application.

6. FUTURE STEPS

In this section, it will be presented some of the future steps of this work:

- For a better understanding of the oxide film microstructure, X-ray photoelectron spectroscopy (XPS) and confocal laser scanning microscopy (CLSM) should be considered. In order to determine the different oxides that were formed at the surface between the cp-Ti, Ti-6Al-4V and Ti-15Zr-15Mo alloy.
- The measure of the dielectric strength of the oxide films or their thickness, in order to better understand the charge related of the anodization curves and the different behavior observed between the cp-Ti with the Ti-6Al-4V and Ti-15Zr-15Mo alloys.
- Higher concentrations of reagents aiming for a functionalized surface with the incorporation of particles.
- Confocal laser scanning microscopy (CLSM) of the wear tracks for the further study of the tribocorrosion behavior and mechanisms of the studied conditions.

7. REFERENCES

1. Williams, D.F., *On the nature of biomaterials.* Biomaterials, 2009. **30**(30): p. 5897-5909.
2. Festas, A., A. Ramos, and J. Davim, *Medical devices biomaterials–a review.* Proceedings of the Institution of Mechanical Engineers, Part L: Journal of Materials: Design and Applications, 2020. **234**(1): p. 218-228.
3. Kurtz, S.M., *PEEK biomaterials handbook*. 2019: William Andrew.
4. Williams, D.F., *On the mechanisms of biocompatibility.* Biomaterials, 2008. **29**(20): p. 2941-2953.
5. Oliveira, L.S.d.A.F., et al., *Biomateriais com aplicação na regeneração óssea–método de análise e perspectivas futuras.* Revista de Ciências Médicas e biológicas, 2010. **9**(1): p. 37-44.
6. Rogers, G.F. and A.K. Greene, *Autogenous bone graft: basic science and clinical implications.* Journal of Craniofacial Surgery, 2012. **23**(1): p. 323-327.
7. Niinomi, M., et al., *Biomedical titanium alloys with Young's moduli close to that of cortical bone.* Regenerative biomaterials, 2016. **3**(3): p. 173-185.
8. Hussein, M.A., A.S. Mohammed, and N. Al-Aqeeli, *Wear characteristics of metallic biomaterials: a review.* Materials, 2015. **8**(5): p. 2749-2768.
9. Ureña, J., et al., *Surface modification of powder metallurgy titanium by colloidal techniques and diffusion processes for biomedical applications.* Advanced Engineering Materials, 2017. **19**(6).
10. Correa, D., et al., *Tribocorrosion behavior of β-type Ti-15Zr-based alloys.* Materials Letters, 2016. **179**: p. 118-121.
11. Alves, A., et al., *Tribocorrosion behaviour of anodic treated titanium surfaces intended for dental implants.* Journal of Physics D: Applied Physics, 2013. **46**(40): p. 404001.
12. Kurtz, S., et al., *Projections of primary and revision hip and knee arthroplasty in the United States from 2005 to 2030.* Jbjs, 2007. **89**(4): p. 780-785.
13. Preston, J.S., D. KBateman, and A.J. Tria Jr, *Constraint in Revision Total Knee Arthroplasty.* Mastering Orthopedic Techniques REVISION KNEE ARTHROPLASTY, 2019: p. 131.
14. Kamath, A.F., et al., *Quantifying the Burden of Revision Total Joint Arthroplasty for Periprosthetic Infection.* The Journal of Arthroplasty, 2015. **30**(9): p. 1492-1497.
15. Old, A.B., W.J. Long, and W.N. Scott, *Revision of Total Knee Arthroplasties Performed in Young, Active Patients with Posttraumatic Arthritis and Osteoarthritis.* J Knee Surg, 2017. **30**(9): p. 905-908.
16. Lewallen, E.A., et al., *Biological strategies for improved osseointegration and osteoinduction of porous metal orthopedic implants.* Tissue Engineering Part B: Reviews, 2015. **21**(2): p. 218-230.
17. Su, Y., et al., *Bioinspired surface functionalization of metallic biomaterials.* Journal of the Mechanical Behavior of Biomedical Materials, 2018. **77**(Supplement C): p. 90-105.
18. Xiao, M., et al., *Bio-functionalization of biomedical metals.* Materials Science and Engineering: C, 2017. **70**(Part 2): p. 1057-1070.
19. Harun, W., et al., *A comprehensive review of hydroxyapatite-based coatings adhesion on metallic biomaterials.* Ceramics International, 2018. **44**(2): p. 1250-1268.
20. Baino, F. and I. Potestio, *Orbital implants: state-of-the-art review with emphasis on biomaterials and recent advances.* Materials Science and Engineering: C, 2016. **69**: p. 1410-1428.
21. Wang, X., et al., *Topological design and additive manufacturing of porous metals for bone scaffolds and orthopaedic implants: a review.* Biomaterials, 2016. **83**: p. 127-141.
22. Narushima, M., T. Nakai, and M. Niinomi, *Advances in metallic biomaterials: Processing and Applications.* Sendai: Springer, 2015.
23. Niinomi, M., *Design and development of metallic biomaterials with biological and mechanical biocompatibility.* Journal of Biomedical Materials Research Part A, 2019. **107**(5): p. 944-954.
24. Wang, K. and M. Li, *Effects of heat treatment and hot deformation on the secondary α phase evolution of TC8 titanium alloy.* Materials Science and Engineering: A, 2014. **613**: p. 209-216.
25. Liu, X., P.K. Chu, and C. Ding, *Surface modification of titanium, titanium alloys, and related materials for biomedical applications.* Materials Science and Engineering: R: Reports, 2004. **47**(3): p. 49-121.
26. Xavier, C.C., et al., *Low temperature heat treatments on Ti-15Zr-xMo alloys.* Journal of Alloys and Compounds, 2017. **727**: p. 246-253.
27. Shackelford, J.F., et al., *CRC materials science and engineering handbook*. 2016: CRC press.
28. Correa, D.R.N., P.A.B. Kuroda, and C.R. Grandini. *Structure, microstructure, and selected mechanical properties of Ti-Zr-Mo alloys for biomedical applications*. in *Advanced Materials Research*. 2014. Trans Tech Publ.
29. Correa, D., et al., *The effect of the solute on the structure, selected mechanical properties, and biocompatibility of Ti–Zr system alloys for dental applications.* Materials Science and Engineering: C, 2014. **34**: p. 354-359.
30. Oliveira, F.G., et al., *Understanding growth mechanisms and tribocorrosion behaviour of porous TiO2 anodic films containing calcium, phosphorous and magnesium.* Applied Surface Science, 2015. **341**: p. 1-12.
31. Harun, W., et al., *A comprehensive review of hydroxyapatite-based coatings adhesion on metallic biomaterials.* Ceramics International, 2017.
32. Alves, S.A., et al., *Synthesis of calcium-phosphorous doped TiO 2 nanotubes by anodization and reverse polarization: a promising strategy for an efficient biofunctional implant surface.* Applied Surface Science, 2017. **399**: p. 682-701.
33. Alves, S., et al., *TiO 2 nanotubes enriched with calcium, phosphorous and zinc: promising bio-selective functional surfaces for osseointegrated titanium implants.* RSC Advances, 2017. **7**(78): p. 49720-49738.

34. Alves, M.M., et al., *In vitro degradation of ZnO flowered coated Zn-Mg alloys in simulated physiological conditions.* Materials Science and Engineering: C, 2017. **70**(Part 1): p. 112-120.
35. Ho, W., C.-P. Ju, and J.C. Lin, *Structure and properties of cast binary Ti–Mo alloys.* Biomaterials, 1999. **20**(22): p. 2115-2122.
36. Oliveira, N.T., et al., *Development of Ti–Mo alloys for biomedical applications: Microstructure and electrochemical characterization.* Materials Science and Engineering: A, 2007. **452**: p. 727-731.
37. Martins Júnior, J.R.S., et al., *Preparation and characterization of Ti-15Mo alloy used as biomaterial.* Materials Research, 2011. **14**(1): p. 107-112.
38. Vicente, F.B., et al., *The influence of small quantities of oxygen in the structure, microstructure, hardness, elasticity modulus and cytocompatibility of Ti-Zr alloys for dental applications.* Materials, 2014. **7**(1): p. 542-553.
39. Correa, D.R.N., et al., *Effect of the substitutional elements on the microstructure of the Ti-15Mo-Zr and Ti-15Zr-Mo systems alloys.* Journal of Materials Research and Technology, 2015. **4**(2): p. 180-185.
40. Xavier, C.C., *Estudo de tratamentos térmicos da liga Ti-15Zr-xMo.* 2017.
41. Ho, W.-F., et al., *Structure, mechanical properties, and grindability of dental Ti–Zr alloys.* Journal of materials science: Materials in medicine, 2008. **19**(10): p. 3179-3186.
42. Hsu, H.-C., et al., *The structure and mechanical properties of as-cast Zr–Ti alloys.* Journal of alloys and Compounds, 2009. **488**(1): p. 279-283.
43. Martins Jr, J.R., et al., *Influence of oxygen content and microstructure on the mechanical properties and biocompatibility of Ti–15 wt% Mo alloy used for biomedical applications.* Materials, 2014. **7**(1): p. 232-243.
44. de Araújo, R.O., M.A.R. Buzalaf, and C.R. Grandini. *Preparation and characterization of Ti-10Mo-xZr alloys for biomedical applications*. in *Materials Science Forum*. 2016. Trans Tech Publ.
45. Kuroda, P.A.B., M.A.R. Buzalaf, and C.R. Grandini. *Preparation, microstructural characterization, and selected mechanical properties of Ti-20Zr-2.5 Mo and Ti-20Zr-7.5 Mo used as biomaterial*. in *Materials Science Forum*. 2016. Trans Tech Publ.
46. Kuroda, P.A.B., M.A.R. Buzalaf, and C.R. Grandini, *Effect of molybdenum on structure, microstructure and mechanical properties of biomedical Ti-20Zr-Mo alloys.* Materials Science and Engineering: C, 2016. **67**: p. 511-515.
47. Kuroda, P., et al., *Thermomechanical treatments influence on the phase composition, microstructure, and selected mechanical properties of Ti–20Zr–Mo alloys system for biomedical applications.* Journal of Alloys and Compounds, 2020. **812**: p. 152108.
48. Correa, D.R.N., et al. *Effect of Some Heat Treatments on Anelastic Properties of Ti-15Zr-xMo Alloys*. in *Materials Science Forum*. 2016. Trans Tech Publ.
49. Correa, D., et al., *Development of Ti-15Zr-Mo alloys for applying as implantable biomedical devices.* Journal of Alloys and Compounds, 2018. **749**: p. 163-171.
50. Correa, D., et al., *Microstructure and selected mechanical properties of aged Ti-15Zr-based alloys for biomedical applications.* Materials Science and Engineering: C, 2018. **91**: p. 762-771.
51. Correa, D., et al., *Adjustment of the microstructure and selected mechanical properties of biomedical Ti-15Zr-Mo alloys through oxygen doping.* Journal of Alloys and Compounds, 2019. **775**: p. 158-167.
52. Correa, D., et al., *On the mechanical biocompatibility of Ti-15Zr-based alloys for potential use as load-bearing implants.* Journal of Materials Research and Technology, 2020. **9**(2): p. 1241-1250.
53. Abdel-Hady, M., K. Hinoshita, and M. Morinaga, *General approach to phase stability and elastic properties of β-type Ti-alloys using electronic parameters.* Scripta Materialia, 2006. **55**(5): p. 477-480.
54. Abdel-Hady, M., et al., *Change in anisotropy of mechanical properties with β-phase stability in high Zr-containing Ti-based alloys.* Materials Science and Engineering: A, 2008. **480**(1-2): p. 167-174.
55. Doni, Z., et al., *Tribocorrosion behaviour of hot pressed CoCrMo−Al2O3 composites for biomedical applications.* Tribology - Materials, Surfaces & Interfaces, 2014. **8**(4): p. 201-208.
56. Toptan, F., et al., *Corrosion and tribocorrosion behavior of Ti–B4C composite intended for orthopaedic implants.* Journal of the Mechanical Behavior of Biomedical Materials, 2016. **61**(Supplement C): p. 152-163.
57. Alves, S.A., et al., *Tribo-electrochemical behavior of bio-functionalized TiO2 nanotubes in artificial saliva: Understanding of degradation mechanisms.* Wear, 2017. **384-385**(Supplement C): p. 28-42.
58. Costa, B.C., et al., *Exposure effects of endotoxin-free titanium-based wear particles to human osteoblasts.* Journal of the mechanical behavior of biomedical materials, 2019. **95**: p. 143-152.
59. Çaha, I., et al., *Corrosion and tribocorrosion behaviour of titanium nitride thin films grown on titanium under different deposition times.* Surface and Coatings Technology, 2019. **374**: p. 878-888.
60. Alves, S.A., et al., *Improved tribocorrosion performance of bio-functionalized TiO2 nanotubes under two-cycle sliding actions in artificial saliva.* Journal of the mechanical behavior of biomedical materials, 2018. **80**: p. 143-154.
61. Gao, A., et al., *Electrochemical surface engineering of titanium-based alloys for biomedical application.* Electrochimica Acta, 2018. **271**: p. 699-718.
62. Oliveira, F.G.M.d., *Biofunctionalization of titanium surfaces for dental implants: osteogenic, anti-microbial and tribocorrosion resistant surfaces.* 2015.
63. Kulkarni, M., et al., *Biomaterial surface modification of titanium and titanium alloys for medical applications.* Nanomedicine, 2014. **111**: p. 111.
64. Wang, X., et al., *Influence of surface structures on biocompatibility of TiO2/HA coatings prepared by MAO.* Materials Chemistry and Physics, 2018. **215**: p. 339-345.
65. Brunette, D.M., et al., *Titanium in medicine: material science, surface science, engineering, biological responses and medical applications*. 2012: Springer Science & Business Media.

66. Alves, S., et al., *Tribocorrosion behavior of calcium-and phosphorous-enriched titanium oxide films and study of osteoblast interactions for dental implants.* Journal of Bio-and Tribo-Corrosion, 2015. **1**(3): p. 23.
67. Runa, M., et al., *First insight on the impact of an osteoblastic layer on the bio-tribocorrosion performance of Ti6Al4V hip implants.* Acta biomaterialia, 2015. **12**: p. 341-351.
68. Ribeiro, A., et al., *Micro-arc oxidation as a tool to develop multifunctional calcium-rich surfaces for dental implant applications.* Materials Science and Engineering: C, 2015. **54**: p. 196-206.
69. Alves, S.A., et al., *Synthesis of calcium-phosphorous doped TiO2 nanotubes by anodization and reverse polarization: A promising strategy for an efficient biofunctional implant surface.* Applied Surface Science, 2017. **399**: p. 682-701.
70. Doni, Z., et al., *Tribocorrosion behaviour of hot pressed CoCrMo− HAP biocomposites.* Tribology International, 2015. **91**: p. 221-227.
71. Costa, B., et al., *ZnO Nanoparticles with Different Sizes and Morphologies for Medical Implant Coatings: Synthesis and Cytotoxicity.* BioNanoScience, 2018. **8**(2): p. 587-595.
72. Ferraris, S. and S. Spriano, *Antibacterial titanium surfaces for medical implants.* Materials Science and Engineering: C, 2016. **61**: p. 965-978.
73. Alves, A.C., et al., *Tribocorrosion behaviour of anodic treated titanium surfaces intended for dental implants.* Journal of Physics D: Applied Physics, 2013. **46**(40): p. 404001.
74. Duarte, L.T., et al., *Surface characterization of oxides grown on the Ti–13Nb–13Zr alloy and their corrosion protection.* Corrosion Science, 2013. **72**: p. 35-40.
75. Zhe, W., et al., *Facile incorporation of hydroxyapatite onto an anodized Ti surface via a mussel inspired polydopamine coating.* Applied Surface Science, 2016. **378**: p. 496-503.
76. Kim, D.-Y., et al., *Formation of hydroxyapatite within porous TiO2 layer by micro-arc oxidation coupled with electrophoretic deposition.* Acta Biomaterialia, 2009. **5**(6): p. 2196-2205.
77. Alves, A.C., et al., *Corrosion mechanisms in titanium oxide-based films produced by anodic treatment.* Electrochimica Acta, 2017. **234**(Supplement C): p. 16-27.
78. Wu, L., et al., *Effect of anodization time on morphology and electrochemical impedance of andic oxide films on titanium alloy in tartrate solution.* Int. J. Electrochem. Sci, 2014. **9**: p. 5012-5024.
79. Kirmanidou, Y., et al., *New Ti-alloys and surface modifications to improve the mechanical properties and the biological response to orthopedic and dental implants: a review.* BioMed research international, 2016. **2016**.
80. Mousa, H.M., C.H. Park, and C.S. Kim, *Surface modification of magnesium and its alloys using anodization for orthopedic implant application.* Magnesium Alloys, 2017: p. 219.
81. Rafieian, D., et al., *Controlled formation of anatase and rutile TiO2 thin films by reactive magnetron sputtering.* AIP advances, 2015. **5**(9): p. 097168.
82. Corrêa, P., *Deposição por sputtering de filmes finos resistentes à tribocorrosão, sobre titânio, visando aplicações biológicas.* 2020.
83. Hanaor, D.A. and C.C. Sorrell, *Review of the anatase to rutile phase transformation.* Journal of Materials science, 2011. **46**(4): p. 855-874.
84. Silva, J.I., et al., *Corrosion and tribocorrosion behavior of Ti−TiB−TiNx in-situ hybrid composite synthesized by reactive hot pressing.* Journal of the Mechanical Behavior of Biomedical Materials, 2017. **74**(Supplement C): p. 195-203.
85. Tiburtius, E.R.L. and E.W. Scheffer, *Triclosan: Destino no Meio Ambiente e Perspectivas no tratamento de águas de abastecimento público.* Revista Virtual de Química, 2014. **6**(5): p. 1144-1159.
86. Jacobs, J.J., J.L. Gilbert, and R.M. Urban, *Current concepts review-corrosion of metal orthopaedic implants.* Jbjs, 1998. **80**(2): p. 268-82.
87. Shreir, L., *1.05-Basic Concepts of Corrosion.* Shreir's Corrosion. Oxford: Elsevier, 2010: p. 89-100.
88. Souza, J.C., et al., *How do titanium and Ti6Al4V corrode in fluoridated medium as found in the oral cavity? An in vitro study.* Materials Science and Engineering: C, 2015. **47**: p. 384-393.
89. Virtanen, S., et al., *Special modes of corrosion under physiological and simulated physiological conditions.* Acta Biomaterialia, 2008. **4**(3): p. 468-476.
90. Cruz, H., et al., *Tribocorrosion and bio-tribocorrosion in the oral environment: the case of dental implants.* Biomedical tribology, 2011: p. 1-33.
91. Pourbaix, M., *Atlas of Electrochemical Equilibria in Aqueous Solutions, trans.* JA Franklin (Houston, TX: NACE International, 1974), 1966. **256**.
92. Barão, V.A., et al., *Stability of cp-Ti and Ti-6 Al-4 V alloy for dental implants as a function of saliva pH–an electrochemical study.* Clinical oral implants research, 2012. **23**(9): p. 1055-1062.
93. Robin, A. and O. Carvalho, *Influence of pH and fluoride species on the corrosion behavior of ti-xnb-13zr alloys in ringer's solution.* Advances in Materials Science and Engineering, 2013. **2013**.
94. Souza, J.C., et al., *Corrosion behaviour of titanium in the presence of Streptococcus mutans.* Journal of dentistry, 2013. **41**(6): p. 528-534.
95. Koike, M. and H. Fujii, *The corrosion resistance of pure titanium in organic acids.* Biomaterials, 2001. **22**(21): p. 2931-2936.
96. Poorqasemi, E., et al., *Investigating accuracy of the Tafel extrapolation method in HCl solutions.* Corrosion Science, 2009. **51**(5): p. 1043-1054.
97. McCafferty, E., *Validation of corrosion rates measured by the Tafel extrapolation method.* Corrosion science, 2005. **47**(12): p. 3202-3215.
98. Development, K.D.a. *Tafel Region Extrapolation*. [cited 2020 nov 22]; Available from: http://www.khdesign.co.uk/TechTafel.htm.

99. Ellis, C.L., et al., *Ion Migration in Hybrid Perovskites: Evolving Understanding of a Dynamic Phenomenon*, in *Perovskite Photovoltaics*. 2018, Elsevier. p. 163-196.
100. Atrens, A., et al., *Understanding the corrosion of Mg and Mg alloys.* 2017.
101. Telegdi, J., A. Shaban, and G. Vastag, *Biocorrosion-steel*, in *Encyclopedia of Interfacial Chemistry: Surface Science and Electrochemistry*. 2018, Elsevier. p. 28-42.
102. Walter, G., *A review of impedance plot methods used for corrosion performance analysis of painted metals.* Corrosion Science, 1986. **26**(9): p. 681-703.
103. Alves, A., et al., *Corrosion mechanisms in titanium oxide-based films produced by anodic treatment.* Electrochimica Acta, 2017. **234**: p. 16-27.
104. Celis, J.-P., P. Ponthiaux, and F. Wenger, *Tribo-corrosion of materials: interplay between chemical, electrochemical, and mechanical reactivity of surfaces.* Wear, 2006. **261**(9): p. 939-946.
105. Ponthiaux, P., F. Wenger, and J.-P. Celis, *Tribocorrosion: material behavior under combined conditions of corrosion and mechanical loading.* Corrosion Resistance, 2012: p. 81-106.
106. Peng, J.-F., M.-X. Shen, and Z.-B. Cai, *Nano Diesel Soot Particles Reduce Wear and Friction Performance Using an Oil Additive on a Laser Textured Surface.* Coatings, 2018. **8**(3): p. 89.
107. Group, M.R. *Tribology*. [cited 2020 nov 22]; Available from: https://faculty.ucmerced.edu/amartini/tribology.shtml.
108. Costa, N.d.A.d., *Desenvolvimento de filmes de óxido de titânio biofuncionalizados com gradiente estrutural e químico sobre a liga Ti-40Nb para aplicação em implantes osseointegrados.* 2020.
109. Toptan, F., et al., *Tribocorrosion behavior of bio-functionalized highly porous titanium.* Journal of the mechanical behavior of biomedical materials, 2017. **69**: p. 144-152.
110. Mathew, M., et al., *Tribocorrosion behavior of CoCrMo alloy for hip prosthesis as a function of loads: a comparison between two testing systems.* Wear, 2011. **271**(9-10): p. 1210-1219.
111. Ratner, B.D., et al., *Biomaterials science: an introduction to materials in medicine*. 2004: Elsevier.
112. Dedavid, B.A., C.I. Gomes, and G. Machado, *Microscopia eletrônica de varredura: aplicações e preparação de amostras: materiais poliméricos, metálicos e semicondutores*. 2007: EdiPUCRS.
113. Wang, Y., et al., *Review of the biocompatibility of micro-arc oxidation coated titanium alloys.* Materials & design, 2015. **85**: p. 640-652.
114. Shin, K.R., et al., *In vitro biological response to the oxide layer in pure titanium formed at different current densities by plasma electrolytic oxidation.* Applied surface science, 2014. **314**: p. 221-227.
115. Ishizawa, H. and M. Ogino, *Formation and characterization of anodic titanium oxide films containing Ca and P.* Journal of biomedical materials research, 1995. **29**(1): p. 65-72.
116. Wang, Y., et al., *Growth, microstructure and mechanical properties of microarc oxidation coatings on titanium alloy in phosphate-containing solution.* Applied Surface Science, 2004. **233**(1-4): p. 258-267.
117. Elorz, P.-S. and Castro, *Structural Materials*. 2019: Springer.
118. Matykina, E., et al., *Stability of plasma electrolytic oxidation coating on titanium in artificial saliva.* Journal of Materials Science: Materials in Medicine, 2013. **24**(1): p. 37-51.
119. Orazem, M.E. and B. Tribollet, *Electrochemical impedance spectroscopy.* New Jersey, 2008.
120. Diomidis, N., et al., *A methodology for the assessment of the tribocorrosion of passivating metallic materials.* Lubrication science, 2009. **21**(2): p. 53-67.
121. Ponthiaux, P., et al., *Electrochemical techniques for studying tribocorrosion processes.* Wear, 2004. **256**(5): p. 459-468.
122. Ureña, J., et al., *Corrosion and tribocorrosion behaviour of β-type Ti-Nb and Ti-Mo surfaces designed by diffusion treatments for biomedical applications.* Corrosion Science, 2018. **140**: p. 51-60.
123. Neto, M., *Understanding the wear and tribocorrosion processes and mechanisms of titanium alloys in bovine serum solution*. 2019, University of Sheffield.
124. Martin, É., et al., *Influence of microstructure and texture on the corrosion and tribocorrosion behavior of Ti–6Al–4V.* Tribology International, 2010. **43**(5-6): p. 918-924.
125. Kuroda, D., et al., *Design and mechanical properties of new β type titanium alloys for implant materials.* Materials Science and Engineering: A, 1998. **243**(1-2): p. 244-249.

8. ANNEX

8.1. XRD Cards

8.1.1. Ti – α phase

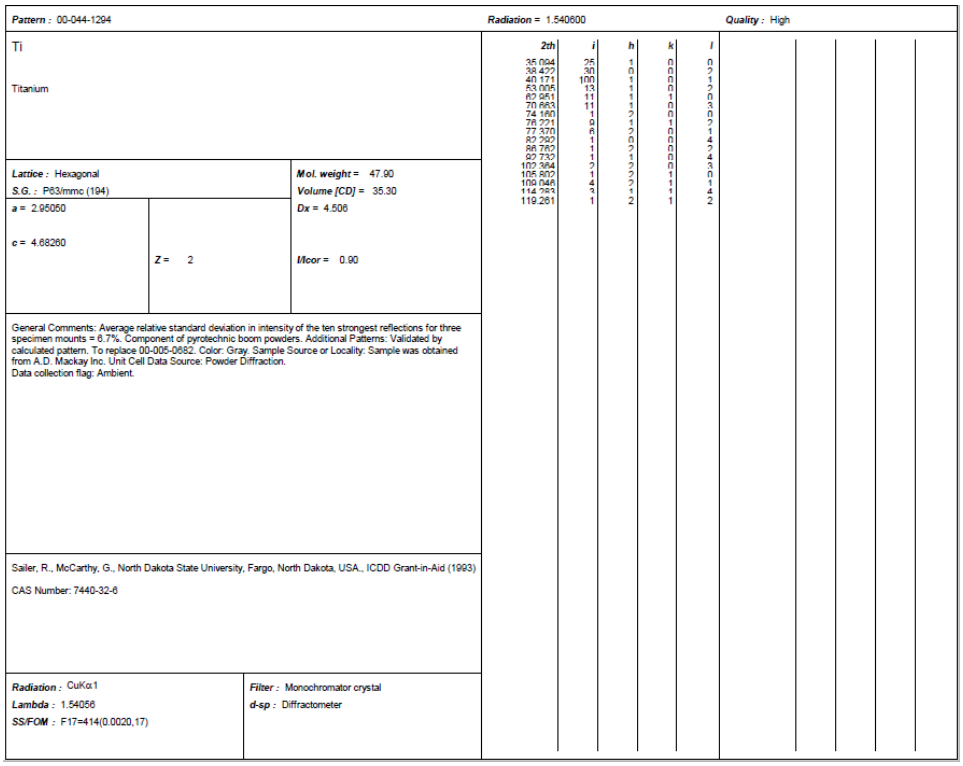

Pattern : 00-044-1294 **Radiation =** 1.540600 **Quality :** High

Ti

Titanium

Lattice : Hexagonal
S.G. : P63/mmc (194)

a = 2.95050
c = 4.68260

Z = 2

Mol. weight = 47.90
Volume [CD] = 35.30
Dx = 4.506
Micor = 0.90

General Comments: Average relative standard deviation in intensity of the ten strongest reflections for three specimen mounts = 6.7%. Component of pyrotechnic boom powders. Additional Patterns: Validated by calculated pattern. To replace 00-005-0682. Color: Gray. Sample Source or Locality: Sample was obtained from A.D. Mackay Inc. Unit Cell Data Source: Powder Diffraction.
Data collection flag: Ambient.

Sailer, R., McCarthy, G., North Dakota State University, Fargo, North Dakota, USA., ICDD Grant-in-Aid (1993)

CAS Number: 7440-32-6

Radiation : CuKα1
Lambda : 1.54056
SS/FOM : F17=414(0.0020,17)

Filter : Monochromator crystal
d-sp : Diffractometer

2th	i	h	k	l
35.094	25	1	0	0
38.427	30	0	0	2
40.171	100	1	0	1
53.005	13	1	0	2
62.951	11	1	1	0
70.683	11	1	0	3
74.160	1	2	0	0
76.271	9	1	1	2
77.370	6	2	0	1
82.292	1	0	0	4
86.782	1	2	0	2
92.732	1	1	0	4
103.364	2	2	0	3
105.802	1	2	1	0
109.046	4	2	1	1
114.283	3	1	1	4
119.261	1	2	1	2

8.1.2. TiO_2 – anatase

Pattern : 01-071-1169 **Radiation =** 1.540600 **Quality :** High

TiO_2

Titanium Oxide
Also called: Anatase

Lattice : Body-centered tetragonal
S.G. : I41/amd (141)

a = 3.80400
c = 9.61400
Z = 4

Mol. weight = 79.90
Volume [CD] = 139.12
Dx = 3.815
I/Icor = 4.80

Additional Patterns: See PDF 01-071-1167. ANX: AX2. Analysis: O2 Ti1. Formula from original source: Ti O2.
ICSD Collection Code: 9855. Sample Source or Locality: Specimen from Binntal, Wallis, Switzerland.
Temperature of Data Collection: 1073 K. Wyckoff Sequence: e a (I41/AMDS).
Data collection flag: Non ambient temperature.

Calculated from ICSD using POWD-12++ (2004)
Horn, M., Schwerdtfeger, C.F., Meagher, E.P., Z. Kristallogr., Kristallgeom., Kristallphys., Kristallchem., volume 136, page 273 (1972)

Radiation : CuKα1
Lambda : 1.54060
SS/FOM : F30=1000(0.0002,34)

Filter :
d-sp : Calculated spacings

2th	i	h	k	l
25.156	999	1	0	1
36.837	59	1	0	3
37.685	176	0	0	4
38.314	69	1	1	2
47.782	218	2	0	0
53.344	133	1	0	5
54.782	130	2	1	1
61.680	23	2	1	3
62.191	92	2	0	4
68.082	40	1	1	6
69.864	40	2	2	0
73.210	4	1	0	7
74.397	59	2	1	5
75.578	16	3	0	1
76.730	3	0	0	8
81.564	4	3	0	3
82.039	28	2	2	4
82.815	13	3	1	2
83.245	4	2	1	7
83.387	11	3	0	5
84.530	13	3	2	1
87.007	8	1	0	9
88.613	8	2	0	8
100.468	4	3	2	3
106.399	16	3	1	6
108.190	7	4	0	0
111.544	1	3	0	7
112.775	13	3	2	5
114.015	8	4	1	1
116.812	14	1	1	10
118.746	13	2	1	9
118.542	4	2	2	8
120.646	3	4	1	3
121.171	10	4	0	4
121.840	3	3	3	2
126.482	3	1	0	11
129.807	11	3	1	8
*129.807	11	4	2	0
134.048	2	3	2	7
135.656	10	4	1	5
141.005	4	3	0	9
147.740	14	4	2	4

8.1.3. TiO_2 – rutile

Pattern : 00-021-1276 **Radiation =** 1.540600 **Quality :** High

TiO_2

Titanium Oxide
Also called: titania, Rutile, syn

Lattice : Tetragonal
S.G. : P42/mnm (136)

a = 4.59330
c = 2.95920

Z = 2

Mol. weight = 79.90
Volume [CD] = 62.43
Dx = 4.250
Dm = 4.230
I/Icor = 3.40

General Comments: Pattern reviewed by Syvinski, W., McCarthy, G., North Dakota State Univ, Fargo, North Dakota, USA, ICDD Grant-in-Aid (1990). Agrees well with experimental and calculated patterns. Additional weak reflections (indicated by brackets) were observed. Naturally occurring material may be reddish brown. Additional Patterns: Validated by calculated pattern. Analysis: No impurity over 0.001%. Color: White. Polymorphism/Phase Transition: Two other polymorphs, anatase (tetragonal) and brookite (orthorhombic), converted to rutile on heating above 700 C. Reflectance: Opaque mineral optical data on specimen from Sweden: R3R%=20.3, Disp.=Std. Sample Source or Locality: Sample obtained from National Lead Co., South Amboy, New Jersey, USA. Temperature of Data Collection: Pattern taken at 298 K. Vickers Hardness Number: VHN100=1132-1187. Unit Cell Data Source: Powder Diffraction.
Data collection flag: Ambient.

Natl. Bur. Stand. (U.S.) Monogr. 25, volume 7, page 83 (1969)

Radiation : CuKα1
Lambda : 1.54056
SS/FOM : F30=108(0.0080,32)

Filter : Monochromator crystal
d-sp : Not given

2th	i	h	k	l
27.447	100	1	1	0
36.088	50	1	0	1
39.186	8	2	0	0
41.226	25	1	1	1
44.052	10	2	1	0
54.323	60	2	1	1
56.642	20	2	2	0
62.742	10	0	0	2
64.040	10	3	1	0
65.480	2	3	2	1
69.010	20	3	0	1
69.790	12	1	1	2
72.410	2	3	1	1
74.411	1	3	2	0
76.510	4	2	0	2
79.872	2	3	1	2
82.335	8	3	2	1
84.260	4	4	0	0
87.464	2	4	1	0
89.557	8	3	3	2
90.708	4	3	3	0
95.275	8	4	1	1
96.017	8	3	1	2
97.177	4	4	2	0
98.514	1	3	3	1
105.569	2	4	2	1
106.019	2	1	0	3
109.406	2	1	1	3
116.227	4	4	0	2
117.827	4	5	1	0
120.052	8	2	1	3
122.788	8	4	3	1
123.880	8	3	3	2
131.847	8	4	2	2
136.549	8	3	0	3
140.052	12	5	2	1
143.116	2	4	4	0
155.870	2	5	3	0

8.1.4. Ti – β phase

Pattern : 01-089-4913 **Radiation =** 1.540600 **Quality :** Indexed

Ti

Titanium
Also called: β-Ti

Lattice : Body-centered cubic
S.G. : Im-3m (229)
a = 3.28300
Z = 2
Mol. weight = 47.90
Volume [CD] = 35.38
Dx = 4.496
I/Icor = 9.61

ANX: N. ICSD Collection Code: 76165. Other Cell: Cell from Z. Kristallogr., Kristallogeom., Kristallphys., Kristallchem., 94 299-300 (1936): 3.32 at 1173 K. Calculated Pattern Original Remarks: REM M PDF 00-044-1288. REM M Stable above 1155 K. REM M Cell at 1173 K: 3.312. REM TEM 298. Temperature of Data Collection: 298 K. Test from ICSD: At least one TF missing. No R value given. Minor Warning: No R value given in the paper. Wyckoff Sequence: a (IM3-M). Unit Cell Data Source: Powder Diffraction.
Data collection flag: Ambient.

Calculated from ICSD using POWD-12++
Levinger, B.W., J. Met., volume 5, page 195 (1953)

Radiation : CuKα1
Lambda : 1.54060
SS/FOM : F4=1000(0.0000,4)
Filter :
d-sp : Calculated spacings

2th	i	h	k	l
38.759	999	1	1	0
55.973	127	2	0	0
70.163	202	2	1	1
83.156	52	2	2	0

8.1.5. HAp

PDF Number	01-080-6199		**Status**	Primary	**Quality Mark**		Star
Pressure/Temperature	Ambient						
Chemical Formula	Ca10 (P O4)6 (O H)2						
Structural Formula							
Empirical Formula	Ca10 H2 O26 P6						
Weight %	Ca39.90 H0.20 O41.41 P18.50						
Atomic %	Ca22.73 H4.55 O59.09 P13.64						
Compound Name	Calcium Phosphate Hydroxide						
ANX	A3B5X13						
Mineral Name	Hydroxylapatite, syn						
Also Called							
Experimental	**Rad**	***I***	**Filter**	**d-Spacing**	**Cutoff**	**Intensity**	**I/Ic**
	CuKá1	1.5406		Calculated		Calculated	1.09
	I/Ic - ND	**Camera Diameter**					
Physical	**SYS**	**Space Group**	**Aspect**	**Modulation Wave Vectors**			
	Hexagonal	P63/m (176)		-			
	Subsystems	ID W Matrix					
	Author's Cell	**a**	**b**	**c**	*a*	*b*	*g*
		9.4207(1)		6.8817(1)			
		Volume	**Z**	**Molecular Volume/Formula Unit Volume**			
		528.92	1.00	528.92			
	Author's Cell Axial Ratio	**c/a**	**a/b**	**c/b**			
		0.730					
	Density	**Dcalc**	**Dmeas**	**Dstruc**			
		3.154		3.15			
	SS/FOM	**Temperature**	**Melting Point**	**R-factor**	**Error**	**Color**	
	F(30) = 999.9 (0.0000, 31)	293.0		0.059			
Crystal	**Space Group**	**Molecular Weight**					
	P63/m (176)	1004.64					
	Crystal Data	**a**	**b**	**c**	*a*	*b*	*g*
		9.421	9.421	6.882	90.00	90.00	120.00
		Volume	**Z**				
		528.92	1.00				
	Crystal Data Axial Ratio	**c/a**	**a/b**	**c/b**			
		0.730	1.000	0.730			

	Reduced Cell	**a**	**b**	**c**	*a*	*b*	*g*
		6.882	9.421	9.421	120.00	90.00	90.00
		Volume					
		528.92					
Optical	*ea*	**n***wb*	*eg*	**Sign**	**2V**		
Structure							
	ADP Type						
	Origin						
	Crystal (Symmetry Allowed)	Centrosymmetric					
	SG Symmetry Operators	Seq Operator					
	SG Symmetry Operators (Modulated Structure)	Seq Operator					
	Atomic Coordinates	Atom Num Wyckoff Symmetry x y z SOF IDP AET					
	Atomic Coordinates (Modulated)	Atom Num Wyckoff x y z SOF IDP Subsys					
	Anisotropic Displacement Parameters	Atom Num ADP11 ADP22 ADP33 ADP12 ADP13 ADP23					
	Anisotropic Displacement Parameters (Modulated)	Atom Num ADP11 ADP22 ADP33 ADP12 ADP13 ADP23					
Modulated	**Positional Displacement Parameters**	Atom Site Axis WV ID Cos Sin					
	Atomic Displacement Parameters	Atom Site WV ID Cos Sin Tensor El.					
	Occupation Modulation	Atom Site WV ID Cos Sin					
	Occupational - Crenel	Atom Site C W					
	Displacement - SawTooth	Atom Site C W AX AY AZ					
Miscellaneous	**Subfiles**	Ceramic (Bioceramic), Common Phase, Forensic, Inorganic, Mineral Related (Mineral , Synthetic), Pharmaceutical (Excipient)					
	Former PDF #						
	Prototype Structure	Ca5 P3 O12 F					

	Prototype Structure (Alpha Sort)	
	LPF Prototype Structure	
	LPF Prototype Structure (Alpha Sort)	
	Mineral Classification	Apatite (Group), phosphate (Subgroup)
	Zeolite Classification	
	Pearson	hP44.00
	Pearson w/o H	hP42
	Cross-References	✓ 01-074-0565 (Alternate), 01-074-0566 (Alternate), 01-079-8093 (Alternate), 01-079-9908 (Alternate), 04-017-1626 (Related Phase)
	CAS Number	
	Entry Date	09/01/2013
	Last Modification Date	
	Last Modifications	

References

Type	DOI	Reference
Primary Reference		Calculated from ICSD using POWD-12++.
Structure		"Unexpected mechanism of Zn(2+) insertion in calcium phosphate bioceramics". Gomes, S., Nedelec, J.M., Jallot, E., Sheptyakov, D., Renaudin, G. Chem. Mater. 23, 3072 (2011).

Comments

Database Comments	ANX: A3B5X13. Analysis: H2 Ca10 O26 P6. Formula from original source: Ca10 (P O4)6 (O H)2. ICSD Collection Code: 183744. Temperature of Data Collection: 293 K. Wyckoff Sequence: i h4 f e (P63/M). Unit Cell Data Source: Powder Diffraction.
User Comments	
Shared Comments	

d-Spacings

I =Cu Kα1 1.54056 Å

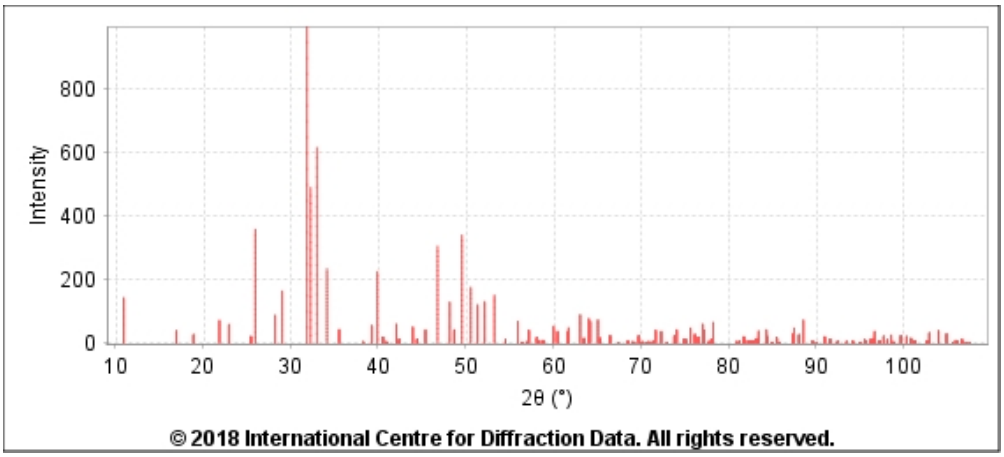

Ca10 (P O4)6 (O H)2 - 01-080-6199 (Stick, Fixed Slit Intensity)

2*q*	d(Å)	Intensity	h	k	l	m	n	o	*
10.8351	8.158570	143	1	0	0				
16.8405	5.260290	39	1	0	1				
18.8236	4.710350	27	1	1	0				
21.7687	4.079280	72	2	0	0				
22.8597	3.887010	59	1	1	1				
25.3604	3.509100	21	2	0	1				
25.8721	3.440850	358	0	0	2				
28.1224	3.170420	88	1	0	2				
28.9307	3.083650	164	1	2	0				
31.7723	2.814050	999	1	2	1				
32.1899	2.778490	490	1	1	2				
32.9075	2.719520	616	3	0	0				
34.0593	2.630140	234	2	0	2				
35.4629	2.529190	43	3	0	1				
38.1806	2.355180	3	2	2	0				
39.1971	2.296410	56	2	1	2				
39.8041	2.262780	225	1	3	0				
40.4469	2.228290	19	2	2	1				
40.8298	2.208270	3	1	0	3				
41.9970	2.149560	60	1	3	1				
42.3266	2.133580	12	3	0	2				
43.8628	2.062350	51	1	1	3				
44.3770	2.039640	12	4	0	0				
45.3180	1.999450	42	2	0	3				
46.6987	1.943500	305	2	2	2				
48.0865	1.890600	130	1	3	2				
48.6033	1.871700	42	2	3	0				
49.4820	1.840500	340	2	1	3				
50.4901	1.806090	176	2	3	1				

51.2728	1.780340	121	1	4	0				
52.0826	1.754550	131m	3	0	3				
52.0826	1.754550	m	4	0	2				
53.1957	1.720430	151	0	0	4				
54.4613	1.683400	10	1	0	4				
55.8721	1.644190	68	3	2	2				
56.3374	1.631710	1	5	0	0				
56.9344	1.616010	3	1	1	4				
57.1308	1.610920	41	1	3	3				
58.0456	1.587690	18	5	0	1				
58.3059	1.581220	8	1	4	2				
58.7583	1.570120	8	3	3	0				
59.9459	1.541820	53	2	4	0				
60.4231	1.530780	37	3	3	1				
61.5912	1.504520	37	2	4	1				
61.6872	1.502410	48	1	2	4				
62.9945	1.474340	90	5	0	2				
63.4272	1.465320	15	1	5	0				
63.9833	1.453920	78	3	0	4				
64.1670	1.450200	69	3	2	3				
65.0216	1.433190	74	1	5	1				
65.2651	1.428430	16	3	3	2				
66.4156	1.406450	24	1	4	3				
67.3473	1.389240	1	2	2	4				
68.4496	1.369530	5	1	3	4				
69.0106	1.359760	3	6	0	0				
69.1616	1.357160	1	1	0	5				
69.6897	1.348160	24	5	1	2				
70.1007	1.341260	3	4	3	0				
70.5406	1.333970	1	6	0	1				
70.8047	1.329640	3	5	0	3				
71.3321	1.321100	4	1	1	5				
71.6203	1.316490	41m	4	0	4				
71.6203	1.316490	m	4	3	1				
72.2589	1.306420	37	5	2	0				
72.9545	1.295670	2	3	3	3				
73.7606	1.283490	23	2	5	1				
74.0201	1.279630	42	2	4	3				
74.9093	1.266630	13	2	3	4				
75.0503	1.264600	12	6	0	2				
75.5954	1.256830	47	2	1	5				
76.1055	1.249670	28	3	4	2				
76.5026	1.244170	19	1	6	0				
77.0146	1.237170	60	1	4	4				
77.1838	1.234880	41	5	1	3				

77.6948	1.228030	3	3	0	5				
77.9748	1.224320	11	1	6	1				
78.2005	1.221350	65	2	5	2				
80.8143	1.188310	3	2	2	5				
81.1765	1.183920	5	5	0	4				
81.7052	1.177590	20	4	4	0				
81.8477	1.175900	8	1	3	5				
82.3471	1.170030	7m	1	6	2				
82.3471	1.170030	m	6	0	3				
82.7364	1.165510	7	3	5	0				
83.1535	1.160720	14	4	4	1				
83.2385	1.159750	13	3	3	4				
83.4048	1.157860	38	4	3	3				
84.2668	1.148200	42	2	4	4				
84.3798	1.146950	21	0	0	6				
84.9327	1.140890	1	4	0	5				
85.4576	1.135220	17	2	5	3				
85.8165	1.131390	2	2	6	0				
87.3393	1.115540	30	1	5	4				
87.4523	1.114390	47m	1	1	6				
87.4523	1.114390	m	4	4	2				
88.0042	1.108820	27	2	3	5				
88.4984	1.103900	73	3	5	2				
89.5483	1.093660	5	1	6	3				
90.0474	1.088890	1	1	4	5				
90.9274	1.080630	20	1	7	0				
91.5631	1.074780	12	2	6	2				
92.4486	1.066790	5m	1	7	1				
92.4486	1.066790	m	6	0	4				
93.4710	1.057790	4	4	3	4				
94.1362	1.052060	5	5	0	5				
95.0195	1.044600	1	4	5	0				
95.5209	1.040440	10	2	5	4				
95.6862	1.039080	7	7	0	3				
96.1876	1.034990	11	3	3	5				
96.4624	1.032770	14	4	5	1				
96.6617	1.031170	37m	2	2	6				
96.6617	1.031170	m	7	1	2				
97.2162	1.026760	6	2	4	5				
97.6914	1.023030	22	1	3	6				
98.1049	1.019820	10	8	0	0				
98.5228	1.016610	25	3	6	1				
98.7762	1.014680	3	2	6	3				
99.6429	1.008170	24	1	6	4				
100.3176	1.003200	21	5	1	5				

100.7960	0.999726	15m	4	0	6				
100.7960	0.999726	m	4	5	2				
101.2137	0.996727	7	7	2	0				
102.6812	0.986434	7	7	2	1				
102.9079	0.984877	33	3	6	2				
103.9582	0.977778	39m	1	7	3				
103.9582	0.977778	m	8	0	2				
104.8717	0.971752	30	4	4	4				
105.5594	0.967305	1	6	0	5				
105.9313	0.964931	8	3	5	4				
106.0486	0.964187	6	4	1	6				
106.6225	0.960577	11	3	4	5				
107.1394	0.957369	1	2	7	2				
107.5438	0.954888	1	8	1	0				

8.1.6. ZnO

PDF Card

PDF Number	00-036-1451		**Status**	Primary	**Quality Mark**		Star
Pressure/Temperature	Ambient						
Chemical Formula	Zn O						
Structural Formula							
Empirical Formula	O Zn						
Weight %	O19.66 Zn80.34						
Atomic %	O50.00 Zn50.00						
Compound Name	Zinc Oxide						
ANX							
Mineral Name	Zincite, syn						
Also Called	chinese white, zinc white						
Experimental	**Rad**	**λ**	**Filter**	**d-Spacing**	**Cutoff**	**Intensity**	**I/Ic**
	CuKá1	1.5406	Graph Mono	Diff.	17.70	Diffractometer	
	I/Ic - ND	**Camera Diameter**					
Physical	**SYS**	**Space Group**	**Aspect**	**Modulation Wave Vectors**			
	Hexagonal	P63mc (186)		-			
	Subsystems	ID W Matrix					
	Author's Cell	**a**	**b**	**c**	**α**	**β**	**γ**
		3.24982(9)		5.20661(15)			
		Volume	**Z**	**Molecular Volume/Formula Unit Volume**			
		47.62	2.00	23.81			
	Author's Cell Axial Ratio	**c/a**	**a/b**	**c/b**			
		1.602					
	Density	**Dcalc**	**Dmeas**	**Dstruc**			
		5.675					
	SS/FOM	**Temperature**	**Melting Point**	**R-factor**	**Error**	**Color**	
	F(27) = 129.6 (0.0072, 29)	299.0				Colorless	
Crystal	**Space Group**	**Molecular Weight**					
	P63mc (186)	81.38					
	Crystal Data	**a**	**b**	**c**	**α**	**β**	**γ**
		3.250	3.250	5.207	90.00	90.00	120.00
		Volume	**Z**				
		47.62	2.00				
	Crystal Data Axial Ratio	**c/a**	**a/b**	**c/b**			
		1.602	1.000	1.602			
	Reduced Cell	**a**	**b**	**c**	**α**	**β**	**γ**

		3.250	3.250	5.207	90.00	90.00	120.00
		Volume					
		47.62					
Optical	εα	**nωβ**	εγ	**Sign**	**2V**		
		=2.013	=2.029	=+			

Structure		
	ADP Type	
	Origin	
	Crystal (Symmetry Allowed)	Non-centrosymmetric - Pyro / Piezo (p), Piezo (2nd Harm.)
	SG Symmetry Operators	Seq | Operator
	SG Symmetry Operators (Modulated Structure)	Seq | Operator
	Atomic Coordinates	Atom | Num | Wyckoff | Symmetry | x | y | z | SOF | IDP | AET
	Atomic Coordinates (Modulated)	Atom | Num | Wyckoff | x | y | z | SOF | IDP | Subsys
	Anisotropic Displacement Parameters	Atom | Num | ADP11 | ADP22 | ADP33 | ADP12 | ADP13 | ADP23
	Anisotropic Displacement Parameters (Modulated)	Atom | Num | ADP11 | ADP22 | ADP33 | ADP12 | ADP13 | ADP23
Modulated	**Positional Displacement Parameters**	Atom Site | Axis | WV ID | Cos | Sin
	Atomic Displacement Parameters	Atom Site | WV ID | Cos | Sin | Tensor El.
	Occupation Modulation	Atom Site | WV ID | Cos | Sin
	Occupational - Crenel	Atom Site | C | W
	Displacement - SawTooth	Atom Site | C | W | AX | AY | AZ
Miscellaneous	**Subfiles**	Common Phase, Educational Pattern, Forensic, Inorganic, Metals & Alloys, Mineral Related (Mineral , Synthetic), NBS Pattern, Pharmaceutical (Excipient), Pigment/Dye
	Former PDF #	
	Prototype Structure	Zn O
	Prototype Structure (Alpha Sort)	

	LPF Prototype Structure	Zn O,hP4,186
	LPF Prototype Structure (Alpha Sort)	
	Mineral Classification	Wurtzite (Supergroup), 2H (Group)
	Zeolite Classification	
	Pearson	hP4.00
	Pearson w/o H	
	Cross-References	00-005-0664 (Alternate), 01-075-1526 (Alternate), 04-001-7297, 04-003-2106, 04-004-2776, 04-004-4530, 04-004-4531, 04-004-5134, 04-004-6457, 04-004-7538, 04-004-8997, 04-005-4711, 04-005-5072, 04-005-5076, 04-006-1673, 04-006-2543, 04-006-2557, 04-006-9717, 04-007-1614, 04-007-4718, 04-007-5097, 04-007-9627, 04-007-9804, 04-007-9805, 04-008-2750, 04-008-3506, 04-008-4400, 04-008-6994, 04-008-7114, 04-008-8196, 04-008-8197, 04-008-8198, 04-009-7657
	CAS Number	1314-13-2
	Entry Date	09/01/1986
	Last Modification Date	
	Last Modifications	

References

Type	DOI	Reference
Primary Reference		McMurdie, H., Morris, M., Evans, E., Paretzkin, B., Wong-Ng, W., Ettlinger, L., Hubbard, C. Powder Diffr. 1, 76 (1986).
Additional Pattern		5. Swanson, H., Fuyat, R. Natl. Bur. Stand. (U. S.), Circ. 539 2, 25 (1953).
Optical Data		Dana's System of Mineralogy, 7th Ed. I, 504.
Polymorphism		3. Bates, C., White, W., Roy, R. Science 137, 993 (1962).
Polymorphism		4. Radczewski, O., Schicht, R. Naturwissenschaften 56, 514 (1969).
Structure		1. Bragg, W. Philos. Mag. 39, 647 (1920).
Structure		2. Abrahams, S., Bernstein, J. Acta Crystallogr., Sec. B: Struct. Crystallogr. Cryst. Chem. 25, 1233 (1969).

Comments

Database Comments	Additional Patterns: To replace 00-005-0664 (5). See PDF 01-075-1526. Color: Colorless. General Comments: The structure was determined by Bragg (1) and refined by Abrahams, Bernstein (2). Powder Data: References to other early patterns may be found in reference (5). Polymorphism/Phase Transition: A high pressure cubic NaCl-type of ZnO is reported by Bates et al. (3) and a cubic, sphalerite type is reported by Radczewski, Schicht (4). Sample Source or Locality: The sample was obtained from the New Jersey Zinc Co., Bethlehem, Pennsylvania, USA. Temperature of Data Collection: The approximate temperature of data collection was 299 K. Unit Cell Data Source: Powder Diffraction.
User Comments	
Shared Comments	

d-Spacings

λ =Cu Kα1 1.54056 Å

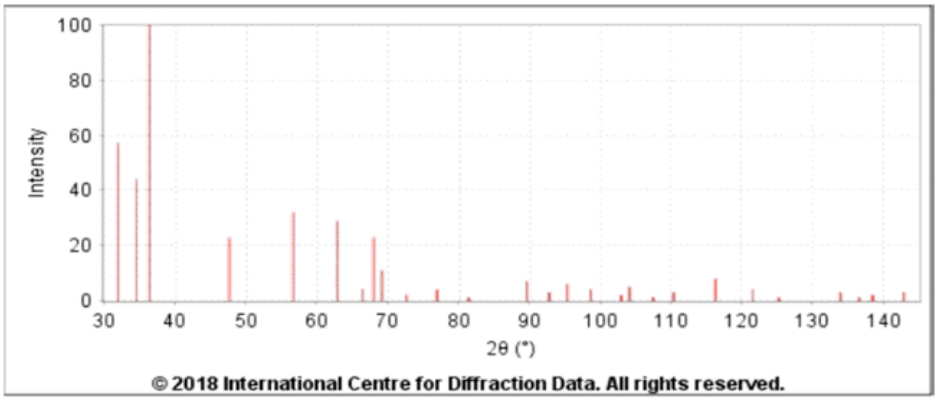

Zn O - 00-036-1451 (Stick, Fixed Slit Intensity)

2θ	d(Å)	Intensity	h	k	l	m	n	o	*
31.7694	2.814300	57	1	0	0				
34.4211	2.603320	44	0	0	2				
36.2521	2.475920	100	1	0	1				
47.5376	1.911140	23	1	0	2				
56.6016	1.624720	32	1	1	0				
62.8624	1.477120	29	1	0	3				
66.3782	1.407150	4	2	0	0				
67.9610	1.378180	23	1	1	2				
69.0982	1.358250	11	2	0	1				
72.5599	1.301740	2	0	0	4				
76.9528	1.238010	4	2	0	2				
81.3677	1.181620	1	1	0	4				
89.6045	1.093120	7	2	0	3				
92.7808	1.063840	3	2	1	0				
95.3007	1.042260	6	2	1	1				
98.6092	1.015950	4	1	1	4				
102.9424	0.984641	2	2	1	2				
104.1304	0.976632	5	1	0	5				
107.4262	0.955607	1	2	0	4				
110.3879	0.938120	3	3	0	0				
116.2744	0.906943	8	2	1	3				
121.5669	0.882558	4	3	0	2				
125.1826	0.867681	1	0	0	6				
133.9254	0.837033	3	2	0	5				
136.5130	0.829282	1	1	0	6				
138.5054	0.823695	2	2	1	4				
142.9096	0.812469	3	2	2	0				